Event Discrimination with Topological 3D Reconstruction at MeV Energies in the JUNO Experiment

Dissertation
zur Erlangung des Doktorgrades
an der Fakultät für Mathematik, Informatik und Naturwissenschaften
Fachbereich Physik
der Universität Hamburg

vorgelegt von

Henning Rebber

Hamburg
2019

Gutachter/innen der Dissertation:	Prof. Dr. Caren Hagner Dr. Björn S. Wonsak
Zusammensetzung der Prüfungskommission:	Prof. Dr. Dieter Horns Prof. Dr. Caren Hagner Prof. Dr. Markus Drescher Dr. Björn S. Wonsak Dr. Kai Schmidt-Hoberg
Vorsitzende/r der Prüfungskommission:	Prof. Dr. Dieter Horns
Datum der Disputation:	17.12.2019
Vorsitzender des Fach-Promotionsausschusses PHYSIK:	Prof. Dr. Günter H. W. Sigl
Leiter des Fachbereichs PHYSIK:	Prof. Dr. Wolfgang Hansen
Dekan der Fakultät MIN:	Prof. Dr. Heinrich Graener

Abstract

The JUNO experiment will use an unsegmented tank filled with 20 kton liquid scintillator to detect neutrinos and antineutrinos, starting from 2021. An important goal is to answer the open question of neutrino mass ordering by measuring electron-antineutrinos from two nuclear power plants in $\sim 53\,\mathrm{km}$ distance. The measurement will also determine the solar oscillation parameters θ_{12} and Δm^2_{21} with a precision below 1 %. A further goal is to measure solar ^{7}Be and ^{8}B neutrinos at high rates. The reactor antineutrinos are identified by means of inverse beta decay (IBD) which leads to a prompt positron and a delayed neutron signal. However, β^--decays of cosmogenic ^{8}He and ^{9}Li can be accompanied by neutron emission and thus mimic the IBD signature. Solar neutrinos are detected via elastic scattering off electrons. The cosmogenic β^+-emitters ^{10}C and ^{11}C are major background here. In any case, a discrimination between electron and positron events would mean a background reduction.

The presented discrimination is based on topological differences between the energy deposition of MeV electrons and positrons. A topological 3D reconstruction (TR) was applied to Geant4-simulated data in order to see the resulting fine differences in pulse shape. After successfully adapting the TR to JUNO, MeV events were closely analysed. It was found that the point-like electron events create less diffuse TR results than positron events. The actual discrimination was twofold: firstly using classically developed single parameter cuts, and secondly by the set-up and training of a convolutional neural network (CNN). The classic approach (the CNN) achieved an accuracy, defined as the ratio of correct classifications at balanced amounts of signal and background events, of 76.9 % (80.8 %) at visible energies within $(2.75 \pm 0.25)\,\mathrm{MeV}$. The discrimination potential was studied for all detector regions and for energies up to 10 MeV. In accordance with the expectation the discrimination power decreases continuously towards higher energies.

^{10}C was studied as a special case since its decay features an additional 718 keV gamma. This enhanced the accuracy to be 85.8 % (89.8 %). Finally, it was demonstrated that the method is sensitive also to a discrimination between electron and gamma events. Here, the accuracy was 69.9 % (73.6 %).

Zusammenfassung

Das JUNO Experiment wird ab 2021 mit einem unsegmentierten, 20 kton fassenden Flüssigszintillatortank Neutrinos und Antineutrinos detektieren. Ein wichtiges Ziel ist die Bestimmung der bislang ungeklärten Neutrinomassenordnung durch die Messung von Antielektronneutrinos zweier Atomkraftwerke in ~ 53 km Entfernung. Die Messung wird außerdem die solaren Oszillationsparameter θ_{12} und Δm^2_{21} mit einer Genauigkeit von unter 1 % festlegen. Weiterhin sollen solare ^{7}Be und ^{8}B Neutrinos mit hohen Raten gemessen werden. Die Reaktorantineutrinos sind über den inversen Betazerfall (IBD), der ein promptes Positron- und ein verzögertes Neutronsignal liefert, gut zu identifizieren. Jedoch können β^--Zerfälle von kosmogenem ^{8}He und ^{9}Li von einer Neutronemission begleitet sein und damit die IBD Signatur imitieren. Solare Neutrinos werden mittels elastischer Streuung an Elektronen detektiert. Hierbei stellen die kosmogenen β^+-Emitter ^{10}C und ^{11}C einen großen Untergrund dar. In den genannten Fällen ist eine Diskriminierung von Elektron- und Positronereignissen geeignet, um Untergrund zu reduzieren.

Die Basis für die hier gezeigte Unterscheidung sind topologische Unterschiede in der Energiedeposition von MeV Elektronen und Positronen. Um die sich ergebenden feinen Unterschiede in der Pulsform sichtbar zu machen, wurde eine topologische 3D Rekonstruktion (TR) auf Geant4-simulierte Daten angewendet. Nach erfolgreicher Anpassung der TR and JUNO folgte eine eingehende Analyse von MeV Ereignissen. Es zeigte sich, dass die punktförmigen Elektronereignisse weniger diffuse TR Resultate erzeugen als Positronereignisse. Die eigentliche Diskriminierung erfolgte auf zwei Arten: zum einen durch klassisch entwickelte Unterscheidungsparameter und zum anderen durch das Aufsetzen und Trainieren eines *Convolutional Neural Networks* (CNN). Mit dem klassichen Ansatz (mit dem CNN) ließ sich eine Treffgenauigkeit, definiert als der Anteil korrekter Klassifizierungen bei ausgewogenem Verhältnis von Signal- und Untergrundereignissen, von 76,9 % (80,8 %) bei sichtbaren Energien innerhalb von $(2,75 \pm 0,25)$ MeV erzielen. Das Diskriminierungspotenzial wurde in allen Detektorregionen untersucht sowie für Energien von bis zu 10 MeV. Erwartungsgemäß ergab sich eine kontinuierliche Abschwächung der Unterscheidbarkeit zu höheren Energien.

Es wurde der Spezialfall von ^{10}C untersucht, bei dessen Zerfall ein zusätzliches 718 keV Gamma entsteht. Dadurch konnte die Treffgenauigkeit auf 85,8 % (89,8 %) gesteigert werden. Ebenfalls zeigte sich, dass die Methode auch auf die Unterscheidung zwischen Elektron- und reinen Gammaereignissen sensibel ist. Hier lag die Treffgenauigkeit bei 69,9 % (73,6 %).

Contents

Introduction

Neutrinos, these most exceptional elementary particles being able to change their flavour during propagation in neutrino oscillations, have been under scientific research throughout the past decades, but still it has not been possible to draw all their secrets from them. The reason is an extremely low interaction rate, making it necessary to build enormous detectors and operate them under very low background conditions. The fundamental importance attached to neutrino physics can be concluded not only from the high number of past and present major experiments, but also from the fact that, after neutrino related awardings in 1988, 1995, and 2002, also the 2015 Nobel prize in physics was given out for the discovery of neutrino oscillations.

One open question is the mass ordering problem. From the presence of oscillations it can be deduced that at least two out of three mass states for neutrinos are non-zero. While the splitting between two masses is known for one pair of eigenstates, past oscillation measurements could only reveal as much as the absolute value of the second independent mass splitting. This leaves two possible hierarchies. A determination of the correct one would remove ambiguities in the search for CP violation in weak interactions. Furthermore, it would have an impact on searches for neutrinoless double-beta decay and also on neutrino mass models.

The mass ordering problem is a major purpose of the JUNO experiment [1] which is currently being built in the south of China. JUNO is designed as a 20 kton liquid scintillator (LSc) detector with an extraordinarily high energy resolution of $3\,\%/\sqrt{\mathrm{energy/MeV}}$. This is necessary in order to precisely measure the energy spectrum of electron antineutrinos from two nuclear power plants. The special baseline of ~ 53 km makes it possible to determine the mass ordering from a fine oscillation structure imprinted on the spectrum. The reactor neutrinos induce inverse beta decays in the LSc which can be identified by triggering on the coincidence of a positron and a delayed neutron signal.

JUNO is located 650 m underground in order to reduce the exposure to cosmic muons to 3.5 Hz. Muon events are a major issue since they produce the long-lived isotopes ^{8}He and ^{9}Li which can undergo β^--decay and simultaneously emit a neutron. The measured signals are likely to mimic the signature of inverse beta decay. Temporal spatial vetoes around muon tracks are applied to minimise this background.

The JUNO detector will also be able to detect solar neutrinos. Investigating the lower end of the ^{8}B neutrino spectrum around 3 MeV can provide a measuring point in the up-turn region of the effect that the solar mass has on neutrino oscillations. The long-awaited measurement will close an important gap in the experimental confirmation of the model describing neutrino oscillations in matter. Furthermore, the high-rate measurement of ^{7}Be neutrinos can hint on the nature of solar metallicity.

Solar neutrinos undergo elastic scattering off electrons in the LSc material and thus cause electron signals. Major background will come from the likewise cosmogenic spallation products ^{10}C, ^{11}C, and ^{11}Be. Furthermore, external gamma background is to be expected from the natural radioactivity in material surrounding the scintillator. A 5 m deep fiducial cut is foreseen to avoid external gamma events.

Both the studies for mass ordering and solar neutrinos would strongly profit from a pulse shape discrimination between electrons and positrons. ^{8}He and ^{9}Li could be identified which would allow to measure their rates and, depending on the cleanness of the discrimination, even to enhance the signal exposure by reducing the fiducial muon vetoes. Solar electron signals could be distinguished from background due to the β^{+} emitters ^{10}C and ^{11}C which are dominating the most conclusive region of the ^{8}B neutrino spectrum. Furthermore, if a discrimination even between gamma and electron events is possible, this would allow to enhance the fiducial volume for solar neutrino measurements.

So far, the only employed way to discriminate electron and positron events in a LSc experiment is a pulse shape discrimination based on positronium formation like it is done in the solar neutrino experiment Borexino [2, 3]. It makes use of the fact that about half of the positrons form ortho-positronium in the target material. This bound state with a target electron delays the annihilation according to an exponential decay with the inverse constant $\tau \approx 3$ ns. A pulse shape discrimination between electron and gamma events has not yet been established.

This work follows a completely new discrimination approach for low energy events. The key lies in the event topologies. Electrons of a few MeV in a LSc detector deposit their energy very compactly within a few centimetres of flight distance. Although positron tracks start off equally, the annihilation with a target electron produces two 511 keV gammas at the end of the track. The gammas start back-to-back and easily travel distances of more than 10 cm before starting to deposit energy within one or more Compton scatterings.

JUNO's high optical coverage of more than 75 % leads to an expected photoelectron yield of $\sim 1,200$ per MeV of deposited energy, more than any other large neutrino detector. This quality in statistical information brings within reach to find traces of these characteristics in the hit time distribution.

An event topology in unsegmented LSc detectors can partly be recovered and visualised, as it was described and demonstrated for high energy muons in [4]. Based on the detection time of a photon, a probability density distribution can be assigned to each hit, mapping the probability for the emission point under consideration of the detector geometry and optical model. The contributions from all hits can be combined, finally resulting in a three-dimensional probability density distribution for photon emission which actually reflects the event topology.

The topological reconstruction was adapted to the needs and requirements of JUNO during this work. Since the method was designed for the purpose of tracking high energy muons, it first needed to be seen how the reconstruction responds to low energy events. It then had to be carefully studied if and how the topological features of electron, positron, and also pure gamma events can be distinguished. Finally, a statistical evaluation was performed on simulated data.

The thesis is structured as follows: Chapter 1 gives an overview on the state of research in neutrino physics with the focus lying on mass ordering. Chapter 2 generally describes the technique of LSc detectors. Chapter 3 deals with the actual JUNO experiment. It describes the detector design and discusses the most important aspects of the physics programme. It is followed by a quick review of the official JUNO simulation software in Chapter 4. Chapter 5 is important to interpret the results of this work. Its first part briefly explains the algorithm of the topological reconstruction. The second part documents major steps that were taken in the scope of this thesis in order to make the method applicable to JUNO or improve its performance. In this context, also a small study of differences in the behaviour of Cherenkov and scintillation light is shown. The final Chapter 6 presents the event discrimination. Two strategies are being followed, firstly the classic development of discrimination parameters and secondly the implementation of an artificial neural network to be trained for event classification. The results of a quantitative evaluation are given and compared for both approaches. The thesis closes with a final conclusion and outlook.

Chapter 1

Neutrino Physics

Like all other known elementary particles, neutrinos have their place in the Standard Model (SM) of particle physics. Herein they act as electrically neutral and colourless spin-$\frac{1}{2}$ Dirac fermions and are described as massless. Three flavours exist both in the particle and in the antiparticle sector: ν_e, ν_μ, ν_τ and $\bar{\nu}_e$, $\bar{\nu}_\mu$, $\bar{\nu}_\tau$, respectively. Each flavour is associated with one charged lepton and shares its lepton family number. The flavour-changing process of neutrino oscillation is experimental evidence for physics beyond the SM. The process contradicts the requirement of the particle's masslessness and violates the conservation of lepton family number.

As a key to understand the motivation behind the numerous and sometimes gigantic neutrino experiments around the globe, this chapter mainly focuses on neutrino oscillations. The formalism is explained in Section 1.1, first for oscillations in vacuum and second in matter. Section 1.2 gives an overview on strategies to track down the parameters required by the oscillation model, going along with the technologies and experiments that lead to our current best fit values, i.e. solar, atmospheric, accelerator, and reactor experiments. Section 1.3 adresses the open questions that drive most current efforts in the field of neutrino physics with emphasis on the determination of neutrino mass ordering.

1.1 Theory of Neutrino Oscillations

The quantum mechanical concept of neutrino oscillations follows the idea of non-identical weak and mass states. By assuming that a flavour eigenstate can be described as a superposition of mass eigenstates and vice versa, and by requiring that neutrinos interact in a pure flavour state, it can be concluded that the admixed mass states travel with different phase velocities during propagation. Thus the composition at the time of detection will have changed with respect to creation. The flavour state is not pure anymore, hence the observed flavour can differ from the produced one. In that sense it can be explained that the neutrino flux of one species – ν_e in case of solar experiments – is reduced while the total neutrino flux is found to be stable.

In the following a brief overview on the oscillation formalism is given for oscillations in vacuum (Section 1.1.1) and flavour conversions in matter (Section 1.1.2). For more details see [5, 6, 7].

1.1.1 In Vacuum

Following the derivation in [7], the two orthonormal sets of n flavour eigenstates $|\nu_\alpha\rangle$ and n mass eigenstates $|\nu_i\rangle$ are connected such that

$$|\nu_\alpha\rangle = \sum_i U_{\alpha i} |\nu_i\rangle \,, \text{ and } |\nu_i\rangle = \sum_\alpha (U^\dagger)_{i\alpha} |\nu_\alpha\rangle = \sum_\alpha U^*_{i\alpha} |\nu_\alpha\rangle \,, \tag{1.1}$$

where U is a unitary $n \times n$ mixing matrix. The time development of the stationary mass eigenstates is given by

$$|\nu_i(x,t)\rangle = \mathrm{e}^{-\mathrm{i}E_i t} |\nu_i(x,0)\rangle \,, \tag{1.2}$$

with time t, energy E_i of eigenstate i, and position x, while the neutrino was produced with momentum p at $x = 0$ and $t = 0$:

$$|\nu_i(x,0)\rangle = \mathrm{e}^{\mathrm{i}px} |\nu_i\rangle \,. \tag{1.3}$$

Small masses $m_i \ll p$ and high energies $E \approx p$ are assumed, so that the relativistic case

$$E_i = \sqrt{m_i^2 + p_i^2} \simeq p_i + \frac{m_i^2}{2p_i} \simeq E + \frac{m_i^2}{2E} \tag{1.4}$$

holds. The development over time of a neutrino with flavour $|\nu_\alpha\rangle$ produced at $t = 0$ is then given by

$$|\nu(x,t)\rangle = \sum_i U_{\alpha i} \mathrm{e}^{\mathrm{i}px} \mathrm{e}^{-\mathrm{i}E_i t} |\nu_i\rangle = \sum_{i,\beta} U_{\alpha i} U^*_{\beta i} \mathrm{e}^{\mathrm{i}px} \mathrm{e}^{-\mathrm{i}E_i t} |\nu_\beta\rangle \,. \tag{1.5}$$

For a conversion from flavour $|\nu_\alpha\rangle$ to a flavour $|\nu_\beta\rangle$, this results in a transition amplitude

$$\begin{aligned} A(\alpha \to \beta)(t) = \langle \nu_\beta | \nu(x,t) \rangle &= \sum_i U^*_{\beta i} U_{\alpha i} \exp\left(-\mathrm{i}\frac{m_i^2}{2}\frac{L}{E}\right) \\ &= A(\alpha \to \beta)\left(\frac{L}{E}\right), \end{aligned} \tag{1.6}$$

where the relativistic assumptions from Equation (1.4) and $L = x = ct$ with speed of light c were used. Note that the time dependence was expressed in terms of distance L from the source. The transition probability P is given by

$$\begin{aligned} P(\alpha \to \beta)(t) &= |A(\alpha \to \beta)|^2 \\ &= \sum_i \sum_j U_{\alpha i} U^*_{\alpha j} U^*_{\beta i} U_{\beta j} \mathrm{e}^{-\mathrm{i}(E_i - E_j)t} \\ &= \sum_i \left|U_{\alpha i} U^*_{\beta i}\right|^2 + 2\Re \sum_{j>i} U_{\alpha i} U^*_{\alpha j} U^*_{\beta i} U_{\beta j} \exp\left(-\mathrm{i}\frac{\Delta m_{ij}^2}{2}\right)\frac{L}{E}. \end{aligned} \tag{1.7}$$

Here, the common expression

$$\Delta m_{ij}^2 = m_i^2 - m_j^2 \tag{1.8}$$

was used to denote the mass splitting. If all $U_{\alpha i}$ are real, which would be the case for CP invariance, Equation (1.7) can be simplified to

$$\begin{aligned} P(\alpha \to \beta)(t) &= \sum_i U_{\alpha i}^2 U_{\beta i}^2 + 2\sum_{j>i} U_{\alpha i} U_{\alpha j} U_{\beta i} U_{\beta j} \cos\left(\frac{\Delta m_{ij}^2}{2}\frac{L}{E}\right) \\ &= \delta_{\alpha\beta} - 4\sum_{j>i} U_{\alpha i} U_{\alpha j} U_{\beta i} U_{\beta j} \sin^2\left(\frac{\Delta m_{ij}^2}{2}\frac{L}{E}\right). \end{aligned} \tag{1.9}$$

Here it can be seen that a flavour transition requires at least one m_i to be different from zero. Furthermore, it can be concluded that the probability to find the original flavour is given by

$$P(\alpha \to \alpha) = 1 - \sum_{\alpha \neq \beta} P(\alpha \to \beta). \tag{1.10}$$

It is sometimes sufficient to consider two-flavour oscillations, more precisely when the combination of distance L and the particular $U_{\alpha i}$ causes one specific oscillation to dominate. U can then be parametrised with an angle θ and Equation (1.7) reads

$$P(\alpha \to \beta) = \sin^2(2\theta)\sin^2\left(\frac{\Delta m^2}{4}\frac{L}{E}\right). \tag{1.11}$$

In the case of antineutrinos, all $U_{\alpha i}$ have to be replaced by their complex conjugate. This also implies that for CP violation $P(\nu_\alpha \to \nu_\beta) \neq P(\bar{\nu}_\alpha \to \bar{\nu}_\beta)$.

1.1.2 In Matter

As soon as neutrinos traverse dense matter, further considerations have to be made. L. Wolfenstein published his thoughts on implications from coherent neutrino forward scattering in 1978 [8]. Due to their ability to interact weakly, neutrinos feel a potential from the surrounding protons, neutrons, and electrons. Since the nucleons – or the contained u and d quarks, respectively – have a flavour-symmetric cross section for neutral current (NC) interactions with neutrinos, the effect of the resulting potential on the propagation of mass eigenstates is a common phase factor which does not affect the oscillation probabilities. The same holds for NC interactions between electrons and neutrinos. In contrast, the charged current (CC) interaction features only channels featuring ν_e and $\bar{\nu}_e$. This introduces a matter potential

$$A = 2\sqrt{2}G_F N_e p \tag{1.12}$$

to the Hamiltonian operator H^α in the flavour representation – but only for $|\nu_e\rangle$. Here, the Fermi coupling constant G_F and the electron density N_e were used. In the antiflavour case, $-A$ has to be applied analogously on $|\bar{\nu}_e\rangle$. When solving the Schrödinger equation in order to describe the time development of the $|\nu_i\rangle$, the matrix H^α has to be transformed into mass space via $H^i = U^* H^\alpha U$. This results in off-diagonal terms. By diagonalisation, effective mass eigenstates can be obtained.

Like in vacuum, it is often convenient to describe a two-flavour scenario. Analogously, the transition probability can be phrased with one angle θ_m and the mass splitting $\Delta m_m^2 = m_{m2}^2 - m_{m1}^2$:

$$P_m(\alpha \to \beta) = \sin^2(2\theta_m)\sin^2\left(\frac{\Delta m_m^2}{4}\frac{L}{E}\right). \tag{1.13}$$

The transition parameters θ_m and Δm_m^2 are connected to their vacuum equivalents via

$$\Delta m_m^2 = \Delta m^2 \sqrt{\left(\frac{A}{\Delta m^2} - \cos 2\theta\right)^2 + \sin^2 2\theta} \quad \text{and} \tag{1.14}$$

$$\sin^2 2\theta_m = \frac{\sin^2 2\theta}{\left(\frac{A}{\Delta m^2} - \cos 2\theta\right)^2 + \sin^2 2\theta}. \tag{1.15}$$

It needs to be noted that Δm_m^2 and $\sin^2 2\theta_m$ are dynamical variables since A depends on the matter density. The shape of $\sin^2 2\theta_m$ shows a resonance at

$$A_R = \Delta m^2 \cos 2\theta. \tag{1.16}$$

Based on the work by Wolfenstein, S. P. Mikheev and A. Y. Smirnov discussed the implications for solar neutrinos in 1985 [9]. The situation can be approximated by a two flavour picture: Solar ν_e are produced in the core region of the sun and can undergo a transition into an effective flavour $\nu_{\mu\tau}$. The mass eigenstates are $|\nu_{m1}\rangle$ and $|\nu_{m2}\rangle$. The electron density can be assumed to be very high at production, i.e. $A \gg A_R$. According to Equations (1.13) and (1.15), a flavour conversion is very unlikely in that case. Oscillation is suppressed because the $|\nu_{m2}\rangle$ component in the coherent sum of mass eigenstates is so clearly dominating that no interference with $|\nu_{m1}\rangle$ takes place during propagation. While N_e changes slowly along the neutrino path, also θ_m changes adiabatically and at some point the resonance condition in Equation (1.16) is fulfilled. $|\nu_{m2}\rangle$ now contains equal fractions of $|\nu_e\rangle$ and $|\nu_{\mu\tau}\rangle$. When N_e finally approaches 0, $|\nu\rangle = |\nu_{m2}\rangle$ turns to $|\nu_2\rangle$ and the flavour ratio is given by the vacuum composition of $|\nu_2\rangle$.

To conclude, the development of transition probability in vacuum, where probabilities literally oscillate, is different from the adiabatic conversion at slowly varying matter density, which was called MSW effect after Mikheev, Smirnov, and Wolfenstein. Taking into account the current knowledge of mixing angles, the result is a survival probability of $P_m(\nu_e \to \nu_e) \simeq 0.31$. It has to be pointed out that the matter terms can be neglected if the resonance condition (1.16) is not passed. From Equations (1.12) and (1.16) it can be concluded that this is the case for neutrinos with energies below

$$E_R = \frac{\Delta m_{12}^2 \cos 2\theta_{12}}{2\sqrt{2} G_F N_e(0)} \simeq 1.8\,\mathrm{MeV}, \tag{1.17}$$

where the relativistic limit $p \approx E$ and the electron density $N_e(0)$ in the production region have been used. For energies $E \ll E_R$, θ_{12_m} is approximately θ_{12}, and hence the vacuum survival probability from Equation (1.11) is valid, which returns $P(\nu_e \to \nu_e) \simeq 0.57$. Solar neutrino experiments have measured signals from both the matter dominated and the vacuum energy regime. Results can be seen in Figure 1.3 in Section 1.2.1.

1.2 Mixing Parameters

For a complete description of neutrino oscillations, the squared mass differences Δm_{ij} between all n mass states and the entries of the $n \times n$ mixing matrix U have to be fixed. The number of free parameters to determine the $U_{\alpha i}$ can be reduced to $2n-1$ due to the requirement of unitarity and the fact that it describes relative phases. Since flavour and mass space can be considered as rotated against each other, U is usually parametrised like a rotation matrix with $\frac{1}{2}n(n-1)$ weak mixing angles and $\frac{1}{2}(n-1)(n-2)$ CP-violating phases. Interestingly, there is an analogy to CKM mixing in the quark sector. The weak mixing matrix is called U_{PMNS} after B. Pontecorvo, Z. Maki, M. Nakagawa, and S. Sakata, who contributed substantially to their development [10, 11].

For the scenario of three neutrino and antineutrino flavours the matrix reads:

$$
\begin{aligned}
U_{\text{PMNS}} &= \underbrace{\begin{pmatrix} 1 & 0 & 0 \\ 0 & c_{23} & s_{23} \\ 0 & -s_{23} & c_{23} \end{pmatrix}}_{\text{atmospheric}} \underbrace{\begin{pmatrix} c_{13} & 0 & s_{13}\mathrm{e}^{-\mathrm{i}\delta} \\ 0 & 1 & 0 \\ -s_{13}\mathrm{e}^{\mathrm{i}\delta} & 0 & c_{13} \end{pmatrix}}_{\text{reactor}} \underbrace{\begin{pmatrix} c_{12} & s_{12} & 0 \\ -s_{12} & c_{12} & 0 \\ 0 & 0 & 1 \end{pmatrix}}_{\text{solar}} \\
&= \begin{pmatrix} c_{12}c_{13} & s_{12}c_{13} & s_{13}\mathrm{e}^{-\mathrm{i}\delta} \\ -s_{12}c_{23} - c_{12}s_{23}s_{13}\mathrm{e}^{\mathrm{i}\delta} & c_{12}c_{23} - s_{12}s_{23}s_{13}\mathrm{e}^{\mathrm{i}\delta} & s_{23}c_{13} \\ s_{12}s_{23} - c_{12}s_{23}s_{13}\mathrm{e}^{\mathrm{i}\delta} & -c_{12}s_{23} - s_{12}c_{23}s_{13}\mathrm{e}^{\mathrm{i}\delta} & c_{23}c_{13} \end{pmatrix},
\end{aligned}
\tag{1.18}
$$

where the notations $s_{ij} = \sin\theta_{ij}$ and $c_{ij} = \cos\theta_{ij}$ with $i, j = 1, 2, 3$ have been used. According to Equation (1.7), the mixing angles θ_{ij} determine the oscillation amplitude while the complex phase δ introduces the possibility of CP violation.

In this representation, neutrinos are treated as Dirac fermions. There is reason to assume that neutrinos are their own antiparticles, so called Majorana fermions (see Section 1.3.4). Additional complex phases α and β appear in that case:

$$U = U_{\text{PMNS}} \cdot \text{diag}(1, \mathrm{e}^{\mathrm{i}\alpha}, \mathrm{e}^{\mathrm{i}\beta}). \tag{1.19}$$

The oscillation frequency depends on the mass splittings Δm_{ij}, two of which are independent in the three flavour case. The typical length scale on which flavour oscillations take place is given by the oscillation length

$$l_{osc} = 4\pi\hbar c \frac{E}{\Delta m^2}. \tag{1.20}$$

Here, $\hbar$ denotes the reduced Planck constant and c the speed of light. l_{osc} is an important aspect when setting up a strategy to experimentally find the oscillation parameters.

Much progress has been made in the constraints of mixing parameters during the past three decades. It is apparent from Equation (1.20) that the distance to neutrino sources is a decisive factor for their measurement. Sources provided by nature have a predefined distance to terrestrial detectors. Among those sources, the sun and the atmosphere of the Earth share the advantage of constantly high fluxes. Artificial sources like nuclear reactors and particle accelerators leave more freedom for beamline variations.

As indicated in the denotation of Equation (1.18), it turned out that solar ν_e detection is related to the determination of θ_{12} and Δm_{12}, while the observation of atmospheric neutrino and antineutrino fluxes are suitable for measuring θ_{23} and Δm_{23}, and reactor $\bar{\nu}_e$ help finding θ_{13}. The following sections review the contributions of each field to the current global best-fit values listed in Table 1.1. Furthermore, an overview on current efforts and perspectives is given. A comprehensive review can be found in [5]. A recent global fit analysis is described in [12].

Table 1.1: Three-flavour mixing parameters from a global fit [12]. Values (values) refer to the normal (inverted) mass ordering.

Parameter	best-fit	3σ
Δm^2_{21} [10^{-5} eV^2]	7.39	6.79 – 8.01
$\Delta m^2_{31(23)}$ [10^{-3} eV^2]	2.53 (2.51)	2.43 – 2.62 (2.41 – 2.61)
$\sin^2\theta_{12}$	0.310	0.275 – 0.350
$\sin^2\theta_{23}, \Delta m^2_{31(32)} > 0$	0.582	0.428 – 0.624
$\sin^2\theta_{23}, \Delta m^2_{32(31)} < 0$	0.582	0.433 – 0.623
$\sin^2\theta_{13}, \Delta m^2_{31(32)} > 0$	0.0224	0.0204 – 0.0244
$\sin^2\theta_{13}, \Delta m^2_{32(31)} < 0$	0.0226	0.0207 – 0.0246
δ/π	1.21 (1.56)	0.75 – 2.03 (1.09 – 1.95)

1.2.1 Solar Sector

Measurement of solar ν fluxes According to standard solar models (SSM) [13, 14], solar ν_e are produced in manifold channels. The fusion of hydrogen to helium

$$4p \rightarrow {}^4\mathrm{He} + 2e^+ + 2\nu_e \tag{1.21}$$

takes place in two sets of nuclear reactions: the dominating proton-proton (pp) chain and the CNO cycle. The pp chain subsumes three branches in which, based on the fusion of two protons, nuclei with mass numbers up to ^{8}B are involved in the ^{4}He production. In the CNO cycle, carbon, nitrogen, and oxygen are used as catalysts. All neutrino-

Table 1.2: Reaction channels for solar ν_e production together with their abbreviations and ν fluxes on Earth as calculated from the B16-GS98 SSM [14].

Reaction	Abbreviation	Flux ($\mathrm{cm}^{-2}\,\mathrm{s}^{-1}$)
pp chain		
$pp \to de^+\nu_e$	pp	$5.98(1{\pm}0.006) \times 10^{10}$
$pe^-p \to d\nu_e$	pep	$1.44(1{\pm}0.01) \times 10^{8}$
$^3\mathrm{He}\,p \to {}^4\mathrm{He}\,e^+\nu_e$	hep	$7.98(1{\pm}0.30) \times 10^{3}$
$^7\mathrm{Be}\,e^- \to {}^7\mathrm{Li}\,\nu_e\gamma$	^{7}Be	$4.93(1{\pm}0.06) \times 10^{9}$
$^8\mathrm{B} \to {}^8\mathrm{Be}^*\,e^+\nu_e$	^{8}B	$5.46(1{\pm}0.12) \times 10^{6}$
CNO cycle		
$^{13}\mathrm{N} \to {}^{13}\mathrm{C}\,e^+\nu_e$	^{13}N	$2.78(1{\pm}0.15) \times 10^{8}$
$^{15}\mathrm{O} \to {}^{15}\mathrm{N}\,e^+\nu_e$	^{15}O	$2.05(1{\pm}0.17) \times 10^{8}$
$^{17}\mathrm{F} \to {}^{17}\mathrm{O}\,e^+\nu_e$	^{17}F	$5.29(1{\pm}0.20) \times 10^{6}$

producing reactions are listed in Table 1.2 together with the common abbreviations and the resulting neutrino fluxes predicted by the B16-GS98 SSM [14]. Figure 1.1 shows the corresponding energy spectra on Earth as expected from the model and indicates the energy thresholds of selected experiments. Continuous spectra are expected from pp, ^{8}B, hep and the CNO neutrinos ^{13}N, ^{15}O, and ^{17}F. Monoenergetic lines show up for ^{7}Be and pep neutrinos.

The first generation of solar ν detectors used radiochemical methods, namely the ν_e-induced inverse beta decays from ^{37}Cl to ^{37}Ar and ^{71}Ga to ^{71}Ge, the products of which could subsequently be extracted and counted. From the energy thresholds of 233 keV and 814 keV, respectively, the Ga and Cl detectors measured the integrated fluxes and reported significant deficits with regard to the SSM.

Modern detectors typically use either water-Cherenkov (WC) or liquid scintillator (LSc) technology. Both share the advantages of real-time detection and – at least for most channels – energy sensitivity.

WC detectors make use of the fact that, in dielectric media, a charged particle with a velocity v_p higher than the medium's phase velocity of light causes a conic light front with an opening angle that only depends on v_p. The resulting ring-like image, composed of signals from multiple light sensors on a plane, allows for a reconstruction of v_p and the particle direction. In 1987, the 3 kt WC detector Kamiokande[16], and from 1996 on its 50 kt follow-up Super-Kamiokande (SK)[17] observed solar neutrinos via their elastic scattering (ES) off electrons

$$\nu_x + e^- \to \nu_x + e^- \qquad \text{(ES)}. \tag{1.22}$$

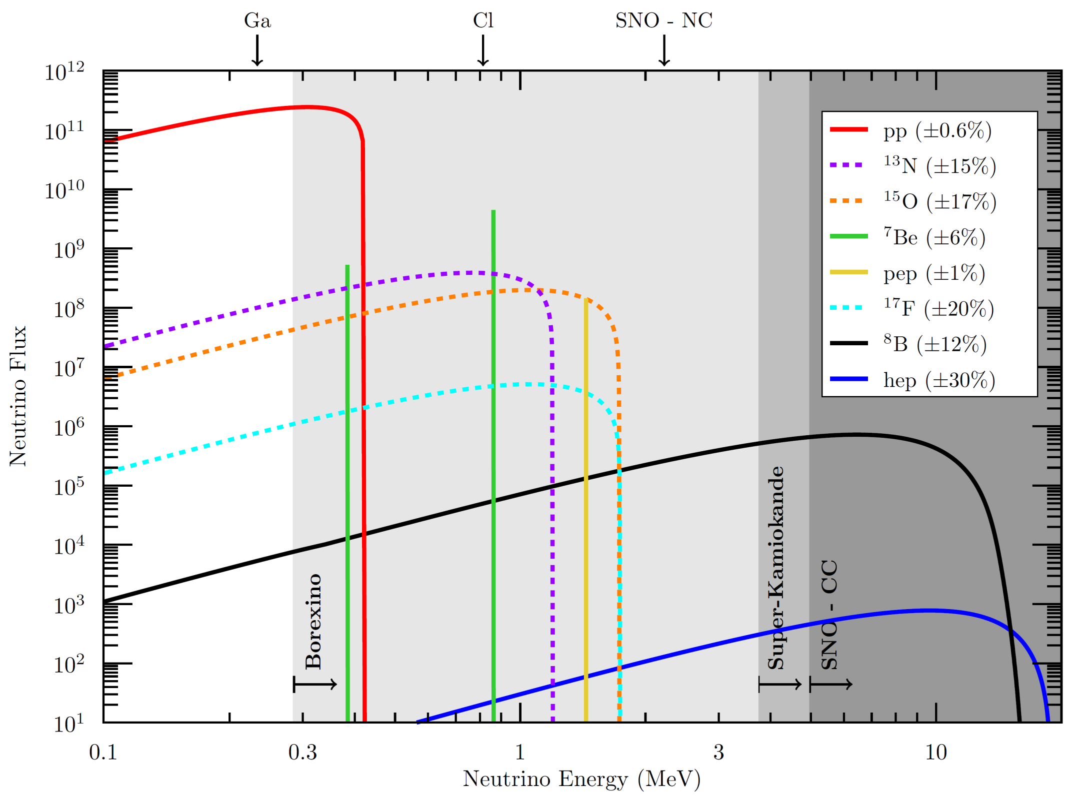

Figure 1.1: Energy spectra of solar ν fluxes as expected from the B16-GS98 SSM. Threshold energies are indicated by horizontal arrows for energy-sensitive experiments and by vertical arrows for energy-integrating experiments. Figure taken from [15].

The directional information helped to classify solar events here. Since reaction (1.22) has a higher cross section for ν_e than for other flavours, i.e. $\sigma(\nu_{\mu,\tau}e) \approx 0.16\,\sigma(\nu_e e)$, both detectors saw the deficit. It was the SNO experiment [18] which, starting measurements in 1999, shed some more light on the situation. Besides the (ES) channel, the contained heavy water (D_2O) was open to the charged current (CC) and neutral current (NC) reactions

$$\begin{aligned} &\nu_e + d \rightarrow e^- + p + p \qquad (\mathrm{CC}) \qquad \text{and} \\ &\nu_x + d \rightarrow \nu_x + p + n \qquad (\mathrm{NC}). \end{aligned} \tag{1.23}$$

The NC reaction is equally open to all flavours while the CC reaction works only with ν_e. Energy reconstruction is possible for ES and CC due to a correlation between the e^- and ν energies. Salt was added to the D_2O in a later phase to enhance the signal from neutron capture. With threshold energies above 2 MeV, the WC experiments are sensitive mostly to ^{8}B-ν with a minor contribution from hep-ν. The summed flux $\Phi_{\mu\tau}$ of ν_μ and ν_τ plotted over the ν_e flux Φ_e shows a linear relation based on the channel as the coloured bands in Figure 1.2 show. The joint flux value determined from the intersect, depicted by contour rings, is in good agreement with SSM predictions illustrated by the dashed lines.

The measured fluxes[17, 18], considering especially the mixing-independent NC channel, strongly supported the conversion theory and fit in with calculations based on the solar MSW effect under the assumption of a large mixing angle (LMA). Solely however, they do not exclude all remaining solutions.

In order to measure other fluxes than ^{8}B-ν it became necessary to investigate lower energies. LSc detectors have energy thresholds as low as 200 keV and can detect solar neutrinos via ES (Equation (1.22)). The electron kinetic energy is absorbed by the molecules inside the LSc and re-emitted isotropically in the optical spectrum. Directionality cannot be used. Chapter 2 discusses the technology in detail.

The 300 t LSc detector Borexino [20] started data taking in 2007. It was designed to observe the flux of the monochromatic 0.86 MeV ^{7}Be-ν. Even the pp-ν flux could be measured after an extensive purification campaign in 2012, [21]. The results confirmed – once again – the SSM, but in particular also the MSW-LMA model. The light blue band in Figure 1.3 shows the ν_e survival probability $P(\nu_e \rightarrow \nu_e)$ as a function of neutrino energy. For energies above 10 MeV, matter effects cause $P(\nu_e \rightarrow \nu_e)$ to obey Equation 1.13. At very low energies, the sun appears transparent to neutrinos and Equation 1.11 holds. Minor corrections to the two flavour calculations arise from the small but non-vanishing θ_{13}. Black points in the plot represent, from left to right, Borexino measurements of

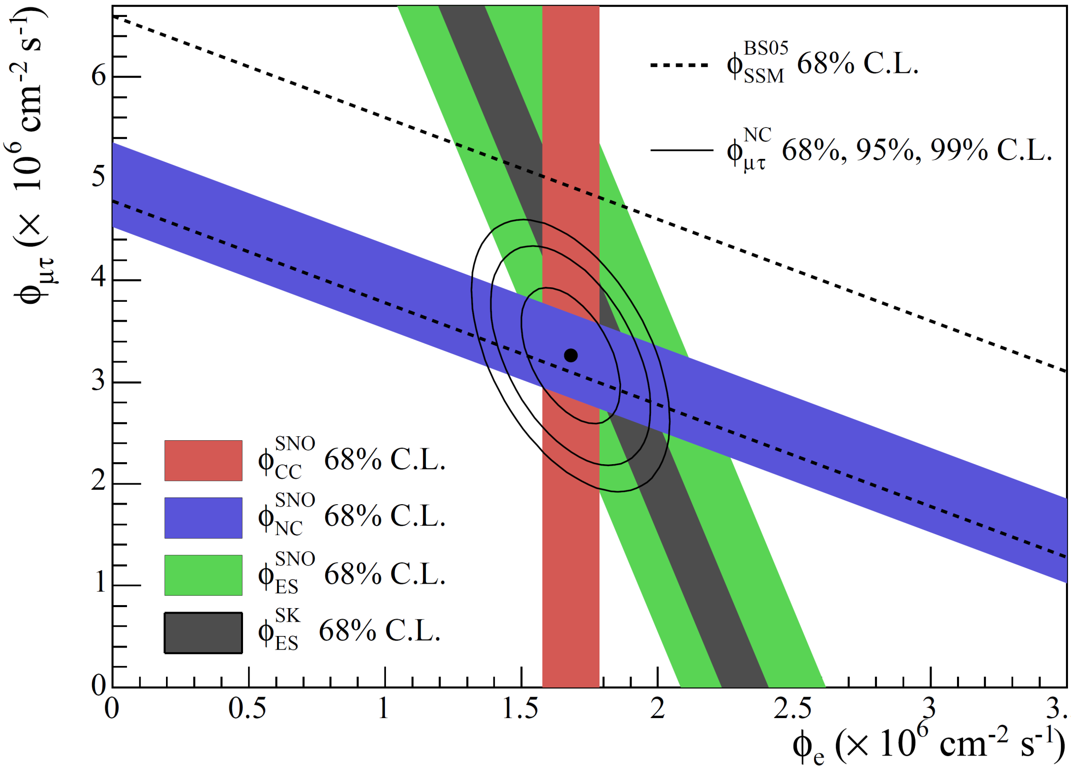

Figure 1.2: Results for measurements of ^{8}B neutrino fluxes in SNO and SK. The summed flux $\Phi_{\mu\tau}$ of ν_μ and ν_τ is plotted over the ν_e flux Φ_e for CC, NC and ES channels. The joint flux value determined from the intersect is depicted by contour rings. The SSM predictions are illustrated by the dashed lines. Taken from [19].

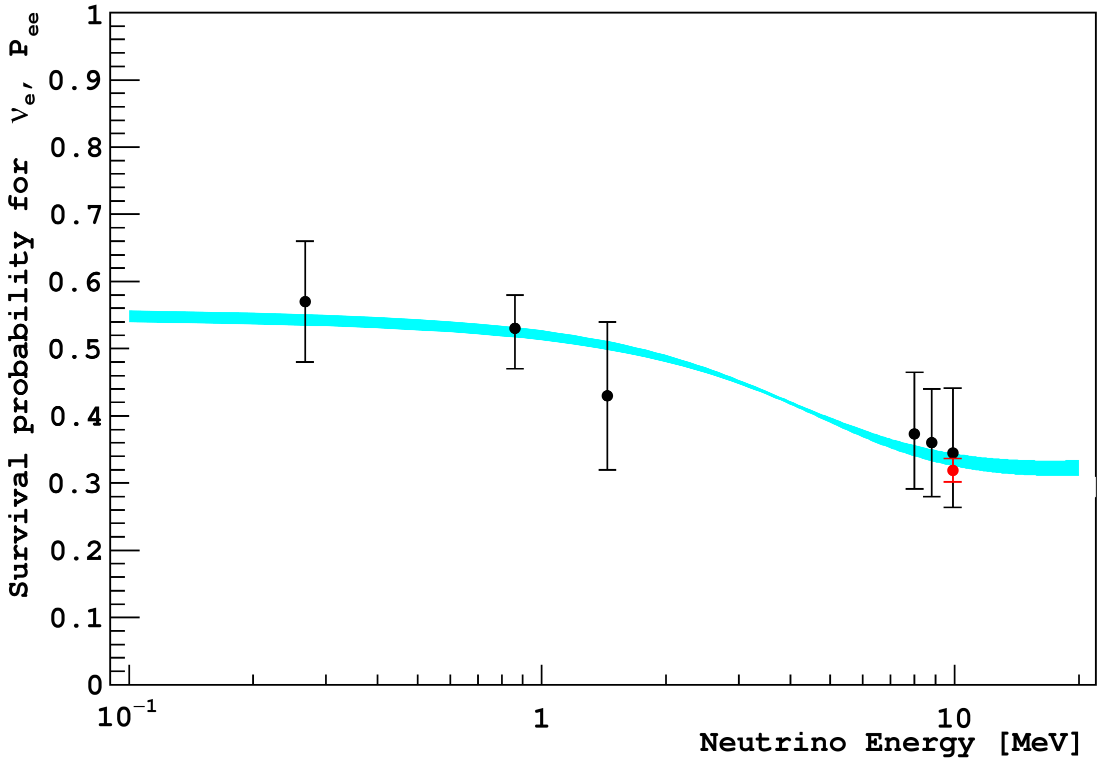

Figure 1.3: Blue band: Survival probability P_{ee} as a function of neutrino energy according to the MSW-LMA prediction. P_{ee} was calculated based on a high metallicity SSM. Black points from left to right: Borexino data from pp, ^{7}Be, pep, and ^{8}B measurements. The latter was determined threefold based on different energy ranges. Red point: combined ^{8}B data from SK and SNO. Taken from [5].

the pp, ^{7}Be, pep, and ^{8}B fluxes. The latter was determined threefold based on different energy ranges. The red point subsumes ^{8}B data from SK and SNO.

While $P(\nu_e \to \nu_e)$ is in good agreement with experimental data at the lower and upper end of the solar ν spectrum, the transition region between 2 MeV and 5 MeV has not been probed so far. In particular, the position of the upturn is vague. Future LSc detectors like JUNO [1] and the proposed Jinping experiment [22] plan measurements here. A discussion on the relevant cosmogenic backgrounds can be found in Section 3.2.3. While the Jinping location provides a uniquely low muon flux, JUNO will encounter the cosmogenic background by high statistics.

An interesting aspect arises from the fact that solar neutrinos reaching a detector in the nighttime must have crossed the Earth. Matter effects are expected to cause a slight regeneration of the ν_e flavour. Investigated by several experiments, the strongest claim of a day-night flux asymmetry comes from SK. With the ^{8}B-ν rates R_D and R_N for day and night, respectively, the asymmetry was reported to be $A_{AD} = 2(R_D - R_N)/(R_D + R_N) =$

$-0.033 \pm 0.010 \pm 0.005$ [17].

To conclude, all solar ν fluxes could be measured apart from the CNO and hep-ν fluxes. Especially the CNO components are of great importance for solar models. The fluxes are directly related to the abundances of metals, i.e. elements heavier than Helium, in the core of the sun. While helioseismical data indicates a high solar metallicity, more recent photosphere observations prefer a low metallicity model [23]. So far, background in Borexino was still too high for CNO detection. Currently, the SNO detector is about to be filled with LSc. The so-called SNO$^+$ experiment [24] is a promising candidate for a successful CNO measurement due to its very deep underground location. The same applies for the proposed Jinping detector.

Determination of θ_{12} and Δm^2_{12} Since the conversion of solar neutrinos is mostly driven by θ_{12} and Δm^2_{12}, the pair is often referred to as solar mixing parameters. Neglecting the impact of the comparatively small θ_{13} and assuming full knowledge of the SSM, the shape of P_{ee} over E (Figure 1.3) depends only on θ_{12} while the positions of transition region and upturn are determined by Δm^2_{12}. However, due to the lack of measurements in this very region, the constraints on Δm_{12} from solar experiments are rather loose. Help comes from another LSc detector: KamLAND [25] holds 1 kt of LSc and, from 2002 to 2011, detected mainly $\bar{\nu}_e$ from nuclear power reactors via the inverse beta decay. The reactor distances varied between 128 km and 214 km. Under the assumption of CPT invariance, the observed deficit in the $\bar{\nu}_e$ flux allowed a measurement of θ_{12} and Δm^2_{12}. Figure 1.4 shows the sensitive regions in the θ_{12}-Δm_{12} plane for KamLAND (blue) and the solar experiments (red). Herein, the θ_{13} value was fixed to the best global fit value. It has to be noted that the preferred Δm^2_{12} values show a tension at $2\,\sigma$ level. The results for θ_{12} are consistent. A higher precision on the solar mixing parameters is expected from JUNO. With a high statistics measurement of nuclear $\bar{\nu}_e$ at about 50 km distance, the uncertainties can be reduced to less than 1 % (see Section 3.2.3).

It has to be pointed out that the sign of Δm^2_{12} is known to be positive by the fact that MSW resonance is observed. The value can be calculated directly from Equation (1.17).

1.2.2 Atmospheric Sector

Determination of θ_{23} and $|\Delta m^2_{32}|$ The determination of $|\Delta m^2_{32}|$ and θ_{23} is historically related to atmospheric neutrinos. In present searches, also neutrino beams from accelerators play an important role.

In our atmosphere, neutrino production is a consequence of cosmic ray interaction

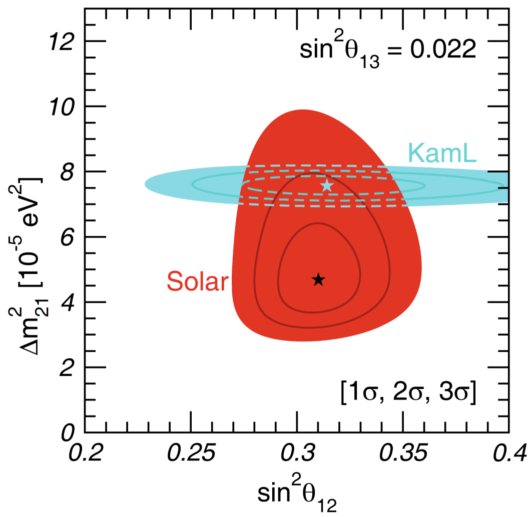

Figure 1.4: Results from KamLAND (blue) and solar experiments (red) for Δm^2_{21} over $\sin^2\theta_{12}$. The best fit values show a $2\,\sigma$ tension in Δm^2_{21}. Taken from [26].

with atmospheric atoms. 87 % of cosmic rays are protons [7], which in turn generate mostly charged π, but also K mesons. These decay predominantly via

$$\pi^+, K^+ \to \mu^+ + \nu_\mu, \qquad \mu^+ \to e^+ + \nu_e + \bar{\nu}_\mu \qquad \text{and} \tag{1.24}$$

$$\pi^-, K^- \to \mu^- + \bar{\nu}_\mu, \qquad \mu^- \to e^- + \bar{\nu}_e + \nu_\mu, \tag{1.25}$$

respectively. Accordingly, the ratio R of fluxes $(\nu_\mu + \bar{\nu}_\mu)$ and $(\nu_e + \bar{\nu}_e)$ can roughly be estimated to be

$$R = \frac{\nu_\mu + \bar{\nu}_\mu}{\nu_e + \bar{\nu}_e} \approx 2. \tag{1.26}$$

This is a good approximation at particle energies lower than 1 GeV. Above, however, more muons reach the ground before decaying, and R increases. Although atmospheric flux models for ν struggle with uncertainties of around 10 % below 10 GeV, the uncertainty on R is expected to be only 3 % due to a cancellation of systematics [27].

After Kamiokande reported an asymmetry between upward-going and downward-going events with $6\,\sigma$ in 1992 [28], Super-Kamiokande (SK) closer investigated the fluxes of μ and e-like events from 1996 on. The dominant detection channel for sub-GeV neutrinos and antineutrinos is quasi-elastic scattering off a nucleon N:

$$\nu + N \to l + N'. \tag{1.27}$$

Single meson production

$$\nu + N \to l + N' + m \tag{1.28}$$

becomes important between 2 GeV and 10 GeV. In either way, the neutrino induces the creation of a lepton l according to its flavour and sign. Due to electromagnetic shower production along an $e^{\pm}$ track, the Cherenkov ring on the plane of light sensors is more diffuse than for a $\mu^{\pm}$ track. This enables a classification into μ-like and e-like for fully contained events. On a statistical basis, e-like events from single meson production can be divided into ν_e and $\bar{\nu}_e$-enriched subsamples due to a longer livetime and subsequent decay of the π^+, while π^- gets captured on a ^{16}O nucleus very quickly. Partly contained events are generally treated as μ-like. A charge sign discrimination is not possible, though. The measured rates were sorted samplewise with respect to directionality. While for e-like events the zenith-angle distribution matched exactly the non-oscillatory prediction, a clear deficit was observed for μ-like events. This supported the oscillation hypothesis of $\nu_\mu \to \nu_\tau$ conversions. Further theories like neutrino decay could be excluded by the characteristic L/E-behaviour of events, where L could be estimated from the zenith-angle.

From the significant ν_μ disappearance and the missing indications for ν_e appearance, a large mixing angle within a two-neutrino scenario could be concluded. The SK constraints from presently all four combined data phases can be seen in the $\sin^2\theta_{23}$-Δm^2_{32} plane representation in Figure 1.5, which is based on three-neutrino analyses. The large mixing angle leaves open the question whether θ_{23} is maximal ($\theta_{23} = \pi/4$), lies in the first ($\theta_{23} < \pi/4$), or in the second octant ($\theta_{23} > \pi/4$).

In order to better constrain the atmospheric mixing parameters, the full three-neutrino scenario needed to be taken into account, going along with precise measurements of ν_μ disappearance and ν_e appearance. An inevitable issue in the context of atmospheric neutrino observation is the relatively large uncertainty on the point of neutrino production, which can lie within a few and a few tens of km above ground. One way around this problem are particle accelerators. High energy protons are directed onto a target so that secondary pions (90 %) and Kaons are created. Via the corresponding processes given within Equations (1.24) and (1.25), muons are created which get absorbed later on. Thus, the dominant flavours in the neutrino beam are ν_μ and $\bar{\nu}_\mu$. The beam can be narrowed by focusing the charged mesons within magnetic horns. Furthermore, an appropriate shaping of the magnetic field can enable particle sign selection. The beam is directed at a neutrino detector in a well defined distance of typically a few hundred km. A near detector, similar in functionality and structure, can help to cancel systematics by

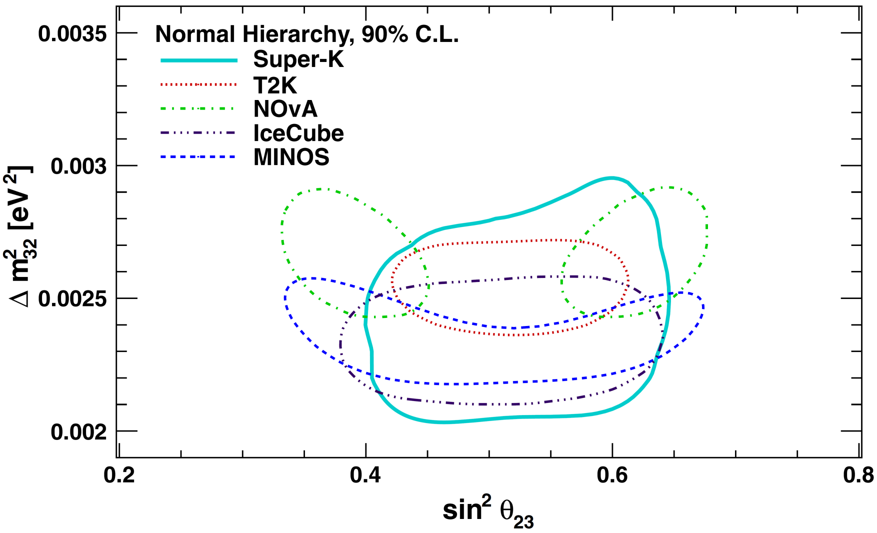

Figure 1.5: 90 % confidence regions in the $\sin^2\theta_{23}$-Δm^2_{32} plane for SK, T2K, NOνA, IceCube and MINOS based on three-neutrino analyses and assuming a normal mass ordering. Figure taken from [29]

monitoring the unoscillated neutrino flux.

Various of these long-baseline experiments have been constructed. MINOS [30] is a 5.4 kt iron-scintillator tracking calorimeter. Between 2005 and 2012 it received the 3 GeV-peaking neutrino beam NuMI from Fermilab at a baseline of 735 km. In combination with its 1 kt near detector at ~ 1 km, MINOS gives very narrow constraints on Δm^2_{31}, as depicted in Figure 1.5.

T2K [31] names the effort of directing a 600 MeV neutrino beam from J-PARC at the SK detector in 295 km distance. With interruptions, the beam has been operated with interruptions in neutrino and antineutrino mode since 2010. Due to a 2.5° off-axis configuration, the energy band is tightened to a more desirable range.

NOνA [32], intended as a successor to MINOS, sees the NuMI beam from a distance of 810 km. At its position 14.6 mrad off-axis, the energy peaks at 2 GeV. Data was taken from 2014. The detector itself is a 14 kt fine grained LSc calorimeter. A near detector is placed at 1 km distance. The allowed 90 % CL regions in Figure 1.5 form two islands, one for each octant option. NOνA disfavours a maximal mixing angle $\theta_{23} = \pi/4$ at $2.6\,\sigma$ significance. The second octant is mildly preferred in global fits [12].

Future long baseline experiments like DUNE and T2HK (see Section 1.3.1) promise measurements with very high precision.

Among the so-called neutrino telescopes, IceCube momentarily shows the highest sensitivity to atmospheric mixing. In a volume of $1\,\text{km}^3$, optical modules detect Cherenkov light in the Antarctic ice. In a denser instrumented sub-volume called DeepCore, atmospheric ν_μ and $\bar{\nu}_\mu$ interactions down to 6 GeV can be reconstructed.

So far no experiment was sensitive on the sign of Δm^2_{32}. The reason is the $\sin^2$ symmetry in the dominant terms of transition probabilities. The consequence is an unclear ordering of the masses, which will be discussed in Section 1.3.1.

1.2.3 Reactor Sector

Determination of θ_{13} The smallest mixing angle θ_{13} was also the last to be detected. The parameter is of great interest: For one thing, a precise knowledge helps to further constrain the solar and atmospheric mixing parameters in three-neutrino analyses. Furthermore, the value of θ_{13} is related to the chance of finding the CP-violating phase δ (see Section 1.3.2).

Available with high fluxes and well-defined source point, $\bar{\nu}_e$ from nuclear power reactors offer a good option for θ_{13} identification. The disappearance of $\bar{\nu}_e$ can be detected in LSc detectors with high efficiency via the inverse beta decay

$$\bar{\nu}_e + p \rightarrow e^+ + n. \tag{1.29}$$

The timing coincidence between the prompt e^+ and the delayed n-capture signal is an efficient way to remove background (see Section 3). Gadolinium-loading of the LSc strongly enhances both the cross-section for n-capture and the subsequent light emission and also shortens the n-capture time. The effects of Δm^2_{21} are negligible for distances $L \approx 1\,\text{km}$ and energies $E < 10\,\text{MeV}$, so that $P(\bar{\nu}_e \rightarrow \bar{\nu}_e)$ mainly depends on $\sin^2 2\theta_{13}$ while $\left|\Delta m^2_{31}\right| \approx \left|\Delta m^2_{32}\right|$. Like in beam experiments, near detectors help to reduce flux uncertainties.

The major contributions in this field come from the Daya Bay [33], RENO [34] and Double Chooz [35] experiments. Daya Bay operates eight identical detector tanks filled each with 20 t of Gd-loaded LSc at flux-weighted baselines of 470 m, 576 m, and 1383 m, respectively. RENO consists of two identical tanks filled with each 16.5 t of Gd-loaded LSc at flux-weighted distances of 294 m and 1383 m, respectively. Double Chooz started measurement in 2010 with its far detector at a 1000 m baseline, joined in 2014 by the near detector at a 400 m baseline. Both detectors hold 10 m^3 of Gd-loaded LSc.

Being approved around 2005, all three of them released first results in 2012, claiming non-zero values for θ_{13}. The latest results are displayed in Figure 1.6.

Another option for θ_{13} measurement is the search for ν_e appearance in a long baseline ν_μ beam experiment. However, given the huge success of reactor experiments, the current and future beam experiments concentrate mostly on open issues like CP phase determination. For comparison, the result from the T2K study is included in Figure 1.6.

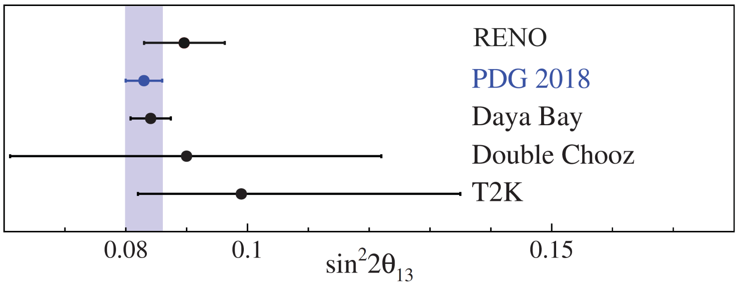

Figure 1.6: Comparison of experimental results on $\sin^2 2\theta_{13}$. Adapted from [34].

1.3 Open Questions

Although the present generation of neutrino detectors allow precise measurements of oscillation parameters, some major questions regarding neutrinos still remain unanswered. The following sections address the oscillation-related searches for neutrino mass ordering and the CP violating phase. This is followed by comments on the absolute mass scale, the particle nature (Dirac or Majorana particle) and sterile neutrinos.

1.3.1 Mass Ordering

Two independent mass splittings $\Delta m^2_{ij} = m^2_i - m^2_j$ can be deduced from the neutrino oscillations with three known flavours. While the sign of m^2_{21} is known to be positive from matter effects in the sun (see Section 1.2.1), no actual experiment has been sensitive on the sign of m^2_{32} so far. This leaves open two options for a possible mass ordering (MO): Either $m_1 < m_2 < m3$, the case in which one speaks of normal ordering (NO), or $m_3 < m_1 < m_2$, referred to as inverted ordering (IO). The two cases are illustrated on the left (NO) and right (IO) side of Figure 1.7. Here, blue, red, and yellow mark the admixtures of ν_e, ν_μ, and ν_τ to the mass states, respectively. Since no value for the CP violating phase δ has definitely been excluded yet (see Section 1.3.2), its effect was considered on the full range from 0 to 2π.

The question of MO is highly important for other physics searches, so do the measurements of the CP phase δ and the unknown octant of θ_{23} depend strongly on the correct ordering. Further consequences arise for searches for neutrinoless double beta decay (see Section 1.3.4), as well as for cosmological and astrophysical measurements [37, 38] and neutrino mass models [39].

Today, there are three major approaches to reveal the MO. Neutrino telescopes and long baseline beam experiments are sensitive on matter effects in the Earth. By contrast, medium baseline reactor experiments study oscillations with high energy resolution re-

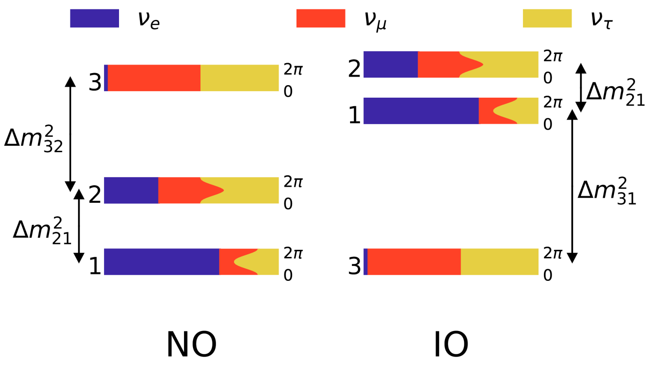

Figure 1.7: Illustration of normal and inverted mass ordering. Blue, red, and yellow mark the admixtures of ν_e, ν_μ, and ν_τ to the mass states, respectively. The effect of δ was considered on the full range from 0 to 2π. Taken from [36].

gardless of matter effects. Moreover, the problem can be faced by observations of the cosmic microwave background from cosmology experiments. The methods will be discussed in the following before reviewing the status of current global fits. Beyond that, [36] and [40] provide a good overview on current MO searches.

MO from Oscillations with Matter Effects Matter effects in the oscillation can be utilised to determine the sign of Δm^2_{32}, as it was also done for the small mass splitting Δm^2_{21}. The framework established in Section 1.1.2 can be applied to describe the oscillation of ν_μ and $\bar{\nu}_\mu$ into an effective second flavour. As apparent from the effective mass mixing angle given by Equation (1.15), the oscillation undergoes a matter-induced resonance depending on $\frac{A}{\Delta m^2_{32}}$, where A is the matter potential given by Equation (1.12). This means that the oscillation probability gets enhanced for NO. Since A is negative for $\bar{\nu}$, here an enhancement should be observed only for IO. According to Equation (1.16), resonance behaviour is expected for neutrino energies between 3 GeV and 8 GeV.

When taking into account the oscillation length given by Equation (1.20), both atmospheric and long baseline beam neutrinos emerge as suitable for respective experiments. The atmospheric neutrino fluxes are well studied, and there are baselines from tens of km to more than $13,000\,\text{km}$ (see Section 1.2.2).

Figure 1.8 shows the survival probability $P(\nu_\mu \rightarrow \nu\mu)$ for atmospheric neutrinos as a plot over energy E and zenith angle $\cos\theta_z$ for both normal (left) and inverted (right) ordering. Compared to the regular oscillation pattern in the IO case, where no matter resonance is expected, the plot for NO shows distortions in the resonance energy region of a few GeV for values $\cos\theta_z < -0.5$, i.e. neutrinos that have passed a considerable fraction of the Earth. For $\bar{\nu}_\mu$, the patterns would switch.

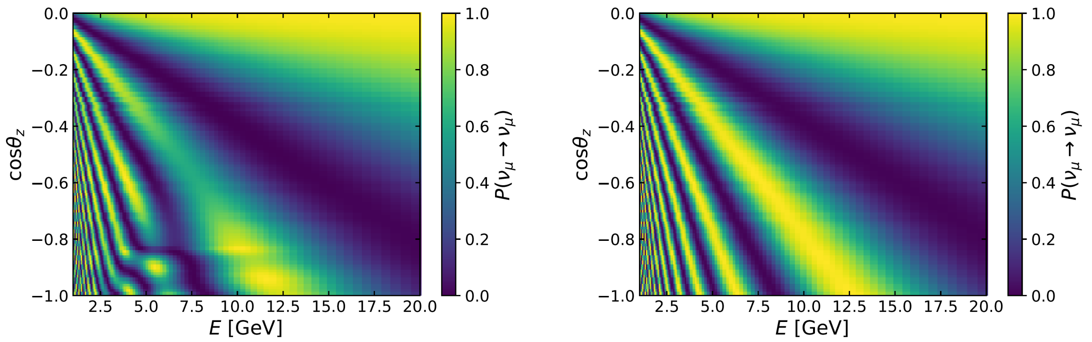

Figure 1.8: Survival probability $P(\nu_\mu \rightarrow \nu\mu)$ for atmospheric neutrinos as a plot over energy E and zenith angle $\cos\theta_z$ for both normal (left) and inverted (right) ordering. Taken from [36].

Present detectors that observe atmospheric neutrinos, including Super-Kamiokande (SK) and the MINOS far detector, suffer from the difficulty in separating charge, i.e. to tell particle from antiparticle events, and from low statistics. Larger tanks like the proposed Hyper-Kamiokande (HK) with ten times the size of its predecessor SK could partly compensate for that [41]. An alternative to the dimensionally limited construction of WC tanks is the instrumentation of natural Cherenkov media like sea water and Antarctic ice by so-called neutrino telescopes [42]. The event signatures for ν_μ and ν_e are basically the presence (track-like) or absence (cascade like) of a muon track, respectively, which can be interpreted from the hit patterns by neural networks. A clean charge separation is not possible, though. The analyses rely on the known differences in cross sections for ν and $\bar{\nu}$ shaping the flux expectations. The energy threshold depends strongly on the density of optical modules.

For IceCube (see Section 1.2.2) it is planned to deploy 26 strings of 192 optical modules each as a denser-instrumented subdetector called PINGU [43]. PINGU will have an effective mass of 6 Mt and can detect neutrinos with energies down to 2 GeV. The measurement of ν_μ disappearance will be flanked by measurements of ν_e and ν_τ appearance. The sensitivity on MO is expected do reach $3\,\sigma$ within 5 years of operation. Depending on the actual values of δ and θ_{23}, this conservative statement could be further tightened. In the current setup, IceCube reported a loose preference of NO based on data from the denser-instrumented subdetector DeepCore [44].

As part of the KM3NeT project [45], ORCA will install at least 50 detector strings of 20 optical modules each in the Mediterranean sea in order to equip more than 2 Mt of water. In that way, neutrinos with energies higher than 5 GeV can be reconstructed. Depending on the final setup, the MO could be determined with $3\,\sigma$ sensitivity within only 3 years of measurement with similar techniques as in PINGU.

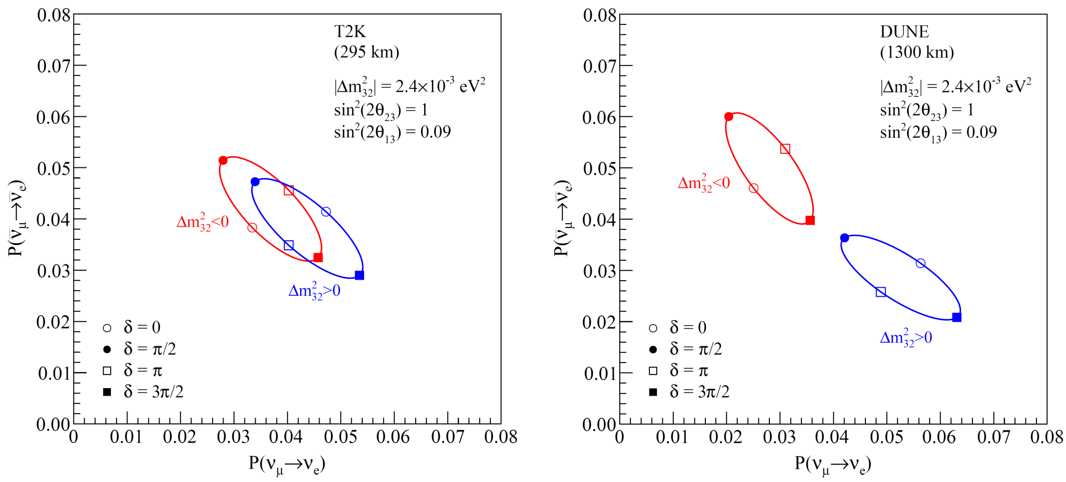

Figure 1.9: Oscillation probability from μ-like to e-like flavour for antineutrinos and neutrinos. The possible values for δ result in an ellipse each for NO and IO, depicted in blue and red, respectively. The left panel corresponds to a 295 km baseline as realized for T2K or the future upgrade T2HK. The right panel corresponds to the DUNE baseline of 1300 km. Taken from [40].

Unlike neutrino telescopes, neutrino beam experiments profit from narrow energy bands, well-defined particle IDs and fixed baselines (see Section 1.2.2) [46]. At the same time, they are limited in distance due to the inevitable widening of the beam. Long baselines are required for matter to take effect on the oscillation. Figure 1.9 illustrates how the determination of MO is related to the value of δ. The oscillation probability from μ-like to e-like flavour is plotted for antineutrinos against neutrinos. The possible values for δ result in an ellipse each for NO and IO, depicted in blue and red, respectively. The left panel corresponds to a 295 km baseline as realized for T2K or the future upgrade T2HK. Here, degeneracies arise in large parts of the allowed δ range. By assuming increasing baselines, the ellipses get pulled apart. A small overlap persists in case of a NOνA-like baseline of 810 km, full separation is reached at 1300 km as depicted in the right panel of Figure 1.9. The latter baseline is targeted for DUNE [47], an upcoming very long baseline experiment. A liquid argon time-projection chamber detector with up to 40 kt target mass is planned to receive an intense neutrino beam from Fermilab at a deep underground far site, additional to a near detector a few hundred meters away from the neutrino source. The setup promises 5 σ precision on MO after 10 years of operation and up to 10 σ depending on the parameter configuration of δ and θ_{23}.

Latest results from NOνA disfavour IO with at least 2 σ for all choices of the remaining oscillation parameters [48].

MO from Oscillations without Matter Effects

MO from Oscillations without Matter Effects Matter effects are not the only imprint of MO in neutrino oscillations. Medium baseline experiments at a distance of roughly 50 km to nuclear power reactors are a promising alternative to long baseline approaches. The survival probability of the $\bar{\nu}_e$ is given by

$$\begin{aligned} P(\bar{\nu}_e \rightarrow \bar{\nu}_e) &= 1 - \sin^2 2\theta_{13}(\cos^2\theta_{12}\sin^2\Delta_{31} + \sin^2\theta_{12}\sin^2\Delta_{32}) \\ &\quad - \cos^4\theta_{13}\sin^2 2\theta_{12}\sin^2\Delta_{21} \\ &= 1 - \frac{1}{2}\sin^2 2\theta_{13}\left[1 - \sqrt{1 - \sin^2 2\theta_{12}\sin^2\Delta_{21}}\cos(2|\Delta_{ee}| \pm \phi)\right] \\ &\quad - \cos^4\theta_{13}\sin^2 2\theta_{12}\sin^2\Delta_{21}, \end{aligned} \tag{1.30}$$

where $\Delta_{ij} = \Delta m^2_{ij}L/4E$, L is the baseline and E is the neutrino energy. ϕ is defined by

$$\begin{aligned} \sin\phi &= \frac{\cos^2\theta_{12}\sin\left(2s^2_{12}\Delta_{21}\right) - \sin^2\theta_{12}\sin\left(2c^2_{12}\Delta_{21}\right)}{\sqrt{1 - \sin^2 2\theta_{12}\sin^2\Delta_{21}}} \qquad \text{and} \\ \cos\phi &= \frac{\cos^2\theta_{12}\cos\left(2s^2_{12}\Delta_{21}\right) + \sin^2\theta_{12}\cos\left(2c^2_{12}\Delta_{21}\right)}{\sqrt{1 - \sin^2 2\theta_{12}\sin^2\Delta_{21}}}. \end{aligned} \tag{1.31}$$

Furthermore, the mass splitting

$$\Delta m^2_{ee} = \cos^2\theta_{12}\Delta m^2_{31} + \sin^2\theta_{12}\Delta m^2_{32} \tag{1.32}$$

is introduced. In Equation (1.30) the MO manifests itself in the sign of ϕ which is positive for NO and negative for IO. The term is proportional to $\sin^2\theta_{13}$ and thus the non-vanishing value which was found for $\sin^2\theta_{13}$ makes the MO experimentally accessible. ϕ very subtly affects the frequency of the subdominant oscillation in $P(\bar{\nu}_e \rightarrow \bar{\nu}_e)$. The two possible curves get maximally out of phase at the solar oscillation maximum, which lies around distances $L \simeq 53$ km for reactor neutrinos. This behaviour can be seen in Figure 1.10. A black dashed line indicates the survival probability as a function of energy when only the dominating last term characterised by the solar mixing parameters θ_{12} and Δm^2_{12} is considered in the calculation. In the full picture, a small oscillation is added on top of the solar, depicted by a red (NO) and blue (IO) line, respectively. While coinciding loosely below 2 MeV and above 5 MeV, the lines get completely out of phase between 3 MeV and 4 MeV. This behaviour can be studied and identified very effectively in Fourier transforms of the spectrum. However, a MO determination via such analyses requires high statistics and excellent energy resolution.

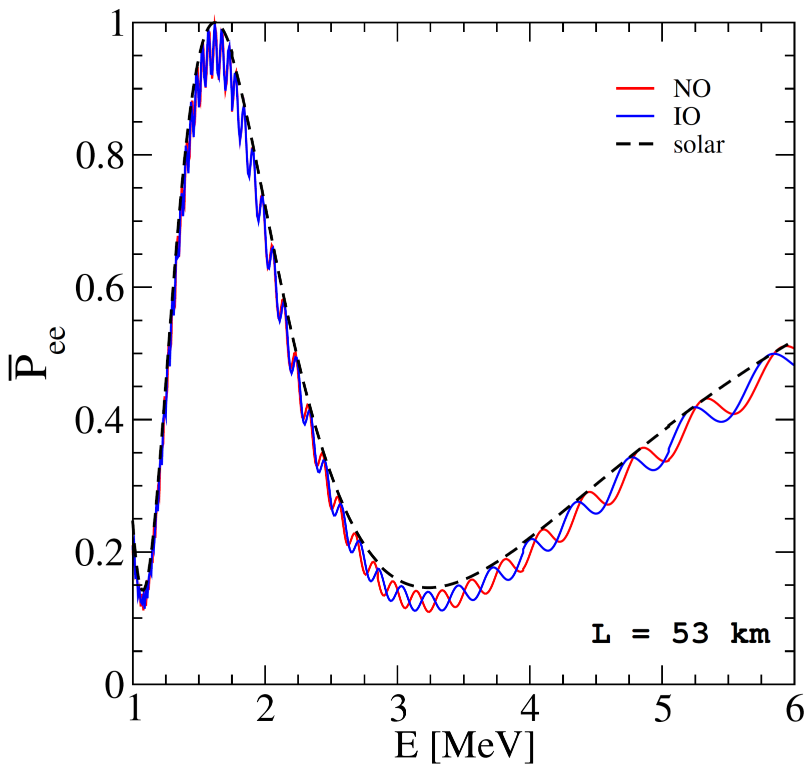

Figure 1.10: Survival probability for a reactor $\bar{\nu}_e$ flux measurement at 53 km distance. The dashed black line indicates the contribution from the dominating solar mixing parameters. Taking into account all parameters results in the red and blue line for NO and IO, respectively. Taken from [36].

JUNO [1] is a 20 kt LSc tank currently built in the South of China in an appropriate distance to two nuclear power plants. The experiment is intended to resolve the subdominant oscillation around the solar oscillation maximum and thus determine the MO. 10^5 events are expected within 6 years of measurement, leading to a significance of more than $3\,\sigma$. JUNO is described in detail in Chapter 3.

MO from Cosmology Cosmology opens up a path to MO determination very complementary to oscillations. Neutrinos play their part in the cosmological expansion history and in the perturbation evolution and therefore affect cosmological observables [36]. Although the masses m_i are not individually accessible, the current generation of experiments shows some sensitivity to their direct sum $\sum m_i$. Depending on the MO, $\sum m_i$ can be expressed in terms of the smallest m_i and the known mass splittings:

$$\begin{aligned}\sum_i m_i^{\mathrm{NO}} &= m_1 + \sqrt{m_1^2 + \Delta m_{21}^2} + \sqrt{m_1^2 + \Delta m_{31}^2},\\ \sum_i m_i^{\mathrm{IO}} &= m_3 + \sqrt{m_3^2 + \left|\Delta m_{31}^2\right|} + \sqrt{m_3^2 + \left|\Delta m_{31}^2\right| + \Delta m_{21}^2}.\end{aligned} \tag{1.33}$$

As a consequence, minimum values can be concluded to be $\sum m_i^{\mathrm{NO,min}} \sim 0.06\,\mathrm{eV}$ and $\sum m_i^{\mathrm{IO,min}} \sim 0.10\,\mathrm{eV}$. Thus, IO could in principle be excluded by constraining $\sum m_i$.

The observation of cosmic microwave background (CMB) was a major purpose of the Planck mission. The CMB anisotropies can be mapped in terms of temperature and polarisation with small angular resolution. The effect of neutrino masses on the relative expansion of the universe is imprinted on the power spectra as a function of the angular scale. This includes the height of the first peak, the peak positions, and the slope of the CMB tail. While the latter is hard to obtain with the given accuracy, the other characteristics share degeneracies with cosmological parameters, and especially the Hubble constant H_0. Planck results from 2018 [49] report upper bounds at 95 % CL for $\sum m_i$ between 0.54 eV and 0.26 eV, depending on the included features of the power spectrum.

As for the degeneracy with H_0 it is helpful to include CMB lensing, i.e. the distortions of photon paths due to gravitational effects from matter inhomogeneities. The deviation from Gaussian smearing in the CMB temperature and polarisation maps can be measured in order to study the lensing potential at different scales. A suppression of the lensing effect is expected at small scales from neutrinos. Inclusion of the lensing effect yields $\sum m_i < 0.24\,\mathrm{eV}$.

$\sum m_i$ is also encoded in the large scale structure of the universe. Mapping the visible baryonic matter reveals structural features in the mass correlation function, i.e.

assessing the distances between each two objects. Neutrinos, being hot dark matter, leave a different trace on structure growth than pure cold dark matter, and especially lead to a suppression of fluctuations at scales below the neutrino free streaming length. Furthermore, a large bump in the mass correlation function, known as Baryon Acoustic Oscillation (BAO), is related to the distance a sound wave can travel in the hot plasma of photons and baryons of the early universe. The gravitational influence of supersonic neutrinos leads to a shift of the peak. This can be exploited to extract $\sum m_i$.

The Lyman-α forest, a series of absorption lines obtained in distant quasars, can also constitute a flux power spectrum that is sensitive on small scales at large redshift. Here, the impact of neutrinos is larger and effects related to dark energy are small.

Major surveys of the large scale structure of the universe include SDSS [50] and DES [51]. Combined with CMB data, neutrino masses can be constrained to $\sum m_i < 0.12\,\mathrm{eV}$ at 95% CL [49]. This puts light pressure on the bounds of $\sum m_i$ for IO.

Care has to be taken regarding the cosmological model: Considerable changes and uncertainties would be generated when departing from the standard ΛCDM scenario which has been assumed in all above constraints. It therefore remains indispensable to determine the MO in a terrestrial measurement.

Other Methods Oscillation measurements and cosmological surveys are the most realistic approaches to reveal MO. In principle, there are further methods with sensitivity to the MO, two of which shall be mentioned here.

The shape of β decay spectra is affected by neutrino masses near the endpoint due to the fact that a part of the Q-value Q_β goes into the neutrino mass m_i. Depicted in a Kurie plot [52], the electron spectrum follows the Kurie function

$$K(T) = \left[(Q_\beta - T) \sum_{i=1}^{N} |U_{ei}|^2 \sqrt{(Q_\beta - T)^2 - m_i^2} \cdot \Theta(Q_\beta - T - m_i) \right]^{1/2}, \qquad (1.34)$$

in which T is the kinetic energy of the emitted electrons, N the number of neutrino masses, U_{ei} the PMNS matrix element with respect to electron flavour, and Θ the Heaviside step function. The Kurie function would, in absence of neutrino masses, cross the T axis at Q_β. Neutrino masses suppress the spectrum and individually shift the endpoint to lower energies. Remarkably, the principle works without prior knowledge on the number of neutrino flavours and thus offers a very model-independent way for mass measurements. However, the present generation of experiments, e.g. KATRIN (see Section 1.3.3), are far from reaching the statistics and energy resolution required for an observation of single-flavour effects.

Indirectly, also the search for neutrinoless double beta decay ($0\nu\beta\beta$) is related to the MO by measuring the effective Majorana mass $|m_{\beta\beta}|$. As depicted in the left panel of Figure 1.12 and explained in Section 1.3.4, $|m_{\beta\beta}|$ as a function of the lightest neutrino mass m_{lightest} splits into two allowed bands: one for NO and one for IO. By setting upper limits on $|m_{\beta\beta}|$, the allowed region for IO can gradually be excluded. As for the sensitivity of $0\nu\beta\beta$ experiments on the one hand, the goal seems reachable in near future. On the other hand, there are some flaws in the plan with regard to MO: Firstly, the statement is only valid if neutrinos are Majorana particles, and therefore the absence of $0\nu\beta\beta$ is not sufficient for an exclusion (see Section 1.3.4). Secondly, the plot changes drastically under the assumption of sterile neutrino flavours (see Section 1.3.5). In this case, the allowed bands for NO and IO share large regions in the parameter space as can be seen in the right panel of Figure 1.12. Last but not least, the plotted relation depends on the underlying $0\nu\beta\beta$ process – a variable no experiment is sensitive to, which must be taken into account in the interpretation.

Recent Global Fits From the present generation of experiments, no facility is sensitive enough to exclude one ordering individually, yet the combination of complementary approaches yields high potential. [53] describes a global fit based on the three-neutrino picture that includes data from various oscillation experiments. The fit favours NO at $3.4\,\sigma$. An important contribution comes from a tension in the preferred value for θ_{13} from reactor and long-baseline experiments (see Figure 1.6), which is higher for IO. The same holds for the mismatch in the atmospheric mass splitting (see Section 1.2.2).

In [36], the result from the oscillation fit was further combined with data from $0\nu\beta\beta$ and cosmological experiments in a Bayesian analysis. As expected the current $0\nu\beta\beta$ results did not have much of an impact. The cosmological bounds on $\sum m_i$ increased the hint on NO to $3.5\,\sigma$.

1.3.2 CP Violating Phase

The excess of matter over antimatter in our universe is an unsolved mystery in modern cosmology [54]. One plausible explanation for the imbalance is CP violation. This would mean that physical processes could not be described equally under a switch of both charge (C) and parity (P). Although CP violation has been found in the quark sector, namely for K-mesons and B-mesons [55, 56], the effect of this phenomenon, known as CKM-mixing, is too small to explain the asymmetry.

Since neutrinos are known to have masses, CP-violating flavour oscillations could

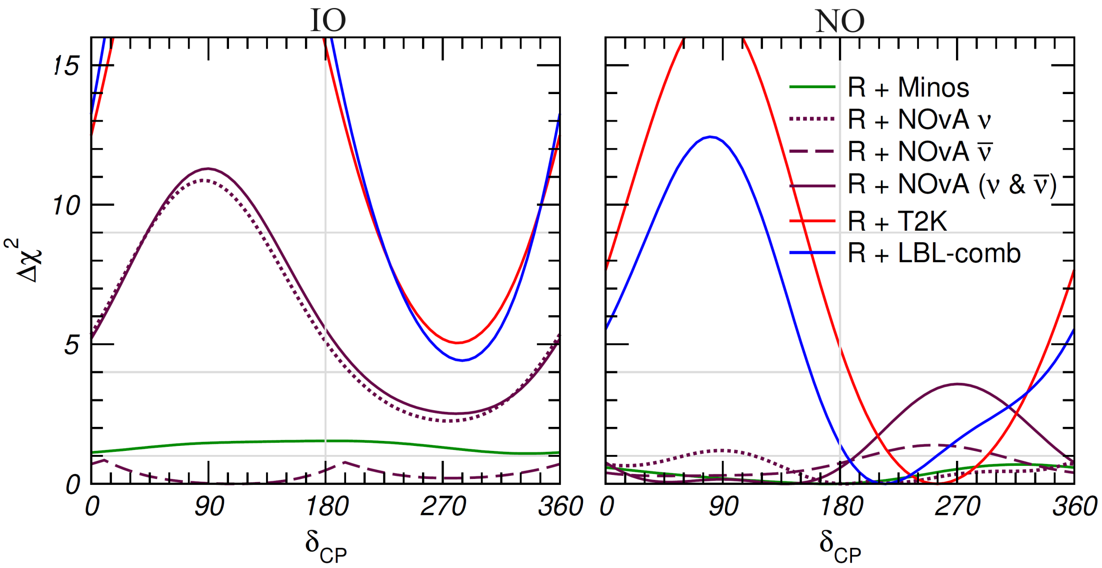

Figure 1.11: Combined analysis for δ determination using data from reactor and accelerator-based long baseline beam experiments. $\Delta\chi^2$ is plotted as a function of δ for MINOS, NOνA, T2K, and a combination of all three. IO is assumed in the left and NO in the right panel. Reactor and beam data was used in order to fit θ_{13}, θ_{23}, and Δm^2_{32}. The solar mixing parameters were fixed to the global best fit values. Taken from [12].

represent another piece in this puzzle. The option is formally considered by introducing the phase δ to the weak mixing matrix U_{PMNS}. In the parametrisation given by Equation (1.18) it can be seen that every occurrence of δ is accompanied by the factor $\sin\theta_{13}$. Therefore, the measurement of a non-vanishing mixing angle θ_{13} (see Section 1.2.3) raised hopes for a measurement of δ.

The common approach for the phase determination is to compare the appearance of ν_e and $\bar{\nu}_e$ in a beam of ν_μ and $\bar{\nu}_\mu$, respectively. Full knowledge of all remaining mixing parameters is required to avoid degeneracies. Especially the sign of $|\Delta m^2_{32}|$, i.e. the mass ordering, and the large uncertainties in $\sin^2\theta_{23}$ have a large impact here. For IO, a value $\delta \simeq \pi/2$ suppresses ν_e and enhances $\bar{\nu}_e$ events. For NO, the opposite effect is expected for $\delta \simeq 3\pi/2$. Matter effects lead to a further enhancement of ν_e for NO, while $\bar{\nu}_e$ are suppressed. The opposite is the case for IO. Meanwhile, a higher value for $\sin^2\theta_{23}$ increases the number of both ν_e and $\bar{\nu}_e$ events. No effect is expected for $\delta = 0$ or $\delta = \pi$. See [12] for a more detailed discussion.

Figure 1.11 shows the results of a combined analysis using data from reactor and accelerator-based long baseline beam experiments. Both reactor and beam data was used in order to fit θ_{13}, θ_{23}, and Δm^2_{32}. The solar mixing parameters were fixed to the global best fit values. The $\Delta\chi^2$ is plotted as a function of δ for MINOS, NOνA, T2K, and a combination of all three – for IO in the left and NO in the right panel. The combination of reactor and T2K data (red line) confirms CP-violation with more than $2\,\sigma$. In the case of IO, the preferred δ region lies around $\delta \simeq 3\pi/2$ for T2K and NOνA (purple lines). In the case of NO, T2K prefers a similar value while NOνA mildly disfavours this region.

In the future, the planned experiments DUNE and Hyper-K could measure δ with high significance [46]. With 1300 km baseline and a wider energy band, DUNE can be regarded as complementary to Hyper-K with 295 km baseline and a very narrow spectrum.

1.3.3 Absolute Masses

Flavour oscillations affirm neutrino masses but do only reveal differences and not the absolute mass scale. At least it is straightforward to derive lower limits from the oscillation mass splittings under the assumption that the lightest mass equals zero.

As already pointed out in Section 1.3.1, the high energy end of beta decay spectra – or their representation in Kurie plots given by Equation (1.34) – can in principle probe the individual masses m_i. Under laboratory conditions however, poor statistics near the endpoint oblige experiments to subsume larger energy regions in order to increase luminosity. This results in a measurement of the effective neutrino mass

$$m_\beta = \sqrt{\sum_i |U_{ei}|^2 m_i^2}, \tag{1.35}$$

where the U_{ei} denote the PMNS matrix elements with respect to the electron flavour. As a source, tritium is conveniently used due to a low Q-value and its simple structure which facilitates model calculations. Likewise, the Troitsk [57] and Mainz [58] experiments could give an upper limit of $\sim 2\,\mathrm{eV}$ on m_β. KATRIN [59] uses similar techniques at a much larger scale and is soon expected to lower this bound by a factor of 10. Future experiments like Project 8 [60] could reach below $5 \cdot 10^{-2}\,\mathrm{eV}$, which is the minimum m_β for IO.

Since massive neutrinos have an impact on cosmological expansion and perturbation evolution, neutrinos leave their traces also on cosmological observables. Sky survey experiments can give upper bounds on the direct sum of neutrino masses, constraining $\sum m_i$ to 0.12 eV at 95 % CL (see Section 1.3.1).

If neutrinos are Majorana particles, experiments searching for neutrinoless double beta decay are sensitive on yet another mass definition by the name of effective Majorana mass $|m_{\beta\beta}|$, given by Equation (1.37). Current upper limits are in the order of 0.1 eV, see also Section 1.3.4.

1.3.4 Dirac or Majorana Particle

Neutrino oscillations and hence the existence of neutrino masses raised the question whether neutrinos are their own antiparticles, so-called Majorana particles [61, 7, 6]. In contrast to all other SM fermions, the absence of charge makes the idea conceivable. The question is strongly related to the process that gives mass to neutrinos, as it will be explained in the following.

Originally, neutrino masslessness was assumed in the SM as a consequence of Lagrangian invariance under local gauge transformations. Chirally right-handed neutrino fields were not needed to formulate the unification of the weak and electromagnetic interaction, and were therefore left out. However, for Dirac neutrinos in order to possess mass, the Dirac mass term in the Lagrangian needs a right handed component, otherwise no Yukawa coupling to the Higgs field is possible. The introduction of such a right handed field would make massive neutrinos compatible with the SM.

An alternative to right handed fields in the Dirac mass term is to expand the Lagrangian by a Majorana mass term, describing a particle that is identical to its antiparticle [6, 7]. This option implies that the origin of neutrino masses is different from all other SM fermions. The Majorana scenario is preferred by most Grand Unified Theories since it can explain why neutrino masses are so small. The three known left-handed neutrinos are complemented by three additional right-handed partners. Their masses are connected via the see-saw mechanism: It follows from the mass term that the masses of the left-handed neutrinos are inversely proportional to the right-handed partners.

A theorem by J. Schechter and J. Valle [62] states that the Majorana nature of neutrinos can be proven with the detection of neutrinoless double beta decay ($0\nu\beta\beta$). According to

$$(A, Z) \rightarrow (A, Z + 2) + 2e^- + Q_{\beta\beta}, \tag{1.36}$$

a parent nucleus with atomic nuber A and proton number Z undergoes two simultaneous beta decays under the release of the respective Q value $Q_{\beta\beta}$ and two electrons. The remarkable thing is that the two neutrinos that accompany a SM-allowed variant of the decay, are missing in the process, thus violating the total lepton number by two units.

$0\nu\beta\beta$ half lives $T_{1/2}$ are expected to be larger than 10^{24} years, making a detection extremely challenging in terms of background reduction. $T_{1/2}$ is inversely proportional to the effective Majorana mass $|m_{\beta\beta}|$ squared, the latter being an observable that can be compared for different isotopes. It is defined as the coherent mass of neutrino masses

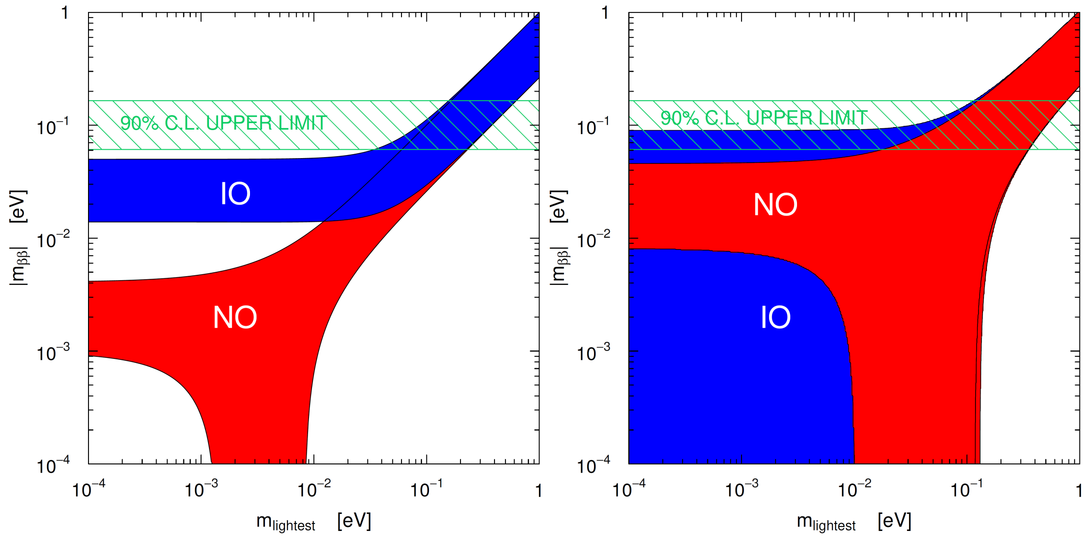

Figure 1.12: Effective Majorana mass as a function of the lightest neutrino mass. Two bands represent the allowed regions for NO and IO, respectively. The left plot shows the three-flavour case, whereas the right plot is based on a scenario with one additional sterile flavour. Taken from [36].

according to

$$|m_{\beta\beta}| = \left|\sum_i U_{ei}^2 m_i\right|, \tag{1.37}$$

with the U_{ei} being the elements of the weak mixing matrix with respect to the electron flavour. Note that for Majorana neutrinos with three active flavours two additional phases enter the matrix as shown in Equation (1.19).

The left panel of Figure 1.12 shows $|m_{\beta\beta}|$ as a function of the lightest neutrino mass. Depending on the MO, two allowed bands appear, broadened due to the unknown Majorana phases plus uncertainties of the standard mixing parameters. However, this picture is highly model-dependent: Only for one specific out of various decay channels satisfying Equation (1.36) does the shape apply. Furthermore, in the presence of further neutrino flavours (see Section 1.3.5) the allowed regions completely change and become degenerate at large parts as it is depicted in the right panel of Figure 1.12. Experiments searching for $0\nu\beta\beta$ give upper limits on $|m_{\beta\beta}|$ and thus exclude plot regions from the top. The currently tightest upper bounds come from GERDA [63] ($0.12-0.26$ eV at 90 % CL), a semiconductor detector looking for the decay in ^{76}Ge, CUORE [64] ($0.11-0.52$ eV at 90 % CL), which uses tellurium dioxide bolometers to probe ^{130}Te, and KamLAND-Zen [65] ($0.061-0.165$ eV at 90 % CL), the former KamLAND with the source isotope ^{136}Xe solved in the liquid scintillator.

Future experiments like LEGEND [66] and nEXO [67] plan to fully exclude the IO band by upscaling the source material to the ton scale. If however $0\nu\beta\beta$ remains unobserved, no definite conclusion regarding MO can be drawn from that – since it remains unclear if neutrinos are Majorana particles after all.

1.3.5 Sterile Neutrinos

Since neutrinos take part in the weak interaction, their number can be derived from the decay width of the Z^0 mediator which has the mass $m_Z = 91\,\mathrm{GeV}$ [5]. The experimental result confirms the number of active neutrinos with masses below $\frac{m_Z}{2}$ to be $N_\nu = 2.984 \pm 0.008$ [5]. However, N_ν does not include neutrino flavours that do not interact weakly, usually referred to as sterile.

Flux anomalies in solar neutrino experiments based on gallium [68], as well as in reactor [69] and beamline [70, 71] neutrino experiments suggested that neutrinos oscillate into at least one undetectable flavour at short baselines below 1 km, before the effect of known flavour oscillations sets in. For reactor neutrinos on the one hand, the possibility of inaccurate predictions could be ruled out by flux measurements with movable detectors. The data prefers sterile neutrino oscillations at more than $3\,\sigma$ with $\Delta m^2_{41} \approx \mathrm{eV}^2$ and $|U_{e4}| \approx 0.1$ in a four-flavour picture. The beamline anomalies on the other hand are contradicted by recent appearance and disappearance data from MINOS+ and IceCube [72]. It was found that neither one nor more additional flavours fit the data consistently [72].

It is worth mentioning that the presence of sterile neutrino oscillation would mean the three flavour mixing matrix to be non-unitary. The latter would rather act as a sub-matrix of the actual U.

Apart from light also heavy sterile neutrinos are under discussion. As mentioned in Section 1.3.4, the Majorana nature of neutrinos would lead to heavy right-handed flavours via the see-saw effect. Masses in the keV range would make them a good candidate for warm dark matter. Masses in the order of GeV would range them cold dark matter, a fact that could help explain the matter-antimatter asymmetry of the Universe. Due to kinematics, heavy neutrinos would not take part in the oscillations of light flavours.

Finally, cosmology provides complementary measurements of light neutrino flavours. Planck constrained the effective number N_{eff} of relativistic species, i.e. the sum of active and sterile flavours at the time of Big Bang nucleosynthesis to be slightly larger than 3, depending on the combination of data sets [49]. Notably, the interpretation of cosmological data is strongly model dependent and N_{eff} can be weakened or even inapplicable when departing from the minimal ΛCDM model.

Chapter 2

Particle Detection in Liquid Scintillator Detectors

Scintillation ranges among the oldest techniques for the detection of nuclear radiation and particles. The principle is simple: Ionising radiation deposits energy in the bulk material, which subsequently releases a part of this energy in the form of visible light. The light emission happens on short time scales and can be detected either by eye or by appropriate electronic sensors based on the photoelectric effect. Scintillators come at reasonable cost and in manifold types: Either inorganic crystals or organic material in gaseous, liquid, or solid form, making them applicable for a wide field of experiments. Furthermore, the almost linear relation between number of emitted photons and deposited energy enables calorimetry.

In present neutrino experiments, liquid scintillator (LSc) enjoys great popularity due to the low energy threshold. In large detectors it lies around a few hundred keV, whereas this limit is determined by the trigger threshold which in turn is mainly due to the dark noise of the light sensors. In comparison, water-Cherenkov (WC) detectors are not sensitive to particles below 3 MeV. This makes LSc technology suitable especially for the detection of reactor neutrinos, solar neutrinos, and neutrinoless double beta decay.

This chapter passes though the detection chain of an organic LSc experiment. Starting with the energy deposition of particles in Section 2.1, the process of light emission is treated in Section 2.2, followed by light propagation in Section 2.3 and detection in Section 2.4. An outlook on LSc technology is finally given in Section 2.5.

2.1 Energy Deposition

In particle detectors neutrinos are identified indirectly via the residual ionising components from interactions. Accordingly, the energy loss of charged particles and gammas will be discussed below. Some additional comments are made on the detection of neutrons as part of the inverse beta decay signal.

2.1.1 Charged Particles

The interactions of fast charged particles with matter – and hence the differential energy loss – depend strongly on the particle velocity, in the following expressed by $\beta\gamma$ with β being the velocity over speed of light c and γ being the Lorentz factor. For moderate velocities $0.1 \lesssim \beta\gamma \lesssim 1000$, energy loss is dominated by ionisation and excitation. For particles with masses m much higher than the electron mass m_e, the mean loss of energy E per unit length x is well-described by the Bethe equation [5]

$$\left\langle -\frac{\mathrm{d}E}{\mathrm{d}x} \right\rangle = Kz^2 \frac{Z}{A} \frac{1}{\beta^2} \left[\frac{1}{2} \ln \frac{2m_e c^2 \beta^2 \gamma^2 W_{\mathrm{max}}}{I^2} - \beta^2 - \frac{\delta(\beta\gamma)}{2} \right]. \tag{2.1}$$

Herein, $K = 4\pi N_A r_e^2 m_e c^2$ is a constant coefficient comprising the Avogadro constant N_A and the classical electron radius r_e, z is the charge number of the incident particle, Z and A are the atomic number and mass of the absorber, respectively, W_{max} is the maximum energy transfer in a single collision, I is the mean excitation energy, and $\delta(\beta\gamma)$ denotes a density effect correction. The function decreases with $1/\beta^2$ towards $\beta\gamma \approx 4$, where a minimum is reached. From then on, the logarithmic part takes over and results in an increase with about $2\ln\gamma$. It has to be stressed that the actual energy deposition fluctuates highly around the mean value. The electronic interactions occur in single collisions with mostly small energy losses, i.e. less than 100 eV [5].

Incident electrons and positrons have a special role since they and their collision partners have equal mass. An approximated description is given by

$$\left\langle -\frac{\mathrm{d}E}{\mathrm{d}x} \right\rangle = K \frac{Z}{A} \frac{1}{\beta^2} \left[\frac{1}{2} \ln \frac{\gamma m_e c^2}{2I^2} - \beta^2 - \frac{\delta^*(\beta\gamma)}{2} \right], \tag{2.2}$$

where the density effect δ^* differs slightly from the previous case [73].

Bremsstrahlung sets in at higher energies as a consequence of the Coulomb fields of shell electrons and nuclei. The losses can be described by

$$\left\langle -\frac{\mathrm{d}E}{\mathrm{d}x} \right\rangle = 4\alpha N_A \frac{Z^2}{A} z^2 \left(\frac{1}{4\pi\epsilon_0} \cdot \frac{e^2}{mc^2} \right)^2 \cdot E \cdot \ln \frac{183}{Z^{1/3}} \tag{2.3}$$

with the fine structure constant α and the vacuum permittivity ϵ_0 [73]. Remarkably, the energy losses caused by bremsstrahlung are proportional to E and inversely proportional to m^2, thus affecting incident electrons and positrons much earlier than heavier particles.

In large detectors, the reduction of kinetic energy finally causes incident particles to stop. However, due to high statistical fluctuations the range cannot be predicted precisely. The continuous slowing down approximation (CSDA) range

$$R = \int_E^0 \left\langle \frac{\mathrm{d}E}{\mathrm{d}x} \right\rangle^{-1} dE \tag{2.4}$$

can be built as an estimate, where it must be mentioned that due to the various scattering processes the overall distance gets diminished with respect to R. Electrons and positrons with energies below 10 MeV travel a few centimetres in LSc, whereas heavier charged particles are stopped within millimetres. CSDA ranges can be obtained e.g. from the NIST databases [74].

2.1.2 Gammas

Three effects mainly characterise photon interactions with matter: photo effect, Compton scattering, and pair production. Figure 2.1 (a) shows how the different processes contribute to the total cross section σ_{tot} in carbon. At low energies, σ_{tot} is clearly determined by the photoelectric effect ($\sigma_{\mathrm{p.e.}}$), i.e. photon absorption with subsequent electron emission. Minor contributions come from the elastic Rayleigh scattering off atoms and molecules ($\sigma_{\mathrm{Rayleigh}}$), and Compton scattering off electrons ($\sigma_{\mathrm{Compton}}$). Above the threshold of twice $m_e = 511\,\mathrm{keV}$ pair production sets in within the nuclear (κ_{nuc}) and electron (κ_e) fields and dominates at high energies. In between, from $\sim 50\,\mathrm{keV}$ up to several MeV, Compton scattering is the predominant process.

Gammas in the context of LSc detectors originate from nuclear state transitions, bremsstrahlung, and electron positron annihilation. Hence they have energies E between a few hundred keV and several MeV, causing mainly Compton interactions to occur. Within a Compton scattering interaction, a part of the photon energy is transferred to an electron and the photon gets deflected, now carrying the energy E'. The relative energy transfer

$$\frac{E'}{E} = \frac{1}{1 + \frac{E}{m_e c^2}(1 - \cos\theta)} \tag{2.5}$$

is a function of energy and the deflection angle θ. The maximum energy transfer at low energies of a few keV is only in the order of a few percent, whereas for a 511 keV

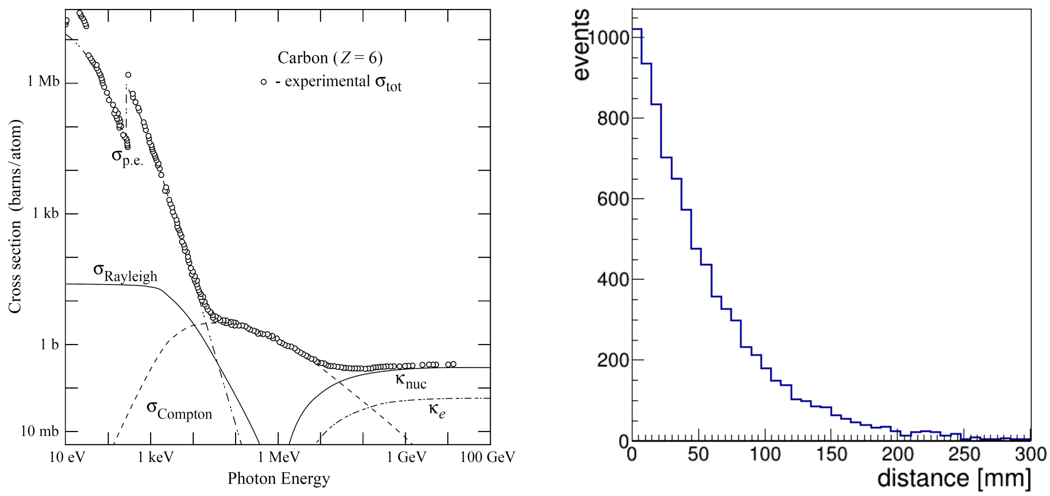

(a) Total cross section σ_{tot} for photon interaction in carbon. Additionally, the contributions from photo effect ($\sigma_{\mathrm{p.e.}}$), Rayleigh scattering ($\sigma_{\mathrm{Rayleigh}}$), Compton scattering ($\sigma_{\mathrm{Compton}}$), and pair production in the nuclear (κ_{nuc}) and electron fields (κ_e) are indicated. Taken from [5].

(b) Distance from the emission point to the point of first Compton scattering in LAB as obtained from a Geant4 simulation.

Figure 2.1: Gamma interactions in LSc.

gamma the maximum is 83 %, and approaches 100 % around 10 MeV. Therefore, multiple Compton scattering in the discussed energy range is very likely.

The mean free path for gammas between 0.5 MeV and 10 MeV shows a mild linear increase from $\sim$ 10 cm to $\sim$ 50 cm [75]. Figure 2.1 (b) shows the distance a gamma travels in LAB until the first Compton interaction takes place as obtained from a Geant4 simulation. The gammas were given uniformly distributed energies between 100 keV and 10 MeV. The histogram illustrates the strong fluctuations in the free path.

2.1.3 Neutrons

Neutrons loose their energy in elastic collisions with light nuclei rather than in ionising processes. Therefore, no calorimetric measurement is possible in LSc. When thermalised in the target, the neutron gets captured by a hydrogen nucleus which emits the free binding energy in the form of a 2.2 MeV gamma. The light sensor system can trigger on the characteristic energy release to detect neutron events.

Many experiments measuring antineutrinos dope the LSc with gadolinium in order to enhance the neutron detection, examples are Double Chooz, Daya Bay, and RENO. The effect is threefold: The cross section of natural abundant Gd for neutron capture is 49 kilo barn, and small concentrations in the LSc far below 1 % lead to strong effects on the capture rate. Also, Gd releases $\sim$ 8 MeV spread over several gammas, thus facilitating the detection. Furthermore, the delay of the caption due to previous thermalisation is shortened from $\sim$ 200 ns to $\sim$ 30 ns which significantly reduces accidental background in a positron-neutron coincidence signal [76]. A disadvantage of Gd-loading is the reduced attenuation length, leaving the detector less transparent for optical photons.

2.2 Light Emission

Most of the light emission in LSc is due to fluorescence, the actual scintillation process. However, for charged particles above the threshold energy also Cherenkov light contributes, although the fraction is at percent level. Both processes will be addressed in short.

2.2.1 Scintillation Light

The molecules in an organic scintillator feature benzene rings, so-called aromatic compounds of hydrogen and carbon. Energy absorption leads to an excitation to the first singlet state S_1 above ground state S_0. With a transition time of a few nanoseconds, the system deexcites to S_0 under the isotropic emission of light. Occasionally, a transition from S_1 to the first excited triplet state $T_1 < S_1$ takes place. If two such T_1 molecules interact, a state conversion is possible such that one molecule populates S_1 and the other S_0. A delayed deexcitation $S_1 \to S_0$ is the consequence.

A LSc typically comprises at least two components: one or more fluorescent aromatic solutes (fluors) dissolved in an aromatic solvent [77]. The solvent slows down throughgoing particles and absorbs the energy losses. The excitation energy is transferred to the primary fluor very fast in non-radiative dipole-dipole interactions. The S_1 state of the fluor lies below the corresponding solvent state, thus the emitted wavelength gets shifted. This is necessary to prevent re-absorption of the emitted light by the solvent. A fluor re-absorption is unlikely due to the low concentration of a few grams per litre solvent. A secondary fluor can be added at a concentration of milligrams per litre in order to further shift the spectrum to a range appropriate for the light sensors.

A typical solvent is pseudocumene (PC) with a peak emission at 290 nm wavelength. PC found use e.g. in KamLAND and Borexino. High toxicity and a low flashpoint of 48° C make it difficult to handle, though. Linear alkylbenzene (LAB) with a peak emission at 283 nm is less toxic and its flashpoint of 140° C makes it a safer use. LAB was the solvent e.g. in Daya Bay and RENO and will also be used for JUNO. 2,5-Diphenyloxazole (PPO) is often used as a primary fluor, its emission peaks at 305 nm. A typical secondary fluor is 1,4-Bis(2-methylstyryl)benzol (bis-MSB) with a peak emission at 425 nm. Figure 2.2 (a) shows an emission spectrum comparable to the final JUNO mixture of LAB, PPO, and bis-MSB.

It is important to know the light yield of a LSc solution for calorimetric purposes. Only about 3 % of the deposited energy goes into the release of optical photons [5]. A typical value is 10^4 photons per MeV of deposited energy. The amount of emitted light is not linear, however. The linearity is lost due to recombination and quenching effects such as differing ionisation densities and chemical impurities [77]. According to the semi-empirical Birks formula [78]

$$\frac{\mathrm{d}L}{\mathrm{d}x} = L_0 \frac{\frac{\mathrm{d}E}{\mathrm{d}x}}{1 + kB\frac{\mathrm{d}E}{\mathrm{d}x}}, \tag{2.6}$$

the luminescence per unit length $\mathrm{d}L/\mathrm{d}x$ can be described with a reference value L_0, the energy loss per unit length $\mathrm{d}E/\mathrm{d}x$, and the Birks parameter kB which depends on the material and has to be measured for each LSc mixture. Equation (2.6) implies that the light yield is energy and particle dependent.

The light emission over time t with respect to the excitation time t_0 is a statistical process which can phenomenologically be described as the sum of several exponential functions with weights ω_i and time constants τ_i:

$$\phi_{\text{em}}(t) = \sum_{i=1}^{n} \frac{\omega_i}{\tau_i} \mathrm{e}^{-\frac{t-t_0}{\tau_i}} \qquad \text{with} \qquad \sum_{i=1}^{n} \omega_i = 1. \tag{2.7}$$

The exact values for ω_i and τ_i are particle dependent due to the individual ionisation densities. This difference in pulse shape is the basis for particle discrimination techniques.

2.2.2 Cherenkov Radiation

When a charged particle traverses a dielectric medium it polarizes the molecules as it passes. If the particle velocity v is higher than the local phase velocity of light, this causes the medium to coherently response by emitting electromagnetic waves in the optical range [5]. A wavefront develops and propagates with the Cherenkov angle

$$\theta_C = \operatorname{acos}\left(\frac{1}{n\beta}\right) \tag{2.8}$$

to the particle track, where n denotes the refractive index and $\beta = v/c$ with speed of light c, thus forming the characteristic Cherenkov cone. From the threshold velocity $\beta_t = 1/n$ the requisite kinetic energy of a particle with rest mass m can be concluded to be

$$E_C \geq mc^2 \left(\frac{1}{\sqrt{1 - \frac{1}{n^2}}} - 1 \right). \tag{2.9}$$

Accordingly, the threshold energy for $n \approx 1.5$ in LSc is 210 keV for electrons and 36 MeV for muons.

The effect on the energy loss is minimal, but the Cherenkov radiation (CR) contributes to the total light yield in a LSc detector. Geant4 simulations and calculations suggest a ratio of a few percent. [79] reports a measured ratio in the same order. A clear separation in experiments is difficult, though, since both effects superimpose. Slight differences between CR and scintillation light arise from the fact that CR is emitted on the picosecond scale after energy deposition, from the directionality due to θ_C, and from the emission spectrum. The latter can be deduced from the number of emitted Cherenkov photons per unit length

$$\frac{\mathrm{d}N}{\mathrm{d}x} = 2\pi\alpha z^2 \int_{\lambda_1}^{\lambda_2} \left(1 - \frac{1}{n^2\beta^2}\right) \frac{\mathrm{d}\lambda}{\lambda^2}, \tag{2.10}$$

between two wavelengths λ_1 and λ_2, where α is the fine structure constant and z is the charge number of the throughgoing particle. When neglecting dispersion, this leads to

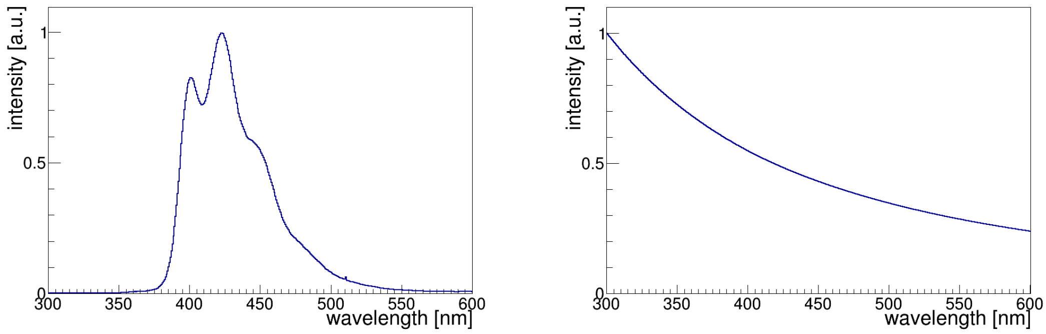

(a) Scintillation light, data provided by [80]. (b) CR, calculated according to Equation (2.10).

Figure 2.2: Emission spectra for scintillation light in a JUNO-like LSc mixture (a) and Cherenkov radiation (b). The plots are not to scale.

the Frank Tamm formula [73]

$$\frac{\mathrm{d}N}{\mathrm{d}x} = 2\pi\alpha z^2 \cdot \sin^2\theta_C \cdot \frac{\lambda_2 - \lambda_1}{\lambda_1\lambda_2}. \tag{2.11}$$

The wavelength spectrum according to Equation (2.10) is plotted in Figure 2.2 (b). Depending on the contained wavelength shifters, the CR can outshine the scintillation component at very short or very long wavelengths, as can be seen in comparison with Figure 2.2 (a).

2.3 Light Propagation

The dispersion $n = n(\lambda)$ of a medium causes photons to propagate with the group velocity

$$v_g = \frac{\mathrm{d}\omega}{\mathrm{d}k} = \frac{c}{n(\omega) + \omega(\frac{\mathrm{d}n}{\mathrm{d}\omega})}. \tag{2.12}$$

rather than with their phase velocity

$$v_p = \frac{c}{n}. \tag{2.13}$$

Here, ω denotes the frequency and $k = 2\pi/\lambda$ the wavenumber of the photon [5]. In liquid scintillator, the photon trajectory stays unchanged unless one of the following interactions takes place:

Absorption The emission spectrum of a fluorescent material is not necessarily congruent with its absorption spectrum. The latter can be redshifted by vibrational state relaxation, which is called Stokes shift. But still the overlap of the LSc emission spectrum with parts of the absorption spectra of the LSc components allows the scintillator molecules to absorb photons. The energy can either be reemitted or converted into heat. In any case the original photon does not proceed its trajectory since reemission happens isotropically and delayed by another decay time [81, 82].

Rayleigh Scattering Rayleigh scattering of photons on molecules is an elastic process, i.e. the wavelength remains unchanged. The cross section for Rayleigh scattering in a liquid mainly obeys a λ^{-4} dependence [81]. The directionality of the process is anisotropic since the polarisation component parallel to the direction of incident light is fully suppressed for scattering angles $\theta = 90°$. This is reflected in the differential cross section for Rayleigh scattering

$$\left(\frac{\mathrm{d}\sigma}{\mathrm{d}\Omega}\right)_{\mathrm{ray}} \propto \frac{1+\cos^2\theta}{2}, \tag{2.14}$$

from which follows the scatter probability into forward and backward direction to be twice as high as orthogonal to the original flight direction. Inelastic scattering off molecules (Raman scattering) can be neglected due to much lower cross section [82].

Mie Scattering Mie scattering describes an elastic photon interaction with dirt or dust in the LSc. In contrast to Rayleigh scattering, the wavelength dependence is only weak. The directional distribution is complex and features an increased forward amplitude [82].

From the perspective of event reconstruction, the discussed attenuation effects lead to a loss of information since they disrupt the correlation between distance and time of flight. Furthermore, absorption without reemission results in a decreased light yield. For all processes, the reduction of intensity I in one dimension x can individually be described by an exponential law

$$I(x) = I_0 \mathrm{e}^{-\frac{x}{l}} \tag{2.15}$$

with the initial intensity I_0 and a characteristic propagation length l. Hence the propagation lengths l_{abs} for absorption, l_{are} for absorption plus reemission, l_{ray} for Rayleigh scattering, and l_{mie} for Mie scattering add up to the effective attenuation length l_{att}

according to

$$\frac{1}{l_{\text{att}}} = \frac{1}{l_{\text{abs}}} + \frac{1}{l_{\text{are}}} + \frac{1}{l_{\text{ray}}} + \frac{1}{l_{\text{mie}}}. \tag{2.16}$$

Unlike the individual lengths, l_{att} can be measured directly.

2.4 Light Detection

The emitted photons are detected by a system of light sensors. The detection principle is based on the conversion of optical photons into electrons via the photoelectric effect. A large set of parameters can be used to characterise the sensors, three of which are briefly discussed in the following due to their relevance for the LSc detector performance.

Photon Detection Efficiency Generally, a high number of photoelectrons favours the reconstruction of vertex and energy (see Section 4.4). Therefore, besides the optical coverage, also the photon detection efficiency (PDE) ε_{PDE} is a key parameter. The PDE denotes the number of detected photons N_{det} over incident photons N on a sensor, i.e.

$$\varepsilon_{\text{PDE}} = \frac{N_{\text{det}}}{N}. \tag{2.17}$$

Dark Count Rate Hits on a photo sensor that were not induced by external light are referred to as dark counts. A high dark count rate (DCR) impedes event reconstruction and can cause false triggers at very low energy thresholds. Different effects provoke dark counts, most relevantly thermionic emission of photo electrons and leakage currents between electrodes. Further contributions include cosmic ray interactions and radioactive decays within the sensor.

Transit Time Spread High precision in the determination of hit times is essential for a good vertex reconstruction. From the light sensor point of view the crucial point is the time variation in signal formation. The variation within one device, either defined as the full width at half maximum (FWHM) or as the standard deviation, is called transit time spread (TTS). Several effects contribute to the TTS: the conversion from photons to photo electrons, the multiplication process and the transport of the actual electric pulse. Given the dominant fast LSc time constant (see Section 2.2), a TTS in the order of a few nanoseconds is required to minimise the statistical impact on reconstruction.

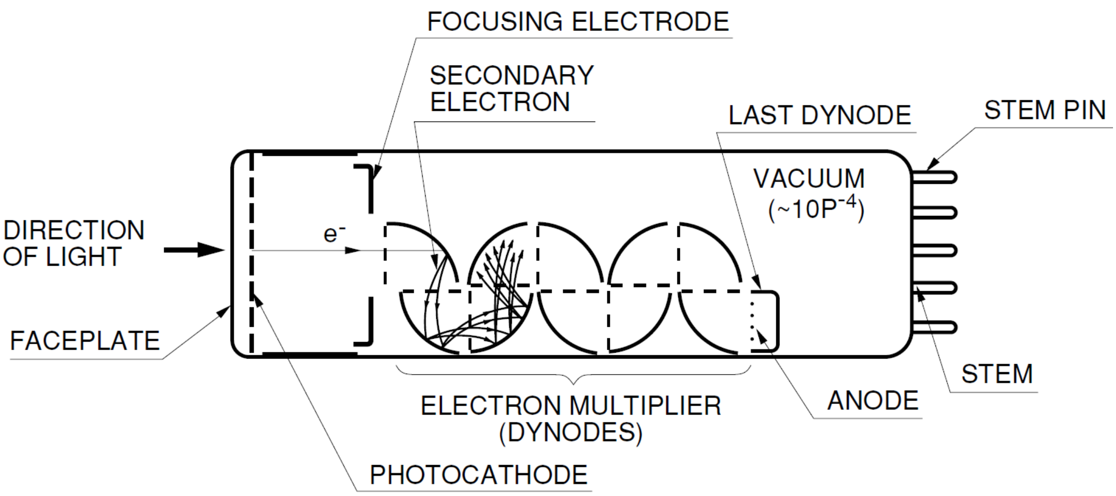

Figure 2.3: Structure and detection scheme of a dynode PMT. Taken from [83].

2.4.1 Photomultiplier Tubes

Photomultiplier tubes (PMTs) are the classical choice for light detection in large LSc and WC detectors, see [83] for a detailed technical overview. With diameters up to 20 inch, PMTs are the cheapest option for a large and very sensitive optical coverage.

An evacuated glass bulb houses the main components: A photocathode (PC), a multiplication structure, and an anode. Incoming photons can be absorbed by the PC on the inside of the glass window. Electrons in the PC layer are excited and emitted into the vacuum via the external photoelectric effect. The choice of window and PC material is responsible for the wavelength sensitivity of the PMT, e.g. bialkali coatings are suitable for the visible light spectrum.

The multiplication structure can take different forms. The dynode type is most common. The principle is schematically shown in Figure 2.3. A focusing electrode directs the photoelectron (PE) onto the first dynode, an electrode coated with a major secondary emissive material. Several secondary electrons are released, depending on the accelerating voltage. The multiplication process is repeated at the following dynodes which are held at increasing potential. The total voltage between PC and the collecting anode can be as high as several kV, providing a typical gain factor between 10^6 and 10^7 final secondary electrons per PE. The TTS can be as low as 3 ns FWHM for 20 inch PMTs and even shorter for small models.

An alternative to dynode multiplication is a multi channel plate (MCP), schematically illustrated in Figure 2.4. The plate with a thickness of a few mm is made of highly resistive material (e.g. lead-glass) and perforated with parallel capillaries, measuring $\sim 10\,\mu$m in

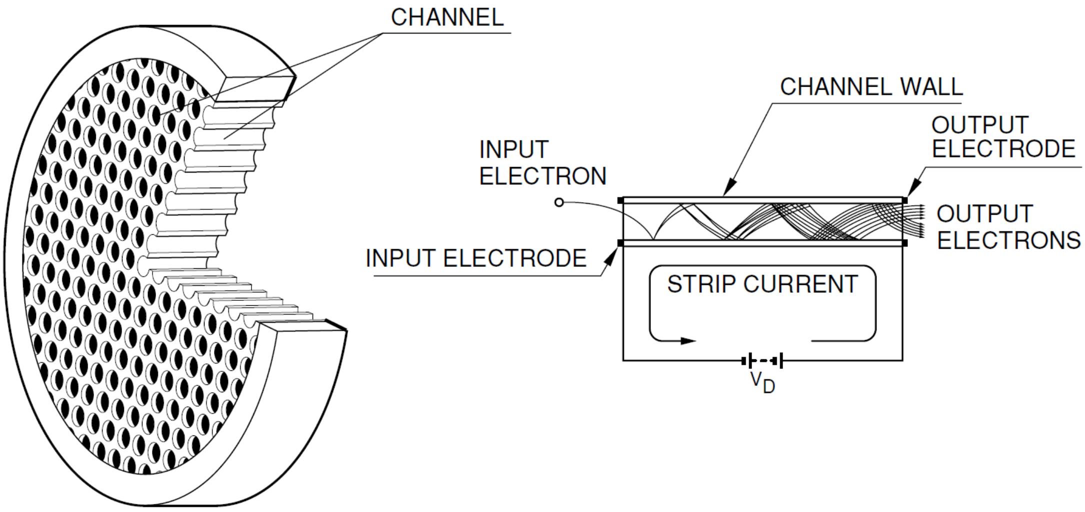

Figure 2.4: Left: Sketch of an MCP. Right: Scheme showing the multiplication process within one MCP channel. Taken from [83].

diameter and being slightly declined with respect to the plate surface. Impinging PEs trigger a cascade of secondary electrons when – accelerated by a strong electric field orthogonal to the plate – criss-crossing through the tunnel. The gain is similar to the dynode type. The TTS can reach excellent values below 100 ps. In large PMTs it is harder to equally focus the PEs from every spot of the PC onto the small MCP plate, thus introducing delays of more than 10 ns.

The number of generated primary PE divided by the number of incident photons is referred to as quantum efficiency $\varepsilon_{\mathrm{QE}}$ of the tube. The probability for a PE to be multiplied in order to finally provoke a signal is called collection efficiency $\varepsilon_{\mathrm{CE}}$. Hence, the PDE is given as the product

$$\varepsilon_{\mathrm{PDE}} = \varepsilon_{\mathrm{QE}} \cdot \varepsilon_{\mathrm{CE}}. \tag{2.18}$$

QE values usually lie between 15 % and 35 %. The CE can approach 100 % under optimal conditions and is diminished by an external magnetic field. In large PMTs even the weak Earth magnetic field negatively affects the long PE trajectories.

The PMT layout entails the eventual occurrence of spurious pulses. These are pre- and after-pulses. Pre-pulses occur when the incoming photon releases a PE at the focusing electrode or first dynode. This can result in a smaller gain and earlier anode pulse, thus altering the assigned charge and hit time. After-pulses can arise firstly when an electron scatters elastically on the first dynode before being amplified. This results in a signal delay up to some tens of nanoseconds. Secondly, electrons can ionise remaining gas atoms in the vacuum. The ions are attracted by the PC where they cause further PEs to be released. The resulting current signal at the anode follows some hundreds of nanoseconds after the original pulse.

2.4.2 Silicon Photomultipliers

Silicon photomultipliers (SiPMs) are an alternative to PMTs. They make use of the fact that absorbed photons can generate electron-hole pairs in semiconducting materials. A silicon p-n junction in a photodiode creates a depletion zone free of mobile charge carriers. When a reverse bias is applied, generated electrons and holes are accelerated towards the respective electrodes. A high electric field causes a charge carrier to generate an avalanche of secondary electron-hole pairs in the depletion zone, which can be measured as a macroscopic current. A component of this kind is called single photon avalanche diode (SPAD).

A silicon photomultiplier (SiPM) is a dense array of SPADs implemented on a silicon substrate. 10^2 to 10^3 SPAD can be operated per mm^2. Although the current within one SPAD is uncorrelated to the number of absorbed photons, the sheer number of SPAD units ensures a large dynamic range for photon counting.

The PDE of a SiPM depends on the photon wavelength and can exceed 50 %. The TTS of commercial models ranges from tens to some hundreds of ps. In that sense, SiPMs outperform PMTs. However, their small size complicates the instrumentation of large photosensitive areas which also increases costs. DCRs vary strongly with the temperature during operation. Depending on the application it might be necessary to cool down the setup to minus several tens of °C. More information on SiPMs can be found in [84, 85].

An example for an application in LSc detectors is the JUNO reference detector, which aims at full optical coverage with SiPMs in order to achieve an outstanding energy resolution of 1.5 % (see Chapter 3).

2.4.3 Large Array Picosecond Photo Diodes

With the development of large array picosecond photo diodes (LAPPDs) another device for light detection became commercially available lately. As the name suggests, a main ambition lies on the time resolution, with TTS values currently ranging around 100 ps FWHM. This is achieved by the assembly of two large ($\sim$ 20 cm $\times$ 20 cm) consecutive MCPs, closely followed by $\sim$ 30 parallel anode strips. The multiplied electrons are collected on several adjacent strips and the according currents are observed at both strip ends. A spatial resolution with millimetre precision is possible along the strip dimension by subtracting the pulse times on both ends, and in across-strip dimension by comparing amplitudes of adjacent strips. For further details, see [86].

LAPPDs are installed in ANNIE [87], a WC experiment to study neutrino-nucleus interactions. Also, there are plans for an application in the proposed THEIA project [88], a giant multipurpose experiment using water-based LSc technology.

2.4.4 Data Acquisition

The following paragraph outlines the basic steps in the data acquisition (DAQ) chain, rather than going into technical details.

The first step in the DAQ system is usually a discriminator, triggering only on signals with amplitudes above a defined threshold. From then on, the easiest method to handle pulses is to simply count their number and store the trigger times. This is sufficient for many applications, especially when only single hits are expected due to small sized sensors or low energy events. Otherwise, more sophisticated methods are at disposal. Ideally, the number of photon hits N is proportional to the charge deposited on the anode. Therefore, the analogously integrated pulse is a measure for N. Pile up effects for temporally close hits limit this method in precision, however.

The maximum information is preserved when storing the whole pulse shape. This can be realised with a fast analogue-to-digital converter (FADC). The device digitally stores the pulse amplitude samplewise. A reasonable compromise has to be found between the pulse length and sample rate on the one hand and the amount of data on the other hand. Single hit information like charge and time can be obtained from the pulse shapes in later analyses. Such information is highly valuable for a later event reconstruction. However, a full deconvolution of single hits is challenging, especially with increasing hit number.

The decision when and up to which stage to store data can be taken by a higher-level trigger system that takes into account e.g. the number and positions of fired sensors.

2.5 Perspectives

The use of LSc in large neutrino detectors is a well established technique and its full potential has not yet been exhausted. Concerning energy resolution, the targeted $3\,\%/\sqrt{E}$ of the JUNO experiment mark a new milestone. Related to this, the JUNO reference detector TAO [89], a ton-level LSc tank to measure the unoscillated reactor $\bar{\nu}_e$ spectrum, is designed with the goal to achieve energy resolution better than $2\,\%/\sqrt{E}$.

Compared to WC technology, a weak spot in LSc experiments is the lack of directional information. In principle, a separate treatment of scintillation and Cherenkov light could account for this. Different approaches for light separation in LSc have recently been carried out, making use of timing information [90], spatial light distribution [91], and spectral characteristics with the help of wavelength filters [79]. The sensitivity to the particle direction could give rise to particle identification and hence event discrimination. Corrections to the reconstructed energy could also be deduced.

In the future, higher precision of neutrino measurements need to be encountered by a significant enhancement of statistics. However, the dimension of LSc detectors is limited by the attenuation length l_{att}, meaning that light reduction along the photon path renders an extension of the tank radius beyond l_{att} unprofitable. Therefore, the combination of WC and LSc technology in so-called water-based liquid Scintillator is currently being tested and is foreseen to be used in THEIA [88] and WATCHMAN [92]. It is furthermore discussed as an option for ANNIE phase III [87]. The substance merges the advantages of WC, i.e. high transparency, high-precision timing, and directional information, with the high light yield and low threshold of LSc.

Chapter 3

The JUNO Experiment

The Jiangmen Underground Neutrino Observatory (JUNO) is a large LSc experiment currently built $\sim$ 650 m underground in Guangdong Province in the south of China. Located in a distance of about 53 km to the two nuclear power plants Yangjiang and Taishan it is designed as a medium baseline oscillation experiment for the determination of neutrino mass ordering (MO). In order to meet the requirements of high event statistics and an excellent energy resolution of $3\,\%/\sqrt{E}$, 20 kt of LSc are held by an acrylic sphere surrounded by $\sim$ 18,000 20 inch PMTs and additional 25,000 3 inch PMTs, adding up to a total optical coverage of nearly 80 %. The central detector is placed within a water pool, serving as buffer volume and, in combination with another 2,400 20 inch PMTs, also as a Cherenkov muon veto. High-precision muon tracking is achieved by installing scintillator tracking walls from the OPERA experiment [93] on top of the water pool. Measurement is foreseen to start in 2021.

Further design details are given in Section 3.1 with a focus on the central detector and its PMT systems. Section 3.2 provides an overview on the main physics goals. See [1] for further reading.

3.1 Design

The basic structure of JUNO is depicted in Figure 3.1. The heart of the experiment is its central detector (CD), an acrylic sphere with an inner radius of 17.7 m, filled with the 20 kt LSc through a chimney at the top. The acrylic has a thickness of 12 cm. The CD PMTs are mounted on the inside of a stainless steel latticed shell (SSLS) with an inner radius of 20.05 m and supported by scaffolding pillars – or rather held down due to the buoyancy of LSc within water. The surrounding cylindrical pool measures 43.5 m in diameter and 44 m in height and will be filled up to a level of 43.5 m with ultra pure water.

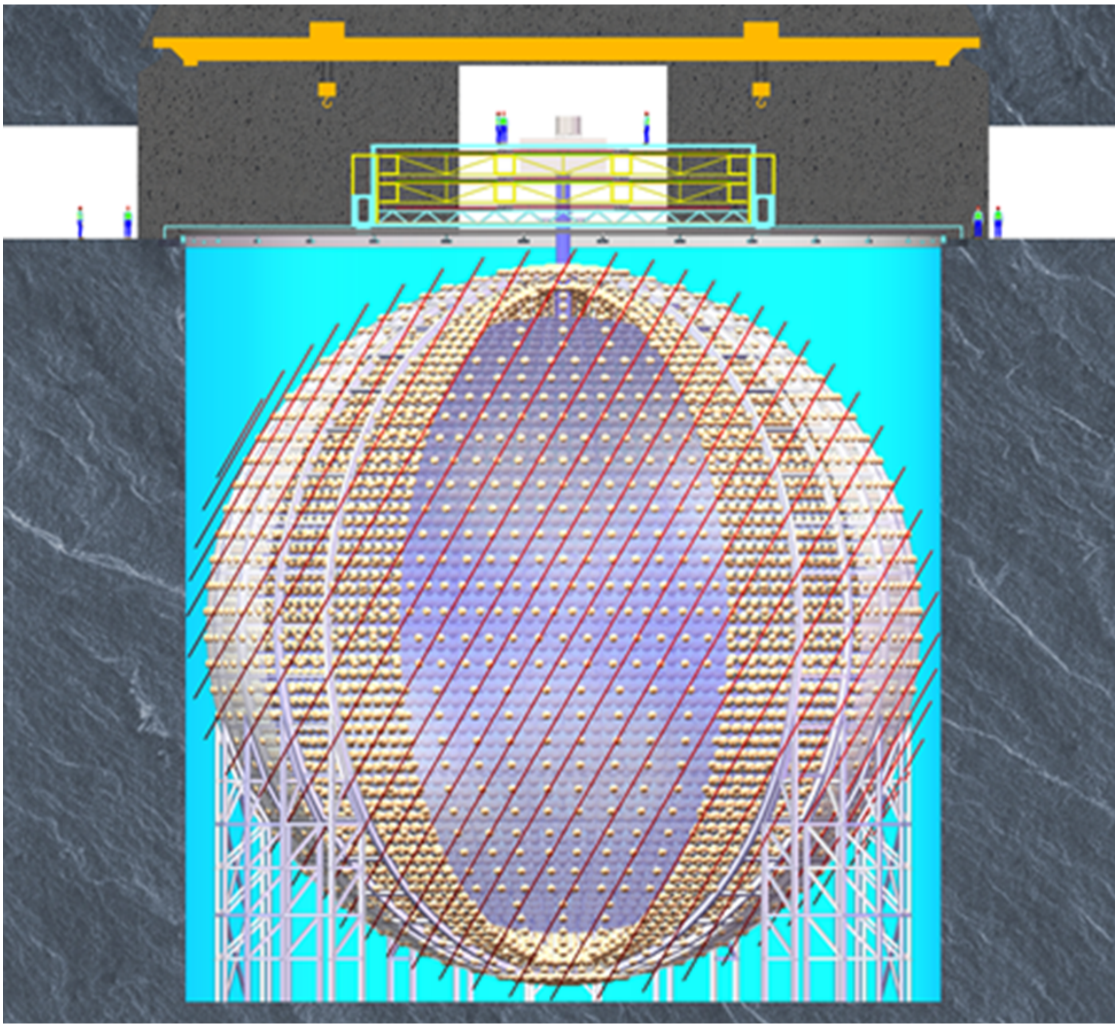

Figure 3.1: Visualisation of the JUNO experiment. The picture shows the spherical LSc tank which is surrounded by ultra pure water and supported by a stainless steel structure. Yellow bulbs represent the PMTs. Red lines mark the coils which wind around the inner detector in order to shield the Earth magnetic field. Provided by [80].

The veto PMTs will be installed on the outside of the SSLS sphere, facing outward. Coils, coloured in red in Figure 3.1, wind around the whole sphere in order to shield the PMTs from the Earth magnetic field. A large part of the CD is covered by the top tracker, building a three layered bridge over the water pool. Table 3.1 summarises the general parameters of the JUNO structure.

Table 3.1: Design parameters for the JUNO detector.

parameter	size [m]
acrylic sphere inner radius	17.70
acrylic sphere thickness	0.12
stainless steel latticed shell inner radius	20.05
water pool radius	21.75
water pool height	44.00

The following paragraphs highlight some selected aspects of the experiment design.

3.1.1 Liquid Scintillator

The JUNO design foresees LAB as LSc solvent combined with 2.5 g/l PPO as fluor and 3 mg/l bis-MSB as wavelengh shifter. Gadolinium doping is not added in favour of transparency which has to be exceptionally high with regard to the detector dimensions. This requirement is quantified by an attenuation length l_{att} not less than 20 m. l_{att} will be checked during the filling process and can be monitored at runtime.

The radioactive contamination from uranium and thorium must not exceed 10^{-15} g/g in order to keep the background low. This is ensured by the dedicated detector unit OSIRIS which will monitor the radioactivity in the LSc right before filling.

3.1.2 Large PMT System

The large PMT (LPMT) system subsumes $\sim 5,000$ units from the Japanese vendor Hamamatsu and $\sim 13,000$ units from the Chinese company Northern Night Vision Technology (NNVT). With absolute $\sim 75\,\%$, the LPMTs make up the major part of the optical coverage. A conceptional difference is the multiplier, being of dynode type in the Hamamatsu and of MCP type in the NNVT tubes. Mainly due to this, the TTS differs notably (see Section 2.4), being around 3 ns FWHM for Hamamatsu and 20 ns FWHM for NNVT. All PMTs are chosen such that the average PDE exceeds 27 % near the peak of the LSc emission spectrum, i.e. around a wavelength of 420 nm. This is ensured by an elaborate testing procedure, where the characteristic features of all PMTs are measured individually before installation. The main parameters for both PMT types are listed in

Table 3.2.

The 18, 000 tubes with their remarkably high PDE in the final setup will provide the CD with a photoelectron yield of $\sim 1,200$ photo electrons (PE) per MeV of deposited energy. The comparison of this number to e.g. ~ 500 PE/MeV in Borexino and ~ 250 PE/MeV in KamLAND stresses JUNO's exceptionally high ambitions with regard to energy resolution.

Groups of three LPMTs are connected to one shared underwater box which houses the electronics for high voltage (HV) control and signal readout. The readout features three independent ADC units converting the analogue signals into digital waveforms with a 1 GHz sampling rate. A local memory stores data until a global validation signal initiates the transmission to the DAQ above water via a CAT5 STP cable. The synchronous communication is ensured by another CAT5 STP cable to the back end electronic, providing a reference clock and the trigger signal.

Table 3.2: Key characteristics of the PMTs used in JUNO.

type	Hamamatsu R12860 HQE	NNVT model	HZC XP72B22
number	$\sim 5,000$	$\sim 13,000$	$\sim 25,000$
size	20 inch	20 inch	3.1 inch
multiplier	dynode	MCP	dynode
PDE@420 nm	24 % – 35 %	24 % – 35 %	22 % – 27 %
TTS (FWHM)	3 ns	20 ns	4.5 ns
DCR	< 50 kHz	< 100 kHz	< 1.8 kHz

3.1.3 Small PMT System

The gaps between the LPMTs will be filled up with 25, 000 3.1 inch PMTs of the model XP72B22 from HZC Photonics. Characteristic parameters can again be found in Table 3.2. Although the small PMTs (SPMTs) represent only 2 absolute per cent of optical coverage, their role is substantial. Due to the small size, 98 % of the SPMTs detect single PE pulses in the antineutrino reactor spectrum – in contrast to the LPMTs, where the number of received PE ranges among two orders of magnitude [94]. The photon counting SPMTs essentially help to calibrate the LPMT response, which is non-linear in event energy and non-uniform in event vertex. Thus, the double calorimetry system will enhance JUNO's energy resolution. Furthermore, as a stand-alone subdetector, SPMT will allow for independent physics studies e.g. in the solar, atmospheric, and supernova neutrino sector.

128 SPMTs are grouped for a joint HV supply and readout, both housed in an underwater electronics box. Unlike the LPMT system, not the digitised waveform but the

time and integrated charge of a PMT hit is sent to the DAQ above water via a CAT5 cable in a trigger-less stream.

3.1.4 Reference Detector

It was found that reactor antineutrino spectra are not smooth when resolved at the per cent level. Instead, a fine micro-structure is expected at the 50 keV to 100 keV scale [95]. This is due to Coulomb effects in the beta decays of neutron-rich fission products. The exact spectral fluctuations however are unknown and hard to be calculated. Since JUNO aims at the determination of mass ordering by measuring the deviation from the fine Δm^2_{31} oscillation, an unknown high frequency component in the Fourier transform of the measured spectrum would be a serious problem. In [89] it could be shown how a realistic fluctuation pattern would diminish JUNO's sensitivity to mass ordering.

To exclude misinterpretations of the JUNO IBD spectrum, a reference detector will measure the unoscillated antineutrino spectrum in a distance of $\sim 30\,\mathrm{m}$ to one core of the Taishan power plant. In contrast to typical near detectors in reactor antineutrino measurements, the Taishan Antineutrino Observatory (TAO) does not need to provide an online flux monitoring, but rather a single – but very precise – reference spectrum. The requirements for that purpose are quite high: 4500 photoelectrons per MeV have to be collected in order to achieve an energy resolution of 1.5 %. TAO is designed as a gadolinium-loaded LSc detector at the ton scale. A spherical vessel holds the LSc. The surrounding walls are covered to nearly 100 % with SiPMs with a quantum efficiency higher than 50 %. The setup has to be operated at -50°C in order to reduce dark noise to an an acceptable level. The start of measurement is planned for 2021.

3.2 Physics Goals

The JUNO design was optimised with regard to the determination of neutrino mass ordering (MO). However, its exceptional size and optical coverage mean good conditions for a bunch of complementary studies. Besides the main goal of MO, this section covers the precise measurement of the solar mixing parameters and the plans for solar, supernova, DSNB and geo neutrinos.

3.2.1 Mass Ordering

The question whether the normal or inverted neutrino mass ordering (NO and IO, respectively) is realised in nature is of fundamental interest in the neutrino community, as it was outlined in Section 1.3.1. Imaging the high frequent Δm^2_{31} oscillation requires both an energy resolution of $3\,\%/\sqrt{E}$, which is ensured by the high photoelectron yield, and an absolute energy scale uncertainty below $1\,\%$, which is achieved by the high degree of detector symmetry and extensive calibration efforts.

MO Measurement The signal channel for reactor antineutrinos in LSc is inverse beta decay (IBD), i.e. the decay of a proton into a positron and a neutron induced by an electron antineutrino according to

$$\bar{\nu}_e + p \to e^+ + n. \tag{3.1}$$

The small difference between Δm^2_{31} and Δm^2_{32} manifests itself in a beat frequency. Due to this, characteristic features for NO and IO would show up in Fourier transforms of the measured positron spectrum. The correct ordering is found by applying the least-squares method with the χ^2 definition [1]

$$\chi^2 = \sum_{i=1}^{N_{\text{bins}}} \frac{\left[M_i - T_i\left(1 + \sum_k \alpha_{ik}\epsilon_k\right)\right]^2}{M_i} + \sum_k \frac{\epsilon_k^2}{\sigma_k^2}, \tag{3.2}$$

where the spectrum is divided into N_{bins} energy bins. M_i and T_i are the measured and predicted number of events in the ith energy bin, respectively. The σ_k denote the systematic uncertainties with corresponding pull parameters ϵ_k that are associated to the ith bin via fractions α_{ik}. By minimising χ^2 for both the NO and the IO hypothesis, the MO can be obtained by comparing the resulting minima. The significance of the discriminator

$$\Delta\chi^2_{\text{MO}} = \left|\chi^2_{\text{min}}(\text{IO}) - \chi^2_{\text{min}}(\text{NO})\right| \tag{3.3}$$

is defined via an $n\sigma$ sensitivity on the MO with $n = \sqrt{\Delta\chi^2}$. On the basis of 100 k events, JUNO would have a discrimination power of $\Delta\chi^2_{\text{MO}} > 16$ under perfect conditions.

For an ideal MO measurement the detector baseline has to be optimised in such a way that the frequency shift in the Δm^2_{31} oscillation becomes most striking, which is around 53 km. At the same time, differences in distance between the detector and the individual reactor cores wash out the effect and diminish the MO sensitivity. Here, variations in the order of a few tens of metres have already strong impact. Additional reactors in the range of a few 100 km interfere with the measurement for a similar reason. At the JUNO site, the mentioned impacts reduce the optimum $\Delta\chi^2_{\text{MO}}$ by 5 [1].

It is expected that JUNO will collect the required 100 k events within six years of measurement.

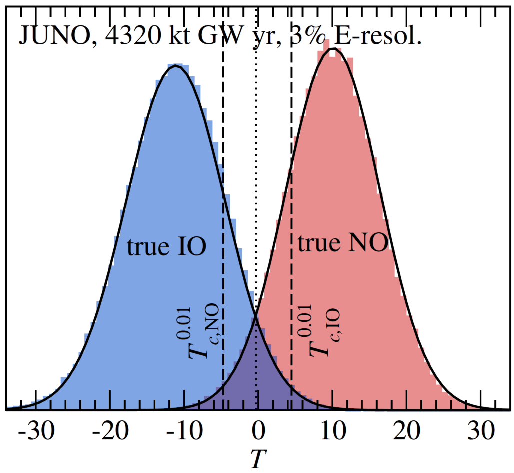

Figure 3.2: Distribution of a test statistic for a frequentist MO analysis. Taken from [96].

Statistical Interpretation The statistical interpretation of a MO measurement is not trivial and it might come in useful to look beyond the standard $\sqrt{\Delta\chi^2}\cdot\sigma$ representation. The binary problem of having two hypotheses H_{NO} and H_{IO} to choose from can be treated in a frequentist approach as elaborated on e.g. in [96]. In this framework, the sensitivity is determined via a test parameter T, which can – but not necessarily has to – be the difference between the two χ^2 minima:

$$T \equiv \chi^2_{\text{min}}(\text{IO}) - \chi^2_{\text{min}}(\text{NO}). \tag{3.4}$$

The probability density to measure a certain value for T in a given experimental setup follows a distribution that depends on the true hypothesis. The T distributions are obtained from Monte Carlo simulations. For JUNO, the result is two very similar, Gaussian curves around the respective expectation value T_0, shown in Figure 3.2. A critical threshold $T_{c,\text{NO}}$ needs to be defined, above which a T value measured by JUNO leads to an acceptance of H_{NO} (here and in the following, the IO case works analogously). Two major questions can be formulated with regard to the plot in Figure 3.2:

- Given that H_{NO} is true, what is the probability α for JUNO to still reject H_{NO}?

α is usually referred to as type-I error rate and determines the confidence level (CL) as $1-\alpha$. It is obtained by integrating the curve for true NO up to $T_{c,\text{NO}}$.

- Given that H_{IO} is true, what is the probability β to accept H_{NO} anyway?

This question is addressed by integrating the IO curve from $T_{c,\text{NO}}$ onwards, thus defining the type-II error rate β. With β one can express the so called power of the test, given as

$1-\beta$. The two related error rates are suited to discuss the significance of an experiment. As indicated in Figure 3.2, $T_{c,\mathrm{NO}}$ and $T_{c,\mathrm{IO}}$, here marking the positions for $\alpha = 0.01$, do not necessarily coincide. Depending on the chosen sensitivity, it can happen that an interval along T allows to simultaneously accept 0 or 2 hypotheses. For JUNO, the so called crossing sensitivity, where $T_{c,\mathrm{NO}}$ and $T_{c,\mathrm{IO}}$ are placed according to $\alpha = \beta$, is $1.9\,\sigma$. Another definition is the median sensitivity, characterised by the requirement that $\beta = 0.5$. The JUNO median sensitivity is stated to be $3.4\,\sigma$ and $3.5\,\sigma$ for NO and IO, respectively.

Backgrounds 89 IBD events are expected every day, accompanied by numerous events from various background sources. The characteristic signature of the prompt positron signal followed $\sim 200\,\mu$s later by the neutron capture is a very efficient handle for identification by requiring spatial correlation (vertex cut) and matching energies (energy cut). In combination with a reduction of the fiducial volume to a detector radius of 17 m, the accidental event pairs within the 1.0 ms trigger window (time cut), caused by coinciding background events due to radioactivity, cosmogenics, and neutrons, can be reduced to ~ 1 per day.

Cosmic muons hit the JUNO detector with a frequency of 3.5 Hz. In case that a hadronic shower occurs along the muon track, various cosmogenic isotopes are produced, among which ^{8}He and ^{9}Li are dangerous due to their ability to mimic IBD events. With branching ratios of 16 % and 51 %, respectively [97], ^{8}He and ^{9}Li undergo β^- decays under simultaneous emission of a neutron. With 84 events per day, the combined rate of ^{8}He and ^{9}Li is about the same as for IBD. Unlike accidental background, cosmogenic background cannot be rejected by a distance criterium. A detector dead time triggered by a muon veto is no option given the long half lives of 119 ms and 178 ms of ^{8}He and ^{9}Li, respectively [97]. Spatially confined vetoes around the reconstructed muon track are a realistic strategy, whereas the considerable loss of fiducial volume has a detrimental effect on the IBD efficiency. Table 3.3 lists the rates of IBD signal and all major backgrounds as well as the efficiencies and power of the event cuts. It can be seen how a 1.2 s cylindrical veto with 3 m radius around the muon track has the gravest effect on the IBD rate with only 83 % efficiency. Finally, 60 IBD events per day are expected to survive the cuts.

An unavoidable background is geo-$\bar{\nu}$s, since they, too, are being detected via IBD. However, with 1.5 events per day, their rate is small and they contribute only to the lower end of the reactor spectrum below 2.5 MeV.

Further background arises from fast neutrons which originate in the surrounding rock and can diffuse through the water pool into the detector. A neutron capture subsequent to the neutron bouncing off a proton can mimic IBD. 0.1 such events are expected to happen per day.

An even smaller contribution comes from $^{13}C(\alpha, n)^{16}O$ reactions, in which alpha particles from natural radioactivity are captured by ^{13}C under emission of a neutron. The prompt signal comes from the gamma de-excitation of the produced ^{16}O nucleus. 0.05 events per day are expected.

Table 3.3: Efficiencies $\varepsilon_{\mathrm{IBD}}$ of IBD selection cuts together with daily signal and background rates [1].

Selection	$\varepsilon_{\mathrm{IBD}}$	IBD	Geo-$\bar{\nu}$s	Accidental	$^{9}Li/^{8}He$	Fast n	(α, n)
—	—	83	1.5	$\sim 5.7 \times 10^4$	84	—	—
Fiducial volume	91.8 %	76	1.4		77	0.1	0.05
Energy cut	97.8 %			410			
Time cut	99.1 %	73	1.3		71		
Vertex cut	98.7 %			1.1			
Muon veto	83 %	60	1.1	0.9	1.6		
Combined	73 %	60	3.8				

Synergies with other Experiments In contrast to the detection of atmospheric and beamline neutrinos, JUNOs medium baseline approach does not utilise the MSW matter effect and is thus complementary. It is for this reason that synergies arise from a combined data treatment, as discussed in [98] and analysed closely in [99]. Both JUNO and a neutrino telescope like PINGU can fit their data to Δm^2_{31}, given as the location of the global minimum in the χ^2 distribution. When studying Asimov data sets, meaning that the observed quantities are in perfect accordance to their expected values, the minima should be 0 and coincide at the actual Δm^2_{31} value when the true MO is assumed. A simulated result is depicted in Figure 3.3 (a) for a runtime of 6 years both for JUNO (black curve) and PINGU (blue curve). Here, NO was assumed to be true. When the fit is done with respect to the wrong MO however, the tension between prediction and data causes non-vanishing minimum values and neither of the fits finds the correct Δm^2_{31}. Moreover, due to the complementary physical approaches, the minimum positions differ. The effect can be seen in Figure 3.3 (b). The widths of the minima, locally resembling parabolas, represent the fit precisions. The observation that especially the JUNO minimum is narrower than the distance between the two minimum positions is deciding for a combined fit of the two datasets. The contradicting preferred values for Δm^2_{31} force the combined fit (red curve) to form a much higher minimum. Two things need to be highlighted here. Firstly, the joined analysis shows less sensitivity to the single experiment performances, especially the strict energy resolution required in JUNO could be weakened to 6 % without losing much sensitivity in the combined approach. Secondly,

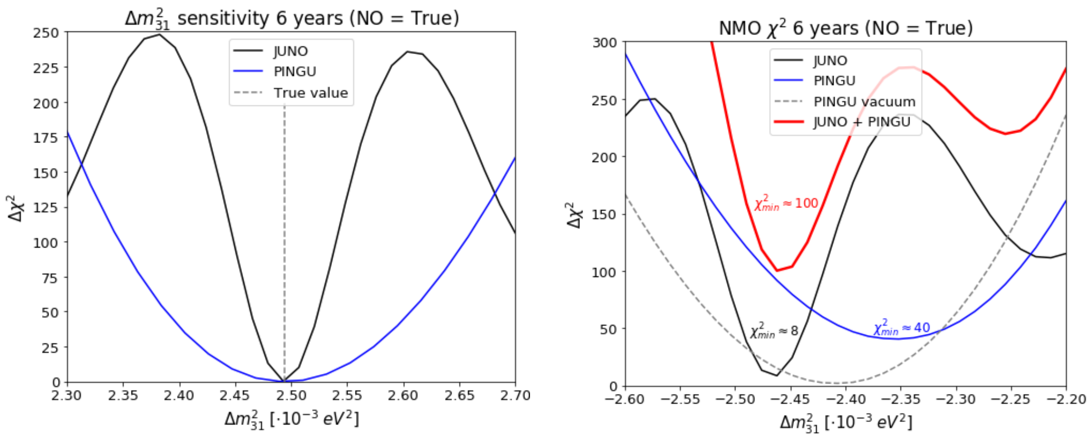

(a) (b)

Figure 3.3: Simulated results from $\Delta\chi^2$ fits to Δm^2_{31} under the condition of a true NO. For the correct MO hypothesis the fits of JUNO (black) and PINGU (blue) find a consistent minimum of 0. For the wrong hypothesis the minima are higher and distinctly located. A combined fit (red) reaches considerably higher significance than the single analyses. Taken from [99].

the combined analysis increases in significance over time, going beyond the statistical gain, since the individual Δm^2_{31} fits become more pronounced.

As it was discussed earlier in this section, the interpretation of significance has to be handled with care. Therefore, the joint approach is an important contribution to MO determination.

3.2.2 Oscillation Parameters

JUNO can do a precise measurement of the solar oscillation parameters θ_{12} and Δm^2_{21} due to its location directly in the first minimum of the solar neutrino oscillation and the excellent energy resolution. A good knowledge of mixing angles and mass splittings will help to further constrain the CP violating phase in long baseline experiments. Furthermore, high precision on the mixing parameters is critical for unitarity tests of the PMNS matrix. Deviations from unitarity would hint at the existence of sterile neutrino flavours.

Figure 3.4 shows the $\bar{\nu}_e$ L/E spectrum as expected in JUNO, depicted as a blue line for NO and a red line for IO. The small wiggles evoked by the Δm^2_{31} oscillation are imprinted on the much slower Δm^2_{21} oscillation, described by a continuous black line. A dashed black line shows the expectation for the non-oscillation hypothesis, the shape being identical to the convolution of reactor spectrum and energy dependent cross section.

In a two-flavour scenario, θ_{12} would manifest itself in the difference between the

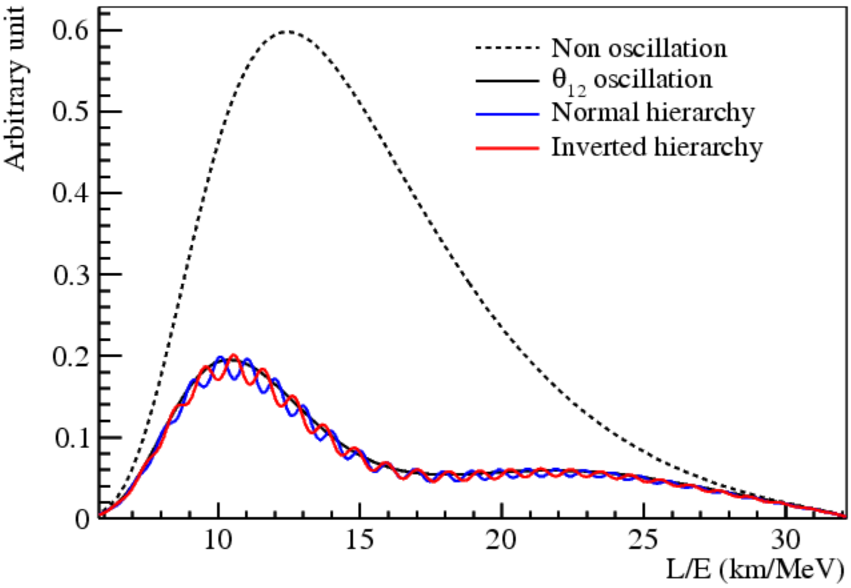

Figure 3.4: L/E spectrum as expected at the JUNO site. The dashed line describes the spectrum given a non oscillation hypothesis. The solid black line represents the θ_{12} oscillation. The additional wiggles in the full three flavour picture are depicted as blue and red lines for NO and IO, respectively. Taken from [1].

two black lines, most prominently in the ratio near the shallow dip around 16 km/MeV whereas its position is determined by Δm^2_{21}. The dip is more pronounced in the depiction in Figure 1.10. The high energy resolution in JUNO allows for an accurate data fit in a three-flavour picture. Both solar mixing parameters can be constrained with a precision below 1 %. This is a big step forward regarding the current precisions listed in Table 3.4. For Δm^2_{21} the leading experiment KamLAND quotes 2.7 % precision, with no further constraint in global analyses. $\sin^2\theta_{12}$ was dominantly measured by SNO with 6.7 % precision, while global fits achieve 4.2 %.

Table 3.4: Current precision on solar mixing parameters. The values from the dominant single experiment are listed as well as global fit best values.

	Δm^2_{21}	$\sin^2\theta_{12}$
Experiment	KamLAND	SNO
Individual 1σ	2.7 % [25]	6.7 % [18]
Global 1σ	2.8 % [12]	4.2 % [12]

3.2.3 Solar Neutrinos

Motivation Solar neutrinos can, as they are direct messengers from the core of the sun, very effectively probe solar models. This holds in particular for the solar metallicity problem, describing the discrepancy between measurements and standard solar models for the elemental composition of the star. Apart from neutrino measurements, solar abundances can be estimated from various observations: helioseismology, photosphere spectroscopy, solar wind measurements, and the examination of selected meteorites that are believed to have preserved big parts of the original solar nebula abundances. The measured values find entry into solar models, where the heavy element fraction, namely the abundances of iron, sulfur, silicon, and oxygen, strongly affect the star opacity and thus the core temperature, in turn being correlated to the neutrino production. Furthermore, the fractions of carbon, nitrogen, and oxygen provide insight into the processes of heat generation and thus the solar structure.

With X and Z describing the mass fractions of hydrogen and elements heavier than helium, Z/X is often used to compare metallicity models. Helioseismology, which is the study of solar oscillations as a result of acoustic waves, is strongly connected to the solar model, as the abundances in different layers determine the speed of sound. It prefers a significantly higher fraction of heavy elements than spectroscopy and meteoritic studies [100]. The low-Z models are backed up by new solar wind measurements [101]. A detailed physical overview is provided by [102].

As will be pointed out later on, JUNO can contribute to the solution of the solar metallicity problem. Furthermore, the experiment can probe a decisive prediction of the neutrino oscillation framework by measuring the upturn region in the MSW paradigm: As it was discussed in Section 1.2.1, the huge amount of matter crossed by solar neutrinos leaving the sun results in a reduced ν_e survival probability P_{ee} measured on Earth, on condition that their energy is high enough to fulfil the MSW resonance criterium given by Equation (1.17). The transition from low P_{ee} at high energies to higher P_{ee} at low energies is expected to lie between 2 MeV and 5 MeV, as can be seen in Figure 1.3. The plot also demonstrates that the region is experimentally unexplored, except for a hint on the upturn from the combined analysis of all four Super-Kamiokande (SK) phases [17].

JUNO's potential with regard to solar neutrino studies lies in its exposure (the LSc mass holding almost 80 times Borexino) and the LSc technology (greatly deceeding the analysis threshold of WC experiments, e.g. 3.5 MeV in SK) paired with the unprecedented high energy resolution. However, drawbacks are the low overburden, leading to a considerable contamination with cosmogenic isotopes, and the lack of directional information, making an event-by-event identification very hard.

Signals and Backgrounds The dominant signal channel for the solar neutrinos is elastic scattering off electrons according to

$$\nu_{e,\mu,\tau} + e^- \rightarrow \nu_{e,\mu,\tau} + e^-. \tag{3.5}$$

This implies that the measured spectra resulting from the solar neutrino spectra depicted in Figure 1.1 are continuous even for discrete neutrino energies. Elastic scattering is open to all flavours, although the cross section σ is higher for the electron than for other flavours with $\sigma(\nu_{\mu,\tau}e) \approx 0.16\,\sigma(\nu_e e)$ [5]. Other than for IBD not coincidences but single signals are measured, which is throwing the gates wide open for numerous background sources, most importantly beta and gamma decays. These can come from internal contamination of the LSc and the surrounding material, and from cosmogenic isotopes. The cosmogenics originate from the spallation of ^{12}C nuclei induced by traversing cosmic muons. Table 3.5 lists the radiopurity requirements for solar neutrino measurements in JUNO as well as the expected rates for solar neutrinos and the cosmogenic isotopes ^{10}C, ^{11}C, and ^{11}Be.

Table 3.5: Radiopurity requirements for low energy solar neutrino measurements, and expected rates for solar neutrinos and cosmogenic backgrounds in JUNO. Values taken from [1].

Internal radiopurity requirements	
^{210}Pb	5×10^{-24} g/g
^{85}Kr	500 counts/day/kton
^{238}U	1×10^{-16} g/g
^{232}Th	1×10^{-16} g/g
^{40}K	1×10^{-17} g/g
^{14}C	1×10^{-17} g/g

Cosmogenic background rates (counts/day/kton)	
^{11}C	1860
^{10}C	35
^{11}Be	2

Solar neutrino signal rates (counts/day/kton)	
pp ν	1378
^{7}Be ν	517
pep ν	28
^{8}B ν	4.5
^{13}N/^{15}O/^{17}F ν	7.5/5.4/0.1

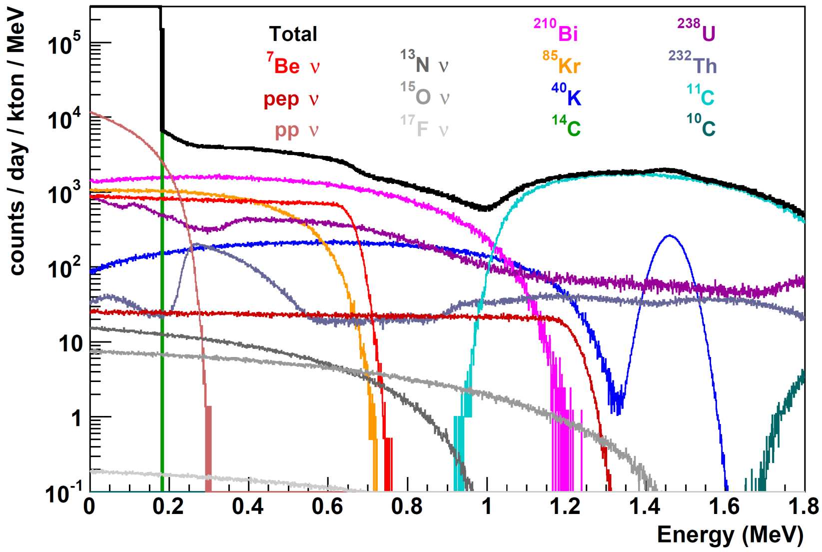

Figure 3.5: Expected signal and background spectra for solar neutrino measurements with JUNO. All rates are in accordance with Table 3.5. Taken from [1].

Figure 3.5 shows the expected spectra that would emerge from the contributions listed in Table 3.5 at energies below 1.8 MeV. It was assumed that external radiation can be removed by fiducial volume cuts, i.e. only intrinsic LSc contamination is displayed. Furthermore, alpha events from the ^{232}Th and ^{238}U chain are neglected, since alpha signals are expected to be removable with pulse shape discrimination.

Along the black line describing the total event rate the ^{7}Be ν signal evokes a recognisable feature in the shape of the characteristic shoulder which is also being observed at Borexino. With the quoted backgrounds, the signal to noise ratio would be around $S/N \approx 1/3$, comparable to the KamLAND solar phase. Reducing the ^{85}Kr and ^{210}Pb contaminations by a factor 5, comparable to Borexino phase-I, would raise S/N to 1/2.

Depending on the efficiency in identifying pile-up events and the corresponding ability to clearly resolve the steep falling edge of the ^{14}C spectrum JUNO can possibly provide a high rate measurement of *pp* ν between the ^{14}C and the ^{210}Bi dominated energy region around 0.2 MeV.

Although the ^{8}B ν rate is too low to be displayed in Figure 3.5, the according spectrum stretches to energies far beyond 2.6 MeV, where no natural gamma background is present. Neutron capture in the surrounding stainless steel produces 6 MeV and 8.5 MeV gammas, which need to be avoided by confining the fiducial volume to the inner detector region, at least a couple of metres deep. It has to be noted that the intrinsic ^{232}Th contamination has to be reduced to 10^{-17} g/g in order to allow a ^{8}B ν measurement below 5 MeV.

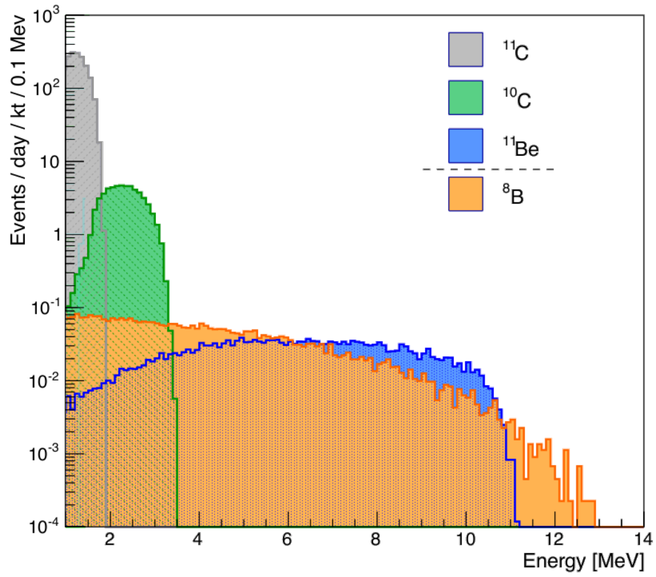

Figure 3.6: Expected signal and cosmogenic background spectra for ^{8}B ν measurements with JUNO. All rates are in accordance with Table 3.5. Taken from [1].

Under these conditions the dominant background for a ^{8}B ν measurement comes from the cosmogenic isotopes with the spectra plotted in Figure 3.6. From the threshold energy of ~ 1 MeV onwards, the β^+ emitters ^{10}C and ^{11}C dominate the total spectrum almost until their Q values at 3.7 MeV and 2.0 MeV, respectively. At the high end of the energy spectrum, the β^- emitter ^{11}Be is dominant.

Analyses JUNO's large exposure and low energy threshold make it possible to explore the MSW transition region with a ^{8}B ν measurement around 3 MeV. The cosmogenic background leaves a small energy window between $\sim$ 3.5 MeV and $\sim$ 5 MeV. The extension to lower energies depends in particular on the reduction of ^{10}C background. In principle, an identification of ^{10}C and ^{11}C can be done on the basis of an e^+/e^- event discrimination. So far, both particles were considered as indistinguishable in LSc detectors. As subject of this thesis, it is demonstrated in Chapter 6 how a distinction can be made based on different topologies in the energy depositions.

As for the solar metallicity problem, JUNO can provide insightful analyses even though a direct measurement of the CNO neutrino fluxes is less realistic. The left plot in Figure 3.7 shows the 1σ allowed regions in the ^{7}Be and ^{8}B ν flux plane for three different solar models: The black ellipse for the SFII-GS98 high-Z model compared to the SFII-AGSS09met low-Z model and the SFII-AGSS09 κ low-Z model that assumes an increased opacity. The Borexino measurement [20], represented by a black marker,

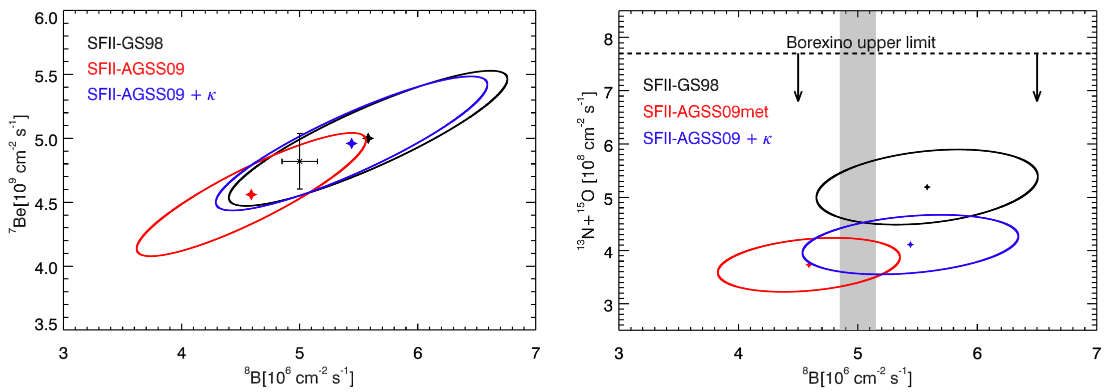

Figure 3.7: Left: Comparison of experimental results and expectations for flux measurements of $^{7}\mathrm{Be}\,\nu$ and $^{8}\mathrm{B}\,\nu$. The black marker with error bars depicts the Borexino measurement. The ellipses represent $1\,\sigma$ allowed regions derived from different solar models. Right: Comparison of experimental results and expectations for flux measurements of $^{13}\mathrm{N} + {}^{15}\mathrm{O}\,\nu$ and $^{8}\mathrm{B}\,\nu$. The dashed line marks the upper limit from Borexino. The grey shaded region represents the $1\,\sigma$ region from $^{8}\mathrm{B}\,\nu$ measurements. Taken from [1].

does – with the current precision – not favour any of the models. A slight tendency could be gained by an increase in accuracy from the JUNO measurement.

The ambiguity can also be approached by comparing a precise $^{8}\mathrm{B}\,\nu$ measurement to an improved upper limit on the combined fluxes of $^{13}\mathrm{N}$ and $^{15}\mathrm{O}\,\nu$, as can be seen in the right plot of Figure 3.7. However, the information on the CNO flux must come from future external data, e.g. from Borexino or SNO+. The current Borexino limit is indicated by the dashed line. It can be seen how the limit reduction has the potential to disfavour the high-Z model, while a precise knowledge on the $^{8}\mathrm{B}\,\nu$ flux can shed more light on the role of opacity in the models.

3.2.4 Supernova Neutrinos

Neutrinos play a substantial role in the established models describing a core collapse supernova (SN), which includes all SN types except for the thermonuclear type Ia. The impressing energy amount of roughly 3×10^{53} erg is released in such an event – about 99 % of which in the form of neutrinos. In the following, the development of the process will be summarised in a very brief way, referring to [103] for an extensive review.

Neutrino production in SN After completing the burning stages up to iron, the core of a star heavier than 11 solar masses $M_\odot$ stops the burning process, leading to the discontinuation of outward directed radiation pressure. Above the Chandrasekhar limit of a core mass of $1.44\,M_\odot$ the remaining degeneracy pressure does not suffice to compensate the gravitational pressure and the core finally collapses. The neutronisation

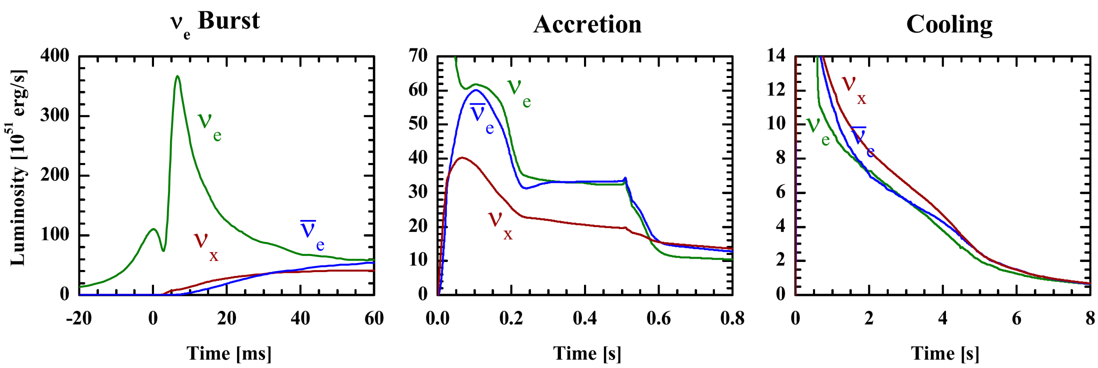

Figure 3.8: Development of neutrino luminosities from a core-collapse SN as expected from a simulation. The three panels show the phases of ν_e burst, accretion, and cooling, respectively. ν_x denotes the added luminosities of heavy flavour neutrinos. Taken from [1].

process $e^- + p \to n + \nu_e$ provides a ν_e flux, but only until the core reaches a density of $10^{12}\,\mathrm{g\,cm^{-3}}$, above which neutrinos are effectively trapped inside the inner core due to the short interaction length of only a few metres at the given energies and density. As soon as the core reaches nuclear matter density ($10^{14}\,\mathrm{g\,cm^{-3}}$), the collapse undergoes a bounce effect, resulting in an outward directed shock wave. The propagating wave encounters the supersonically infalling high-Z matter which implicates deceleration and dissociation of nuclei into free nucleons and α particles on the one hand, and a damping of the shock wave on the other hand. When the shock passes the less dense outer layers of the iron core – called neutrinosphere, since neutrinos can again escape the interaction trap from here on – neutronisation of produced free protons causes the emission of a sudden ν_e burst for a few milliseconds.

Meanwhile, the proto neutron star core continues the accretion of matter, gaining $\sim 0.1\,M_\odot$ per second. During the accretion phase, various neutrino interactions take place in the core. Besides the scattering of neutrinos on nuclei, nucleons, charged leptons, and even neutrinos, this includes neutrino production and absorption in beta processes, creating about 10 % of the core neutrinos, and pair production and annihilation in thermal processes, responsible for the remaining 90 %. The latter channels also create the heavy flavour neutrinos ν_μ, $\bar{\nu}_\mu$, ν_τ, and $\bar{\nu}_\tau$, but almost exclusively in the deeper and therefore hotter regions of the core. Hence they undergo numerous processes until reaching the neutrinosphere.

Neutrino emission has a cooling effect on the proto neutron star. Vice versa, the absorption of neutrinos heats up the matter, also in the less dense outer layers following the neutrinosphere. It is this fact that revives the stalled shock wave and ignites the actual explosion.

Figure 3.8 shows the luminosities for the different phases ν_e burst, accretion, and cooling as a function of time. In the first panel, the prominent peak from the prompt ν_e burst is clearly visible subsequent to an interruption of the increase due to the core becoming opaque to neutrinos at high density. During accretion, mostly ν_e and $\bar{\nu}_e$ leave the neutrinosphere. The cooling phase, depicted in the third panel, stretches to 8 seconds after the collapse.

The average flavour energies range from 10 MeV to 18 MeV, depending much on the phase and region of creation, i.e. on the questions if, when, and where they were thermalised in scattering processes.

SN signals in JUNO Only a few SN explosions per century are expected to take place in our galaxy, making their survey a very rare and highly anticipated event. The only ever measured SN neutrinos from SN 1987A give a spectacular but statistically rather poor insight into the internal SN processes with only a few handfuls of total events detected by the Kamiokande detector [104]. The observation of galactic SN neutrinos serves two major interests: Firstly, it would trigger a worldwide early warning towards the optical telescope community, since SN neutrinos arrive hours before the visible light. Secondly, the model described above can be probed by a high rate, flavour-sensitive measurement. This holds especially for the aspect of the neutrino-driven explosion mechanism.

Taking the expected average distance of 10 kpc as a baseline, JUNO expects event numbers in a similar order of magnitude as SK. JUNO can detect SN neutrinos in different reaction channels, most importantly IBD with about $5,000$ $\bar{\nu}_e$ events. Elastic neutrino-proton scattering is open to all flavours and is expected to generate up to $2,000$ signals. Further 300 ν_e events can be measured due to neutrino-electron scattering, making JUNO the most promising detector for SN ν_e. The charged current interactions of $\nu_e + {}^{12}\mathrm{C} \rightarrow e^- + {}^{12}\mathrm{N}$ and $\bar{\nu}_e + {}^{12}\mathrm{C} \rightarrow e^+ + {}^{12}\mathrm{B}$ feature beta emitters in their final states, allowing for delayed coincidence identifications. However, the respective high energy thresholds of 17 MeV and 14 MeV lead to expected total event numbers around 100, depending strongly on the average neutrino energy. JUNO's readout electronics are designed to cope with the large event rates expected for a SN at 10 kpc.

Although LSc experiments are very limited in reconstructing directionality for single events, the vast amount of IBD events can make it possible to reconstruct the direction of a SN to a certain degree by analysing the displacement of neutron positions with respect to positron vertices. It was demonstrated with a Monte Carlo study in [105] that a Gd-loaded LSc detector can determine the direction with an uncertainty below 10°on the basis of 5000 IBD events.

3.2.5 DSNB

While galactic SN are very rare events, the combination of all past core-collapse SN in the visible universe is expected to provide a constant neutrino flux, known as diffuse supernova neutrino background (DSNB). This flux consists in equal parts of all neutrino and antineutrino flavours. Assumed to be in the order of $100\,\mathrm{cm}^{-2}\mathrm{s}^{-1}$, the DSNB flux could not yet be measured. Its detection, or even an exclusion down to an upper limit, would have implications for our knowledge on the star formation rate, the average core-collapse SN spectrum, and the rate of failed SN. See [106] for more details.

JUNO can detect the $\bar{\nu}_e$ component via IBD. For obvious reasons, the main background at low energies up to 11 MeV comes from reactor neutrinos. An unavoidable background at high energies arises from the atmospheric $\bar{\nu}_e$, which dominate over the DSNB signal with an assumed average energy of 15 MeV above 30 MeV. Throughout the energy region in between, the remaining background sources are fast neutrons, which can mimic IBD by prompt proton recoil and delayed capture, and atmospheric neutrinos, which can generate IBD-like signals e.g. by neutron knock-out. Based on studies for the LENA project [107], pulse shape discrimination is expected to reduce both backgrounds to acceptable levels, so that up to a few tens of DSNB signals could be detected within 10 years of measurement, depending on the actual average energy.

DSNB will also be surveyed by SK, whose target contains about as many protons as JUNO. An upgrade with gadolinium added to the water for a more efficient neutron tagging is about to start measurement and, as a WC detector, will provide a valuable complementary DSNB measurement.

3.2.6 Geo-Neutrinos

The Earth is a continuous source of antineutrinos. The β^- decays from the natural ^{238}U and ^{232}Th chains and ^{40}K constitute a flux of a few $10^6\,\mathrm{cm}^{-2}\mathrm{s}^{-1}$ which could be observed by Borexino [108] and KamLAND [109]. As direct messengers from the inside of the Earth, geo-neutrinos are expected to give answers to geological questions, e.g. how much of the heat flow on the Earth's surface is due to the radioactive, heat producing elements, and how much contribution comes from accretion and core segregation, often referred to as primordial sources. The few handfuls of measured geo-neutrinos do not allow for precise abundance determinations, though. The much bigger JUNO detector is expected to collect ~ 400 geo-neutrino events per year [110] and can therefore drive forward the field substantially.

The visible energies in the detector lie below 3 MeV. Since geo-neutrinos share the IBD channel with the dominating reactor neutrinos, only a statistical treatment is possible by subtracting the reactor spectrum.

A challenge in the geological interpretation will be the composition and thickness of the crust as a local function, which makes the expected strong contribution from the crust hard to disentangle from the layers below. A further discussion of the potential of geo-neutrino measurements at JUNO can be found in [110].

Chapter 4

JUNO `offline` Software

JUNO `offline` is a software package serving different purposes: It contains tools for the production of Monte Carlo (MC) data, for the calibration of simulated and experimental raw data, and for data analysis such as reconstruction of vertex and energy. It is written in `C++` and features a `Python` user interface. `offline` [111] is based on the `SNiPER` framework [112] and uses `ROOT` [113] to write persistent data.

The production of MC data involves four separate stages, illustrated by Figure 4.1. The data can be retrieved after each step in a `.root` format. In the first step, the `Geant4` based [114] *detector simulation*, JUNO events are generated and their kinematics are simulated up to the point of optical photons triggering the sensitive sensors, i.e. PMT and top tracker hits. On the next level, the response of PMTs and readout electronics is mimicked in the *electronics simulation*. From here on, the treatment of simulated equals the experimental data processing: The resulting waveforms are transferred back into hit times and respective charge depositions in the *calibration* step, followed by the final *reconstruction* which performs dedicated algorithms to reconstruct e.g. event vertex and deposited energy.

In order to allow a profound interpretation of the simulated data analysed in Chapter 6, this chapter reviews the different workflow stages, i.e. detector simulation in Section 4.1, electronics simulation in Section 4.2, calibration in Section 4.3, and reconstruction in Section 4.4.

4.1 Detector Simulation

The first simulation step is the generation of events. This can be done either with a virtual particle gun which shoots particles of a chosen type from a certain point with defined momenta into the detector, or by choosing from a list of pre-implemented tools

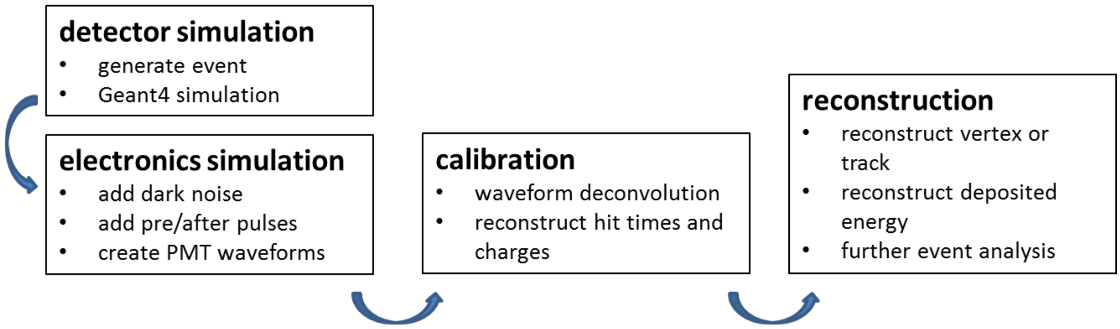

Figure 4.1: Illustration of the workflow in JUNO `offline`. The result of each step is stored in a `.root` file.

that emulate e.g. IBD or certain radioactive decays. Alternatively, an external program can be executed in order to generate the required parameters, which can hence be loaded into the simulation.

The detector geometry is implemented with respect to the dimensions quoted in Table 3.1.

The actual simulation of kinematics and physical processes follows the standard `Geant4` workflow. Optical light is produced by scintillation and Cherenkov radiation, the former using the weights and time constants given by Table 4.1 and explained in Section 2.2.1. Regarding the light propagation, Rayleigh scattering, photon absorption and subsequent re-emission, and optical refraction are considered.

Table 4.1: LSc time constants and weights as implemented in JUNO `offline`.

time constant τ [ns]	weight ω [%]
4.93	79.9
20.6	20.1

A full optical model is implemented, i.e. all optical parameters are treated energy dependent. Figures 4.2 (a) - (h) show several parameters as a function of wavelength as implemented in `offline`.

4.2 Electronics Simulation

In the following step, the hit information of the LPMTs is transformed into pulses. For the SPMT system no pulse shapes are written.

It is possible to mix events from different input files. The input hit times are smeared with regard to the individual channel TTS. Channel dependent time offsets are added to the hit times, reflecting the signal propagation through cables and electronic components.

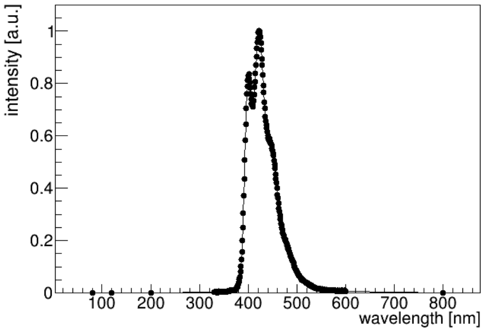

(a) Emission spectrum in LSc.

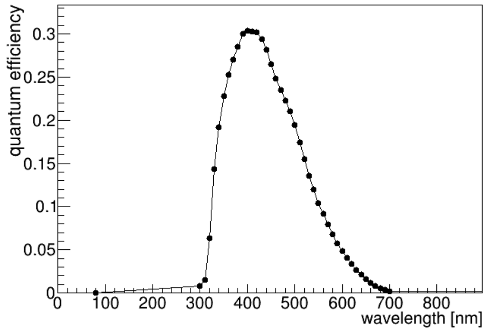

(b) LPMT quantum efficiency.

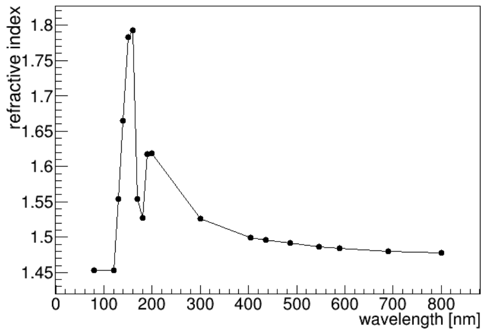

(c) Refractive index in LSc.

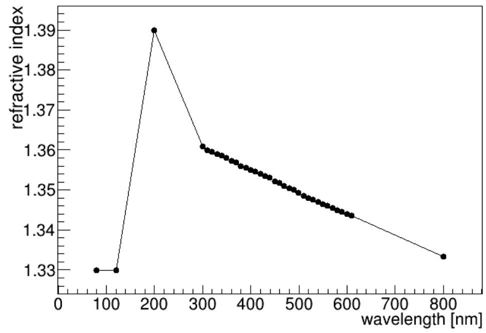

(d) Refractive index in water.

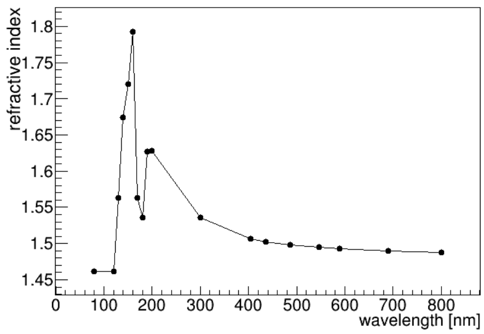

(e) Refractive index in acrylic

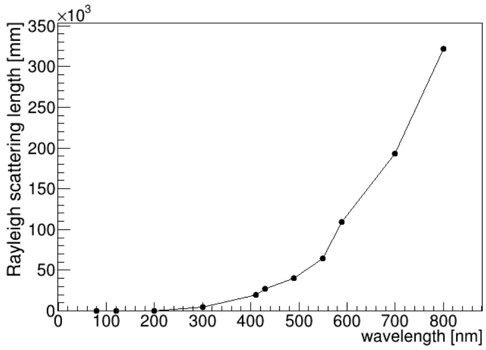

(f) Rayleigh scattering length in LSc.

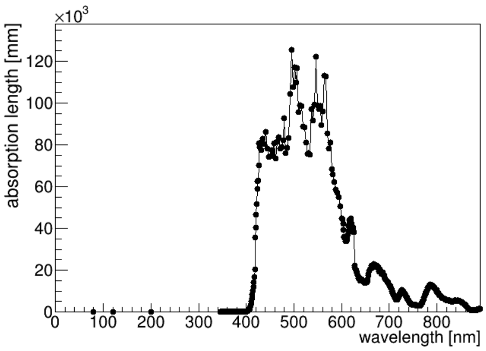

(g) Absorption length in LSc.

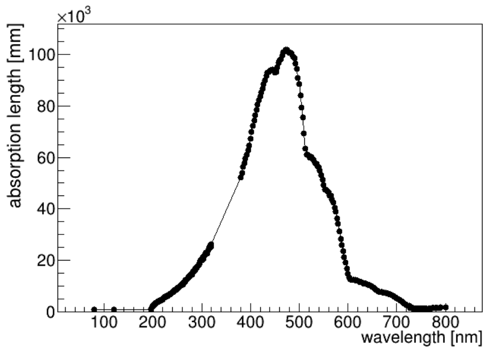

(h) Absorption length in water.

Figure 4.2: Optical parameters as a function of wavelength as they are implemented in `offline`. Data provided by [80].

Pre- and afterpulse hits are added to the physical photon hits, as well as dark noise with a frequency of 20 kHz. Charges are assigned to all hits. Then the signal shape is being built by superimposing log-normal functions which are scaled with regard to the respective charges. Further function parameters were obtained from PMT measurements. White noise is also added on top of the waveforms.

The pulses are sampled with a rate of 1 GHz in a 1250 ns signal window with regard to the actual LPMT DAQ.

4.3 Calibration

The calibration step aims at the recovery of the relevant signal information, which is the number of photoelectrons n_{PE} and their hit times t_i.

In an ideal system the t_i could be gained by performing a simple peak searching algorithm. n_{PE} could be obtained either from counting the peaks or integrating over the signal. In realistic setups, various features render these approaches less suitable. This can be overshoots, meaning that the pulse shortly dips under the baseline level after the main peak, additional peaks due to internal electronic reflections, or simply electronic noise. Furthermore, close-by hits can appear as single peaks, making the reconstruction of t_i and n_{PE} more complicated.

Pulse deconvolution is of help here. The idea is to transform the signal into the frequency domain, apply appropriate filters and re-transform the result into the time domain. Details can be found e.g. in [115]. In a first step, the white noise can very efficiently be reduced by using a Gauss filter on both the real and the imaginary components of the frequency spectrum. The actual deconvolution from the signal shape requires a good knowledge of the typical single PE shape, which is used as a template in order to create a filter. After transforming back into the time domain, the deconvolved signal can much better be treated with integration and peak searching algorithms.

4.4 Reconstruction

The last step in the chain deals with the reconstruction of the physical event inside the JUNO central detector. Besides the amount of deposited energy this includes the event location, called vertex for low energy (LE) events that are considered as point-like, and track for high energy (HE) muons. The standard procedure for muon reconstruction is explained in [116] and will not be discussed here.

The default algorithm for LE vertex reconstruction is a log-likelihood method described in [117]. The idea is to maximise the likelihood function

$$\mathcal{L} = \prod_i f_{\mathrm{res}}(t_{i,\mathrm{res}}), \tag{4.1}$$

where $f_{\mathrm{res}}(t_{i,\mathrm{res}})$ is the value of a probability density function (pdf) at the residual time $t_{i,\mathrm{res}}$ assigned to the ith PMT hit. The latter function is defined as the difference between hit time t_i and estimated time of flight (tof) at a given position $\vec{r}$ in the detector with respect to a reference time t_0 according to

$$t_{i,\mathrm{res}} = t_i - \mathrm{tof}_i - t_0. \tag{4.2}$$

$\mathcal{L}$ is calculated for nodes on a grid which is centred around the best guess $\vec{r}_0$ for the vertex. The origin of the coordinate system coincides with the detector centre. The process starts with the initial value

$$\vec{r}_{0,\mathrm{init}} = c \cdot \frac{\sum_j q_j \vec{r}_j}{\sum_j q_j}, \tag{4.3}$$

chosen as the charge barycentre multiplied by a constant c. c is being determined in a MC study. Here, q_j is the total amount of charge reconstructed for the jth PMT. When the node for maximum $\mathcal{L}$ was found, it serves as new $\vec{r}_0$ for a finer grid. The iteration procedure is repeated until the node distance drops below a predefined value.

In order to obtain a suitable pdf, the luminescence function for LSc given by Equation (2.7) is convolved with a Gaussian that takes into account the PMT timing uncertainty. Only first PMT hits are considered in the reconstruction. Therefore, a correction is applied regarding the fact that the pdf profile sharpens the more hits a PMT has. It was found that it is sufficient to use four individual pdfs for up to four PMT hits, and one additional pdf for five or more hits. The respective pdf curves are depicted in Figure 4.3 (a).

To reduce the impact of re-emitted and scattered photons, hits outside the time window $-5\,\mathrm{ns} < t_{i,\mathrm{res}} < 30\,\mathrm{ns}$ are rejected for reconstruction.

The vertex resolution in one dimension is shown for different TTS assumptions over energy in Figure 4.3 (b) as stated in [117]. At 1 MeV, the most realistic configuration with $\sigma = 4\,\mathrm{ns}$ leads to an uncertainty of $\approx 11\,\mathrm{cm}$. As expected, the precision increases to higher energies due to the higher amount of information in terms of PE counts.

It has to be noted that, other than for the shown result, in the current `offline` distribution the geometrical model used for the tof calculation does not consider refraction at optical transitions between LSc, acrylic and water.

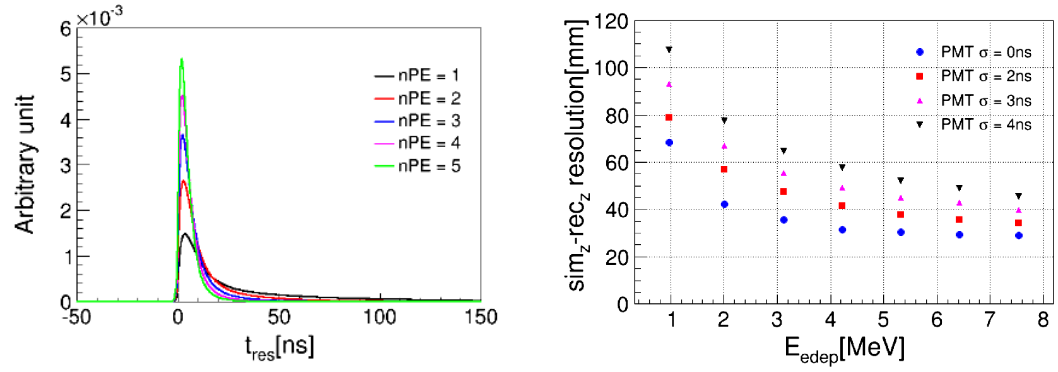

(a) $f_{\mathrm{res}}(t_{i,\mathrm{res}})$ for different numbers of PMT hits.

(b) Vertex resolution over energy.

Figure 4.3: Pdfs used in the default `offline` vertex reconstruction and its performance. Taken from [117].

The knowledge of the vertex is very important to determine how much energy E was deposited in the LSc volume. Mainly due to light attenuation and refractive effects, the total number n_{PE} of photoelectrons at a given energy depends on the vertex. JUNOs spherical design by approximation reduces the problem to a function of the detector radius r at which the event took place. Accordingly, n_{PE} is by a correction factor $f(r)$ obtained from simulated calibration runs. Figure 5.10 shows the simulated number of detected photons as a function of r. It can be seen how, after a continuous rise, the function drops again beyond a peak around 16 m as a consequence of total reflection near the detector edge.

In principle, the energy reconstruction could follow an outline similar to the vertex reconstruction. [118] describes how E can be determined with the required precision below $3\,\%/\sqrt{E}$ by maximising a likelihood function. The respective pdf is constructed to describe the probability of each PMT to have seen the observed number of hits given the relative position of PMT and vertex and an assumed E.

Chapter 5

Topological Event Reconstruction

The event discrimination presented in Chapter 6 is based on an innovative concept for event reconstruction in large LSc detectors, in the following referred to as topological reconstruction (TR) [4, 119]. The descriptive name reflects the fact that the result represents a spatial probability distribution for the origin of photon emission. For multi GeV muons the resolution allows to determine the deposited energy, reconstruct the muon track, and even make out energy loss features along the muon track. Thus it holds potential for the identification of cosmogenic hadronic showers, enabling individually shaped muon vetoes in order to reduce the dead time of an experiment.

A remarkable aspect is the fact that the algorithm does not rely on a particle hypothesis. Assuming only knowledge of a single point in space and time that the particle has passed, the TR can calculate the track without depending much on the detector geometry.

Section 5.1 explains the basic idea behind the TR with the formalism established in [4] and highlights some implementation details. Section 5.2 describes changes that have been applied to the TR software in the scope of this thesis. This includes the adaptation to the JUNO experiment (Section 5.2.4), the treatment of several PMT subsets (Section 5.2.1), the choice of technique for vertex reconstruction (Section 5.2.2) and the so-called crystallisation algorithm (Section 5.2.5).

5.1 Reconstruction Principle

5.1.1 Basic Formalism

Large LSc detectors measure hits on their light sensors subsequent to energy deposition from a primary particle. The treatment of hit times in the TR can be explained starting

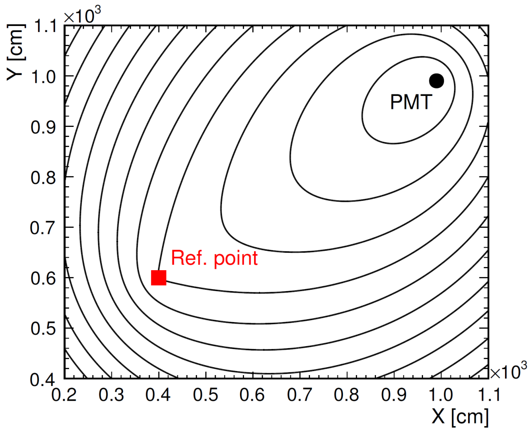

(a) Two-dimensional depiction of isochrones which emerge in the reconstruction of the emission point from a single detected photon. It was assumed that the photon emission happened after the primary particle had passed $\vec{r}_{\text{ref}}$. t_s was set to 0.

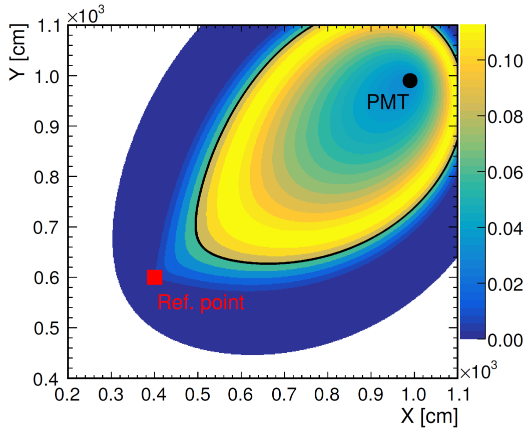

(b) Smearing of an isochrone due to the statistical time uncertainties introduced by the scintillation process and the electronics response.

Figure 5.1: Depiction of the drop-shaped probability distribution that emerges for a single detected photon. Taken from [4].

from a simple model. Given that at least one reference point $\vec{r}_{\text{ref}}$ is known which the primary particle has passed at the – likewise known – reference time t_{ref}, it is assumed, firstly, that the particle has travelled on a straight line at the speed of light c and, secondly, that a photon which has been detected by a sensor located at $\vec{r}_j$ came directly from the emission point $\vec{x}$ along the particle track. The hit time t_j can then be expressed in the form

$$t_j = t_{\text{ref}} \pm \frac{|\vec{x} - \vec{r}_{\text{ref}}|}{c} + \text{tof}_\gamma(\vec{x}, \vec{r}_j) + t_s. \tag{5.1}$$

The sign in front of the second term depends on whether $\vec{x}$ was reached before or after $\vec{r}_{\text{ref}}$. The photon time of flight tof_γ is a function of emission point and sensor position and can be determined using the photon group velocity in the medium (see Equation (2.12)). t_s considers statistical fluctuations that arise from the scintillation process and the time uncertainty of the photo sensor.

Potential points of photon emission can be identified by solving Equation 5.1 for $\vec{x}$. Figure 5.1 (a) shows the two-dimensional depiction of isochrones which arise for an exemplary constellation of reference point and PMT location assuming different hit times and a t_s fixed to 0. The isochrones get a typical drop-like shape when the time of photon emission is assumed to be later than t_{ref}.

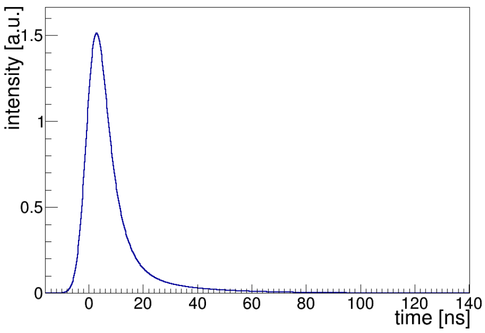

(a) The probability density function ϕ_{t_s} considering a delay due to scintillation and a 3 ns TTS of the photo sensor.

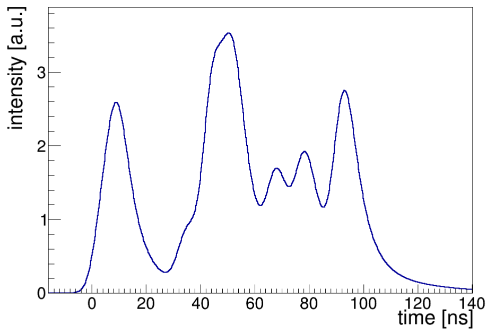

(b) Example for an unnormalised signal function. The shape of ϕ_{t_s} was superimposed for 10 randomly distributed hits with charges varying between 0.5 and 1.8.

Figure 5.2: Treatment of timing uncertainty in signal functions.

Although the exact t_s stays unknown in a photon measurement it can be treated statistically with respect to a probability density function ϕ_{t_s}. ϕ_{t_s} is a convolution of the scintillation function (Equation 2.7) and the time uncertainty of the photo sensor, approximated by a Gaussian. An exemplary ϕ_{t_s} with the scintillation parameters used in the JUNO simulation (see Table 4.1) and a TTS (FWHM) of 3 ns is plotted in Figure 5.2 (a). The effect on the solution of Equation (5.1) is a smearing of the formerly sharp isochrones. An example is shown in Figure 5.1 (b).

The probability density for the emission point of the kth hit on the jth photo sensor can be expressed as

$$\phi_{j,k}(\vec{x}) = w_{j,k}\varepsilon_j(\vec{x}) \int_0^\infty \phi_{t_s}(t')\phi_{\mathrm{tof}_\gamma}(t,\vec{x},\vec{r}_j)\mathrm{d}t'. \tag{5.2}$$

Here, $\phi_{\mathrm{tof}_\gamma}(t,\vec{x},\vec{r}_j)$ denotes a probability density distribution that considers the tofs of multiple photon pathways and hence takes into account the extent of the sensor. The purpose of the integral is to match the statistical expectation of a hit at $t_j - t_{\mathrm{ref}}$ with the tof corresponding to $\vec{x}$ and $\vec{r}_j$. The prefactor $\varepsilon_j(\vec{x})$ considers the position-dependent detection efficiency. This includes light attenuation, the solid angle defined by the sensor, and its angular acceptance. The normalisation factor

$$w_{j,k} = \left(\int_{V_{\mathrm{LSc}}} \varepsilon_j(\vec{x}) \int_0^\infty \phi_{t_s}(t')\phi_{\mathrm{tof}_\gamma}(t,\vec{x},\vec{r}_j)\mathrm{d}t'\mathrm{d}V\right)^{-1} \tag{5.3}$$

makes sure that Equation (5.2) satisfies

$$\int_{V_{\mathrm{LSc}}} \phi_{j,k}(\vec{x})\mathrm{d}V \stackrel{!}{=} 1, \tag{5.4}$$

which requires the photon to originate from the LSc Volume.

In order to include the information from all hits and sensors, the single hit contributions can be summed up according to

$$\Gamma_{\mathrm{det}}(\vec{x}) = \sum_{j} \Gamma_{\mathrm{det}_j}(\vec{x}) = \sum_{j,k} \phi_{j,k}(\vec{x}). \tag{5.5}$$

The detection efficiency is usually not homogenous over the detector. Therefore, the probability density for detected light $\Gamma_{\mathrm{det}}(\vec{x})$ must be divided by the summed local detection efficiency of all sensors in order to get the probability density for emitted light $\Gamma_{\mathrm{em}}(\vec{x})$:

$$\Gamma_{\mathrm{em}}(\vec{x}) = \frac{\Gamma_{\mathrm{det}}(\vec{x})}{\sum_j \varepsilon_j(\vec{x})}. \tag{5.6}$$

5.1.2 Iteration Process with a Probability Mask

In spite of the superposition introduced in Equation (5.5) the information from the single photo sensors was treated independent of each other so far. However, one can be take advantage from the fact that the photon emissions are correlated since they all originate from the same primary particle. It is very likely that the kth hit on the jth photo sensor is due to an emission from the event topology that is indicated by all other hits. It is thus reasonable to reweigh the contribution of each single hit with the information provided by other sensors. A probability mask, i.e. a spatial map of prior information, is folded with the probability density map from the single hits given by Equation (5.2). Care has to be taken that the probability mask does not contain information from the very same sensor in order to avoid simple self enhancement which would not reflect real information.

The reweighing can be done for all sensors – and multiple times, with each iteration confining the emission topology more to the actual primary track. The number of iterations is limited by the degree of approximation during implementation.

5.1.3 Implementation Details

The embedding of the described principle into a software framework demands a strategy that is applicable to different detectors and also flexible in the configuration for variable event types. Furthermore, the time needed to run the algorithm is required to be short.

The implementation has been written in the programming language `C++` and has an object-oriented structure. All classes dealing with the specific detector properties such as geometry, electronics response, and the optical model inherit from generic classes.

During the actual algorithm a loop runs over all photo sensors. A signal function is built for every sensor. It is given as a superposition of curves defined by the shape of ϕ_{t_s}, shifted to the positions of the registered single hit times of that sensor and scaled with the respective charges. An example for 10 random hits is shown in Figure 5.2 (b).

The calculation operations are carried out on a grid structure. For every node m at position $\vec{x}_m$ on the grid, the value of the signal function is requested at the tof to the current sensor j at position $\vec{r}_j$. It is multiplied by the local detection probability $\varepsilon_j(\vec{x}_m)$ and the local value of the current probability mask. The repetitive calculations for tof and ε_j are done beforehand and stored in look-up tables (LUTs) as a function of distance between PMT position and emission point and angle between PMT norm vector and emission point as seen from the PMT.

The iteration process can be specified at runtime in an `ASCII` configuration file. The grid can be refined and confined to a subregion of the detector from iteration to iteration with growing precision of the reconstruction. This allows to save computation time. The entries in the probability mask in the initial calculation cycle are set to a constant value. It turned out that for the following iterations self enhancement effects can be avoided by using alternating subsets of light sensors, while the result of the previous iteration is used as probability mask.

Figure 5.3 shows the development of the reconstruction result after different numbers of iterations. The depicted event is the simulation of a 3 GeV muon in the LENA detector [107]. The continuous lines show the true track of the primary particle (red) and secondary particles (black). The resulting number density of emitted photons is projected on the XY-plane of the detector. It is visible how the gain in precision goes along with a spatial confinement and refinement of the grid. Regions of multiple secondary emission are visible after 21 iterations.

5.1.4 Artefacts and Edge Effects

Several approximations lead to effects that do not reproduce actual event information. One issue is the scattered light component. Since every photon is treated as coming directly from the emission point, scattered photons, which can make out several ten per cent of the total light amount, create an uncorrelated contribution to the result, manifesting itself as a veil of mist lying over the reconstructed picture. Furthermore, scattered light leads to artefacts as soon as the grid is constrained to a detector sub-

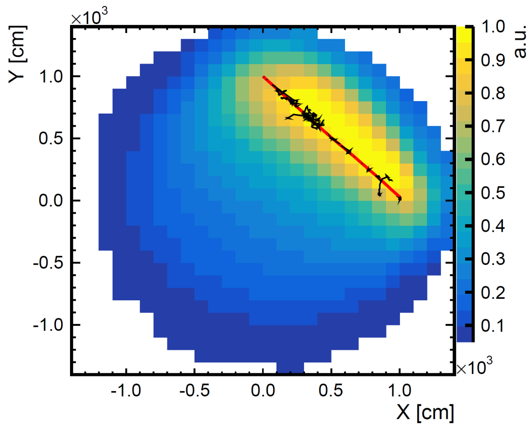

(a) Iteration 0

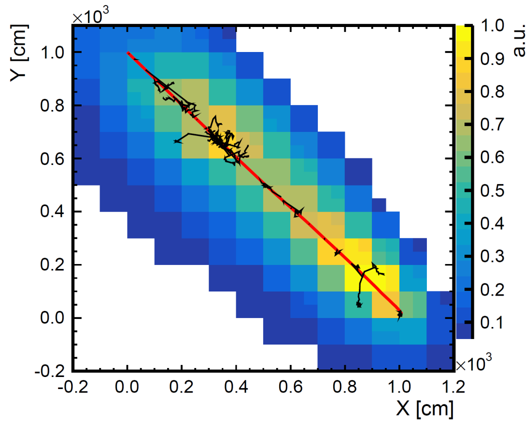

(b) Iteration 8

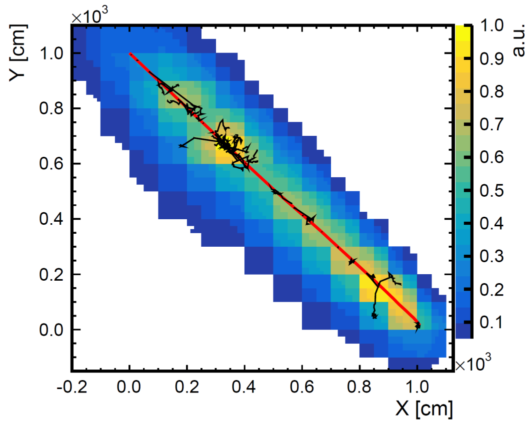

(c) Iteration 21

Figure 5.3: Development of the reconstruction result after different numbers of iterations for a 3 GeV muon simulated in the LENA detector. The continuous lines show the true track of the primary particle (red) and secondary particles (black). The resulting number density of emitted photons is projected on the XY-plane of the detector. Taken from [119].

volume. Although the scattered photons might come from within the grid bounds, the extended tof can render the most probable origin to lie outside. Normalisation leads to a visible contribution at the nearest grid edge, resulting in bright regions near the outskirts of the confined volume. A simple way to suppress edge artefacts is to strongly diminish the outermost bins of the probability mask. The impact of scattered light can further be reduced on a statistical basis. As introduced in [120], a probability to be direct light can be assigned to every detected photon, depending on its arrival time and given a basic topology. The probability is later used to weigh the respective hit contribution in the signal function.

So far, scintillation was assumed to be the origin of all photons. Since Cherenkov light makes out a small fraction on the per cent level, its anisotropic emission can lead to a minor bias of the topology. Eventually being a valuable source for directional information, a statistical treatment of potential Cherenkov photons is currently under investigation.

For detectors with light sensors inside or very close to the active detector volume, emission regions near the sensor plane, i.e. at distances comparable to the sensor size, can lead to a strong overvaluation of that region due to an excessive exposure of single sensors. On the one hand, this leads to a disproportional estimation of deposited energy. On the other hand, it turned out that very bright regions in the topology have the tendency to concentrate the surrounding probability depositions in following iterations more than is physically justifiable. It was found reasonable and useful to blind very close sensors during reconstruction [120].

At some point, further iterations will reproduce and enhance artefacts more than they provide new real information. Hence, it is a general task to find an optimal number of iterations and not to overdo the process.

5.2 Adaptation to JUNO and Further Development

As the second part of this chapter, this section describes the major contributions that have been made to the TR in the scope of this work.

The TR, as it was described in [119], has been designed in connection with LENA as a flexible framework, having in mind the option to adapt the tool to other experiments. JUNO, with its exceptionally high light yield, is an ideal scope of application. The adaptation had to be addressed on different levels:

Source Code Various classes needed to be added in order to treat JUNO data independently from other experiments during reconstruction. In doing so, much of the code structure could be taken over from LENA, while single passages demanded for changes.

One such aspect is the definition of PMT locations (see Section 5.2.1), another is the determination of a reference point in space and time (see Section 5.2.2).

External Look-up Tables Some repetitive calculations have been externalised in order to save computation time. These are the local detection probability for a single PMT, earlier referred to as $\epsilon_j(\vec{x})$, and the local time of flight $\mathrm{tof}(\vec{x})$. Basically, these variables carry the influences of the experiment's optical model. The generation of look-up tables for JUNO is explained in Section 5.2.4.

Configuration Files Many detector parameters and strategy options can be configured at runtime. Configuration files were created to control the reconstruction for JUNO.

Input Data As long as JUNO is not taking experimental data only Monte Carlo (MC) simulations can be analysed. Small changes had to be done in the `offline` source code in order to provide all desired MC truth information. Since the variables written to `offline` do not have the structure required by the TR, a converter was written which reduces the `offline` data to the needed variables and transforms them into a structure that can be read in by the TR.

Following the description of the JUNO adaptations, two general implementations are explained, building optional tools for the reconstruction strategy. One is the so-called crystallisation (see Section 5.2.5) and the other is the reduction of the reconstruction mesh to a spherical subregion of the detector (see Section 5.2.6).

5.2.1 PMT Handling

The handling of light sensors was changed with regard to LENA in two respects. Where the positions of the LENA PMTs were calculated in accordance with the scheme used for MC simulation, the PMT positions in JUNO are read from an `ASCII` file together with their internal ID. All LENA PMTs were treated as identical units. The PMT data file now allows to pass further specific information such as the sensor type – 20" MCP, 20" dynode, or 3" dynode. This is important since different types demand for individual treatment, e.g. it is necessary to build dedicated LUTs. The size and TTS of each type can be specified in the configuration files. However, the reading of the PMT data file can in future be extended e.g. by individual TTS values, orientations, or a label indicating broken tubes.

The second PMT-related feature which was added is the option to disable PMTs of a certain type from the reconstruction via a command in the configuration files. This comes in useful regarding the fact that the large PMTs are outnumbered by the small ones, although the latter collect only a very small fraction of the total photo electrons. Switching them off leads to a remarkable reduction of computation time by the cost of only a minor amount of information. Furthermore, a restriction to PMT subsets allows it to study the types separately, e.g. to evaluate the impact of the low TTS Hamamatsu PMTs.

5.2.2 Vertex Reconstructions

In order to determine the reference point in space and time required by the TR, the LENA framework resorts to a random Gaussian smearing of the MC truth with the corresponding parameters to be controlled in the configuration files. For JUNO this method was left as an option but complemented with the possibility to do a vertex reconstruction based on the PMT data. A vertex reconstruction becomes necessary when, like later in this work, the TRs of different event types are compared against each other. Since different particles have individual ways to deposit energy in the scintillator (see Section 2.1), a unified resolution would not be an appropriate assumption.

The vertex reconstruction now integrated was implemented by D. Meyhöfer and is described in [121]. It incorporates a principle called backtracking. Like in the TR, a three dimensional grid is laid over the detector. From all first hits on the PMTs, which are considered less likely to come from scattered photons than later hits, the tof between a point in the detector and the respective tube is subtracted. A time spectrum is built from the residuals at each node of the grid. Near the true vertex this distribution is expected to reflect the sharp scintillator decay function folded by the PMT TTS and to melt away everywhere else. Therefore, the algorithm searches for the node with the steepest rise. An iterative process with a continuous refinement of the grid while confining its volume allows a very time economic procedure.

The performance of the backtracking method is demonstrated in Figure 5.4 for simulated electron (green markers) and positron (blue markers) events in JUNO. Electronic noise and PMT TTS was both considered. Plot (a) shows the resolution in a single coordinate, which is about 16 cm (29 cm) at 1 MeV visible energy for electrons (positrons). The resolution improves with rising energy and from 6 MeV it lies constantly around 8 cm for both event types. The reason for the worse positron resolution is the emission of annihilation gammas which deposit energy a little offside the spot of positron ionisation. For the absolute distance between the true and reconstructed vertices this means a resolution between 28 cm (46 cm) at 1 MeV and 13 cm above 6 MeV as can be seen in plot (b). The time resolution, depicted in plot (c), is related to the vertex resolution

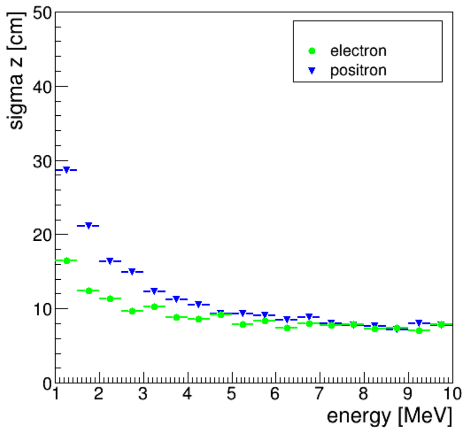

(a) Resolution in a single coordinate.

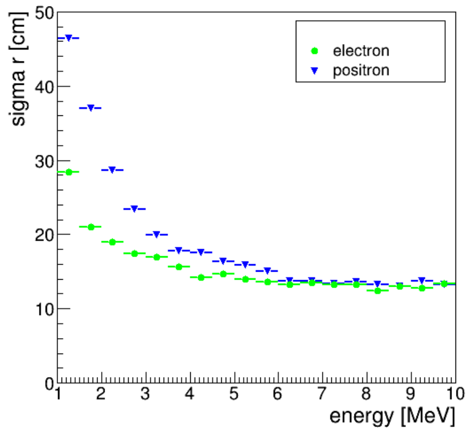

(b) Resolution in the absolute distance between true and reconstructed vertex.

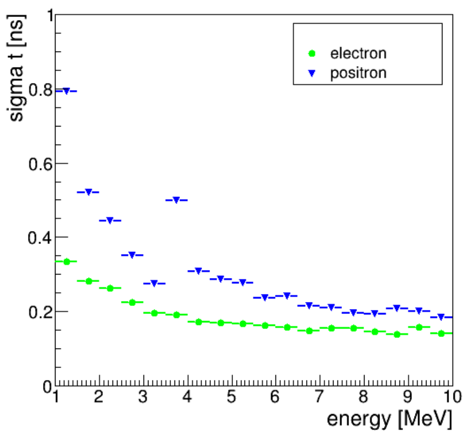

(c) Resolution in time.

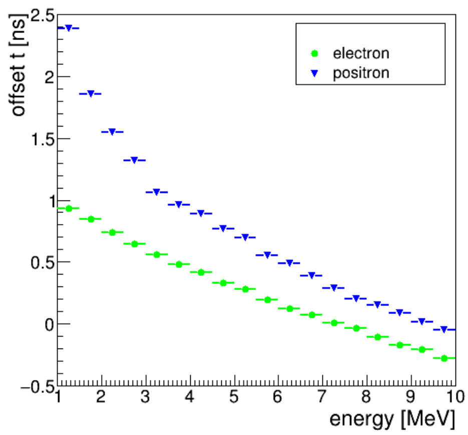

(d) Offset between true time and expectation value for the time reconstruction.

Figure 5.4: Resolution of the backtracking vertex reconstruction included in the TR as a function of the visible energy. The algorithm is described in [121].

and likewise the differences between electrons and positrons linger on. While all electron values stay well below 0.4 ns and even 0.2 ns above 3 MeV, the positron resolutions start off from 0.8 MeV and do not get below 0.2 ns. The outlier around 3.75 MeV is due to a mismatch between the Gaussian fit and the underlying distribution of reconstructed hit times, which in some cases showed non-Gaussian attributes. Although the variance in time reconstruction is small, its mean offset from the true time, shown in plot (d), can be as large as a few ns, depending on the energy. This means, it cannot simply be corrected by a constant shift.

The choice of method for the reference point can be made in the configuration files.

5.2.3 Optical Model

A bunch of optical parameters is necessary to calculate photon trajectories, hit times, and hit probabilities for JUNO. During the development of this work, the final mixture of the JUNO scintillator was still under development, and so the parameters used in the following are adopted from the `offline` simulation. `offline` uses a full optical model, i.e. the parameters are considered as wavelength dependent, see Section 4.1.

Handling of Optical Refraction

In comparison to LENA, the different optical media in the JUNO detector introduce a non-trivial complexity in the LUT calculation. The boundary between LSc and acrylic can be neglected due to an almost identical refractive index (compare Figures 4.2 (c) and (e)), which leaves the transition from acrylic to water (compare Figures 4.2 (c) and (d)). Snell's law of refraction

$$\frac{\sin(\theta_1)}{\sin(\theta_2)} = \frac{n_2}{n_1} \tag{5.7}$$

can be applied here. θ_1 and θ_2 denote the angles of incidence and refraction, respectively, with the corresponding refractive indices n_1 and n_2. Unfortunately, there is no analytical solution for the search for the refraction point on a curved interface. Therefore, the refraction was determined in a semi-analytic way. The path of a photon, inciding at a point $\vec{p}$ on the PMT surface under a certain angle α, can be traced back to the optical boundary on the acrylic sphere, where the refraction can be calculated according to Equation (5.7). Acrylic and LSc is treated optically identical. With an arbitrary number of incident angles, a ray pattern can be laid over the LSc volume of the detector as it is visualised in Figure 5.5 (a), where $\vec{p}$ is placed at $(0, 0)$. An interesting feature is an area free of rays at the upper edge of the hemisphere. Snell's law forbids photons coming from this region to reach $\vec{p}$ directly. The region is defining the detector shell from which emitted photons can undergo total reflection. Light coming from here must either be scattered, absorbed and re-emitted, or reflected somewhere else to reach the PMT. It can be seen that the shape of this blind region is no clean circular segment but rather features a slight kink where several rays cross. Underneath this focal spot, the phenomenon leads to a narrow zone in which rays corresponding to very high incident angles α cross rays with smaller α. Direct photons from this region can reach $\vec{p}$ on two divergent trajectories with sub-nanosecond differences in time of flight.

The final reconstruction LUTs will be stored as histograms in the two dimensions distance d from and angle ϕ to the PMT. It thus makes sense to evaluate the refraction in an equally binned histogram. The ray pattern must be chosen dense enough to ensure that every bin is crossed by at least one ray. The α angle of the crossing ray is filled into the histogram. When more than one ray crosses the bin, a weighted mean value is taken according to the distances covered by the crossing rays. For the small region with two α possibilities, the second α is stored in an extra histogram with equal binning.

A class was implemented which builds these histograms with an arbitrary binning based on a handful of geometrical and optical parameters. It needs to be noted that the point $\vec{p}$ on the PMT surface does not necessarily have to lie within the two-dimensional plane of d and ϕ. In that way the three-dimensional PMT surface can be taken into account when calculating the LUTs for the TR later on.

The class also calculates and returns further relevant values for a given bin, e.g. the point where the photon crosses the optical boundary, the distances that a photon travels in LSc plus acrylic and in water, and the time of flight that this takes.

Figure 5.5 (b) shows the difference $\Delta\text{tof} = \text{tof}_{\text{refr}} - \text{tof}_{\text{norefr}}$ in photon tof between a refracted and a direct photon trajectory towards a PMT. The PMT position marks the origin of the coordinate system. The delay introduced by refraction is found to be well below 1 ns throughout a major part of the detector. The highest deviation of about 1 ns can be seen near the upper edge of the blind region.

Since placing a LSc sphere into a water buffer is a concept that finds use also beyond JUNO, the developed tool can also be applied elsewhere within the scope of the TR like it was already done for SNO+ [122].

Propagation of Cherenkov and Scintillation Light

Although a small light fraction in LSc detectors is due to Cherenkov light, all photons are treated as scintillation light in the TR. If any, the effect on the result is small. Nevertheless, it is worthwhile to have a look into the different characteristics with regard

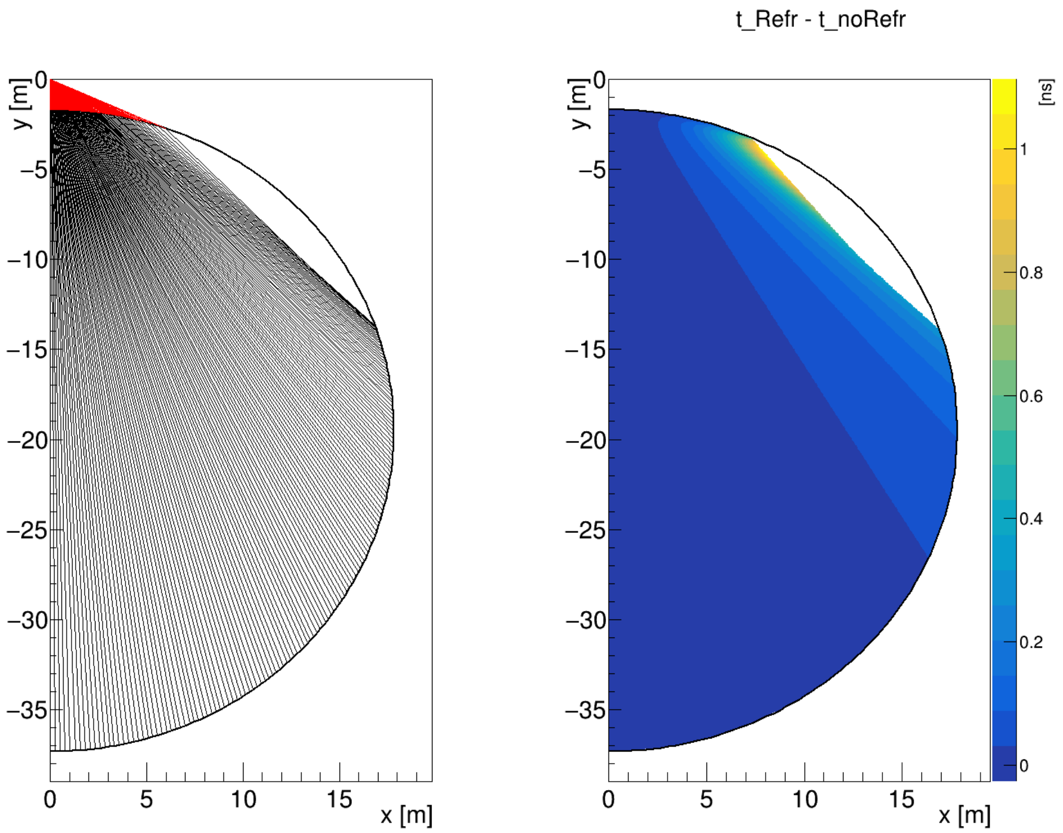

(a) Trajectories for unattenuated photons which are emitted at $(x, y) = (0, 0)$ and refracted at the JUNO arylic sphere. The trajectory parts in water and LSc are depicted in red and black, respectively. The region in the top outer edge of the sphere cannot be reached by photons from that origin. Vice versa, a PMT is blind for direct light emitted from this part of the central detector.

(b) A detector map showing the effect of refraction on the photon time of flight. The colour encodes the difference between the time of flight on a refracted and a direct path.

Figure 5.5: Handling of optical refraction in the topological reconstruction.

to future attempts e.g. towards direction reconstruction.

The implementation of the optical model allows a revealing look at the different hit signatures which one expects on a PMT in terms of hit times. The major effect arises from differences in emission time. In contrast to the immediate emission of Cherenkov light, the emission of scintillation light follows an exponential decay function with a time constant of a few nanoseconds. The disparity is enhanced by the varying spectra – short wavelengths strongly preferred for Cherenkov light in contrast to a peak around 430 nm for scintillation light – that lead to a higher group velocity on average for Cherenkov photons.

In order to study the issue, arrival times were calculated for a fixed number of photons with wavelength distributions corresponding to the scintillation spectrum shown in Figure 4.2 (a) and the Cherenkov spectrum given by Equation (2.10) within the bounds of the quantum efficiency shown in Figure 4.2 (b). The refraction tool described above was used to obtain the photon trajectories. The travelled distances in LSc and water were used to determine the times of flight with the group velocity given in Equation (2.12) in consideration of the refractive indices shown in Figures 4.2 (c) and (d). Furthermore, the travelled distances were used to reduce the hit weights according to the attenuation described by Equations (2.15) and (2.16) with the parameters obtained from the plots shown in Figures 4.2 (f) - (h). The PMT time resolution was not taken into account, neither were the quantum efficiency nor the delay of scintillation photons. In this way the propagation effects can be studied detached from the type of light sensor and the specific timing characteristics of the LSc.

Figure 5.6 shows results for two different points in the detector. The positions in the JUNO detector are indicated by red marker in the left frames. The light sensor is placed at $(x, y) = (0, 0)$. The middle and right frames show the arrival time spectra for scintillation and Cherenkov light, respectively, shifted by the mean tof. For a close-by emission point (top row of plots), the form of both spectra is rather sharp. The immediately emitted photons arrive with a full width at quarter maximum (FWQM) of 0.10 ns (0.30 ns), given the emission spectrum for scintillation light (CR). The slight effect of refractive indices on the group velocities gets more pronounced for longer tof. Emission from the other side of the detector (bottom row of plots) leads to a FWQM of 0.66 ns (1.6 ns). Light sensors with sub-nanosecond time resolution, e.g. LAPPDs, should be able to identify at least a fraction of the CR, especially in combination with a slow LSc.

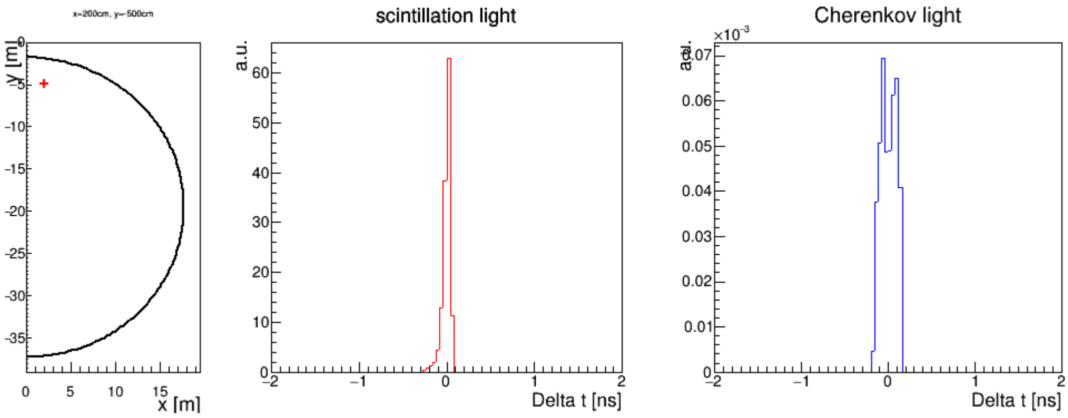

(a) Emission point $(x, y) = (200, -500)$ cm.

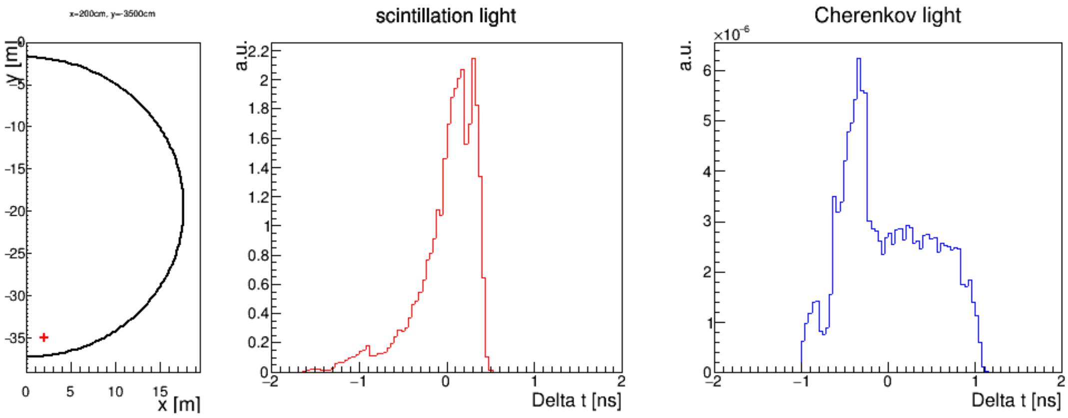

(b) Emission point $(x, y) = (200, -3500)$ cm.

Figure 5.6: Effect of emission spectra on photon arrival times, both for scintillation (middle) and Cherenkov light (right). The left plot shows the emission point in the detector as a red marker. The position of the light sensor is $(x, y) = (0, 0)$.

5.2.4 Pre-Calculation of Lookup Tables

Variables depending only on the detector but not on the actual event can be determined and written outside the reconstruction process and loaded when needed. This handling speeds up the program. The variables can be stored in a two-dimensional histogram as a function of distance and absolute angle with respect to the position and normal vector of each PMT. The spherical symmetry in JUNO allows it to use one LUT for every tube of the same type.

In general, there are two options for LUT generation, either in a MC simulation or by calculation. A simulation on the one hand has the advantage that it takes into account a whole bunch of physical effects and considers complex geometrical aspects such as shadowing from the static support structure without further ado. But it also bears the risk of systematically favouring the reconstruction which runs on data provided by the very same MC framework as the LUT. A calculated LUT on the other hand is independent of the MC data and is quite flexible to adjust and turn on or off physical effects at will. Furthermore, events at long distances demand for an extensive simulation effort in order to compensate for the low hit count. The calculated LUT is not limited by statistics.

This section describes the calculation of LUTs and compares the results to simulations.

Direct Light Probability

A LUT is needed to provide the probability of a PMT to see direct light emitted at a distance d under the angle ϕ. Different aspects enter into the calculation. The first one is visibility, i.e. the probability p_{vis} of a photon to be emitted in a direction that is covered by the PMT surface. The second one is the probability p_{surv} of photons to reach the PMT unaffected by any attenuation effects, i.e. absorption and scattering, or by reflection. In principle, a third component could consider the PMT acceptance of the photon's incidence angle, but since the angular acceptance is not taken into account in the `offline` simulation it was neither done here.

In order to account for the three-dimensional shape of the PMT, its surface was approximated as a hemisphere and divided into samples which are considered one by one for points in the detector. Photon emission is assumed to be isotropic. Due to refraction at the boundary from acrylic to water, p_{vis_i} cannot simply be taken as the solid angle that the area of the ith sample covers with respect to $\vec{x}$. Instead, the points $\vec{c}_1$ and $\vec{c}_2$ on the boundary are determined at which two opposite sample edges are visible from $\vec{x}$ by using the refraction tool described above. The opening angle ω_i between these points as seen from $\vec{x}$ are used in order to calculate the solid angle Ω_i according to

$$\frac{\Omega_i}{4\pi} = \sin^2\left(\frac{\omega_i}{4}\right) = p_{\mathrm{vis}_i}. \tag{5.8}$$

p_{surv_i} is given by attenuation as described in Section 2.3. The Rayleigh scattering length and absorption length as depicted in Figure 4.2 is used to solve Equation (2.15) for the path distance between $\vec{x}$ and $\vec{p}$ as obtained from the refraction tool.

The total direct light probability at a fixed photon energy is then given as the sum

$$P(\vec{x})|_{E_l} = \sum_i p_i(\vec{x})|_{E_l} = \sum_i p_{\mathrm{vis}_i}(\vec{x})|_{E_l} \cdot p_{\mathrm{surv}_i}(\vec{x})|_{E_l}. \tag{5.9}$$

over all sample points on the PMT surface. To account for the JUNO optical model, $P(\vec{x})$ is determined for different wavelengths E_l in the range of the LSc emission spectrum. The resulting values $P(\vec{x})|_{E_l}$ are averaged according to

$$\overline{P(\vec{x})} = \overline{P_{\mathrm{unsc}}(\vec{x})} = \frac{\sum_l I(E_l)\varepsilon_{\mathrm{QE}}(E_l)P(\vec{x})|_{E_l}}{\sum_l I(E_l)\varepsilon_{\mathrm{QE}}(E_l)} \tag{5.10}$$

with $I(E_l)$ being the intensity of the emission spectrum and $\varepsilon_{\mathrm{QE}}(E_l)$ the quantum efficiency at the respective energy.

The resulting LUT for direct light can be seen in Figure 5.7 (a). The PMT samples were chosen as $3\,\mathrm{cm} \times 3\,\mathrm{cm}$ squares on the geometrical base of the PMT surface, projected onto a hemisphere. 10 equidistant wavelengths were used to determine $\overline{P(\vec{x})}$.

In order to compare the calculated result, a simulation was carried out in the JUNO `offline` framework. 10^5 electrons with kinetic energies of $0.5\,\mathrm{MeV}$ were spread throughout the LSc volume. The low energies make sure that all primary photons are emitted very close to the specified vertex. The high number of nearly $18,000$ PMTs in the detector allows it to determine the number of detected over emitted photons for as many combinations of distance and angle to a PMT per event. Here, only the direct photons were counted as hits. The combination of all events and PMTs results in the LUT depicted in Figure 5.7 (b).

Apart from a coarser binning and small fluctuations due to statistics, the two LUTs are very much alike and share all general tendencies. The location of the blind region is almost identical. The bending of equivalent lines is very similar, especially towards the blind region. The probabilities in both approaches share almost the same scale, although the calculated LUT shows slightly higher values. This might be due to reflections at the optical boundaries which were only considered in the simulation. The same effect can explain a small region of relatively strong overestimation in the calculated approach near

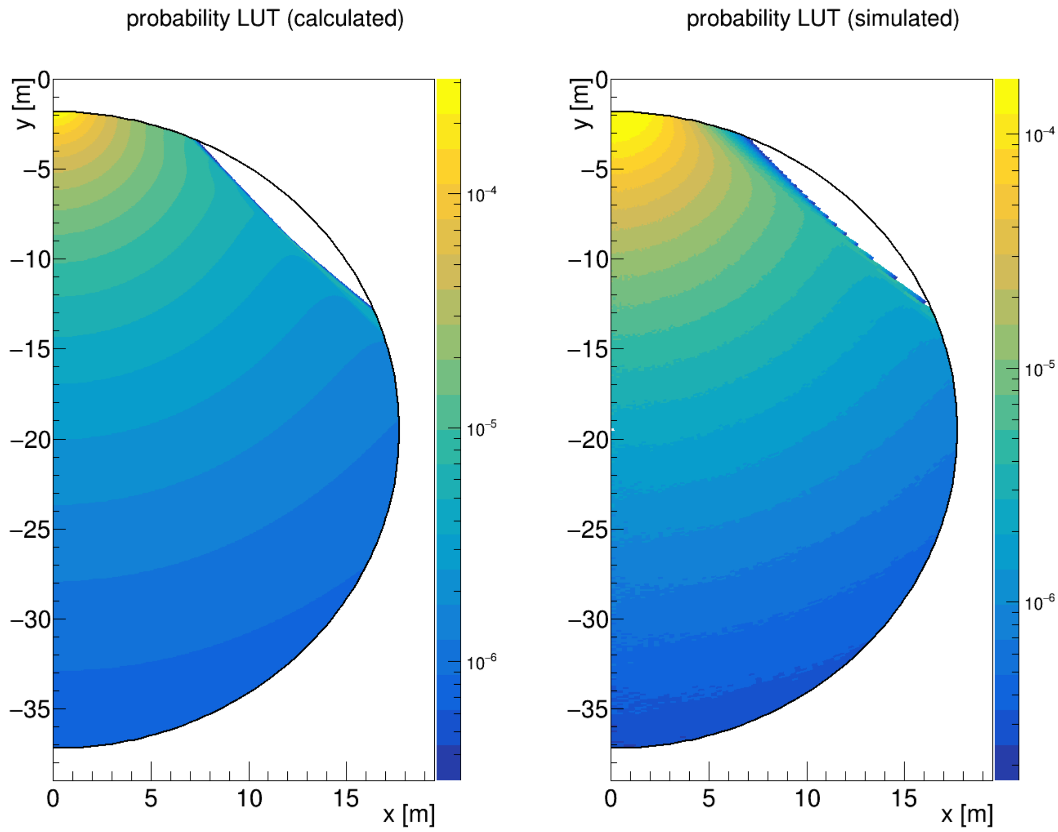

(a) (b)

Figure 5.7: LUTs containing the probability for photons to hit a 20" PMT placed at (x,y)=(0,0), obtained from both calculation (a) and simulation (b).

the upper edge of the blind region. Here, the photons approach the optical boundary under bigger angles and thus face an increased reflectance.

Time of Flight

A second table is needed to lookup the tof from a point in the detector to a PMT. Technically, the broad PMT area and the dynamic refractive indices allow it for photons to reach the tube on various trajectories from a point $\vec{x}$ and thus lead to a tof spectrum rather than a distinct value. For the sake of practicality, only one value is written to the LUT, as it was already practised for LENA [119]. This is justified by the observation that the variance in hit times from one detector point is considerably smaller than their smearing due to TTS.

Along with the determination of $p_i(\vec{x})$ for every sample point, the time of flight

$$\mathrm{tof}_i(\vec{x}) = \frac{d_{\mathrm{xc}}}{v_{g_{\mathrm{LSc}}}(\lambda(E_l))} + \frac{d_{\mathrm{cp}}}{v_{g_{\mathrm{H2O}}}(\lambda(E_l))} \tag{5.11}$$

is obtained for a fixed wavelength $\lambda(E_l)$. Here, d_{xc} and d_{cp} denote the travelled distances in LSc and water, respectively, and v_g is the group velocity as given by Equation (2.12). The weighted mean value

$$\mathrm{tof}(\vec{x})|_{E_l} = \frac{\sum_i p_i(\vec{x})|_{E_l} \mathrm{tof}_i(\vec{x})|_{E_l}}{\sum_i p_i(\vec{x})|_{E_l}} \tag{5.12}$$

over the whole PMT surface is taken. It needs to be mentioned that for the small detector region with two solutions for the incident angle $\alpha(\vec{x})_i$ only the shorter tof_i was considered.

Analogous to the probability LUT, the relevant wavelength range is divided into intervals, and the emission intensity and quantum efficiency are being used to weight the tof:

$$\overline{\mathrm{tof}(\vec{x})} = \overline{\mathrm{tof}_{\mathrm{unsc}}(\vec{x})} = \frac{\sum_l I(E_l)\varepsilon_{\mathrm{QE}}(E_l)\mathrm{tof}(\vec{x})|_{E_l}}{\sum_l I(E_l)\varepsilon_{\mathrm{QE}}(E_l)}. \tag{5.13}$$

Figure 5.8 (a) shows the resulting LUT. The tof values range from a few to 180 ns. Again, a second LUT was obtained from the `offline` simulations described previously. It is depicted in Figure 5.8 (b). Apart from a slightly higher granularity due to the coarser binning, the two results show hardly any difference, which underlines that the geometrical model used in the calculated approach satisfies the conditions, and also indicates that the small divergences observed in the two probability LUTs can be reduced to attenuation effects including reflection.

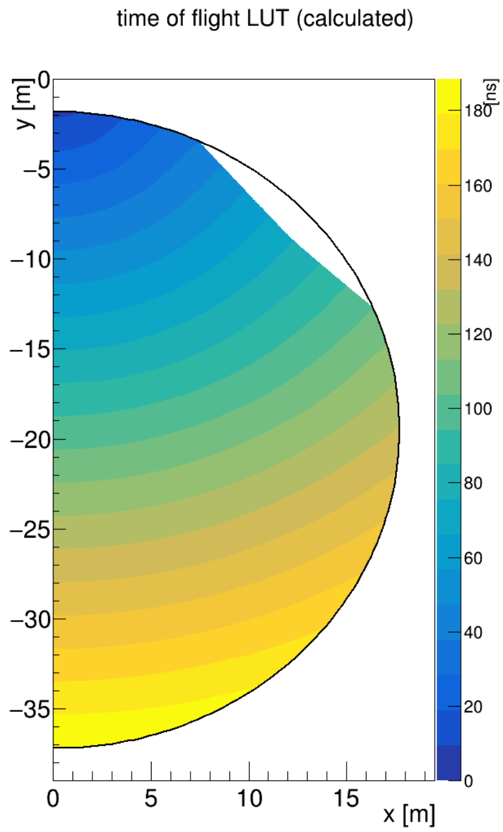

(a)

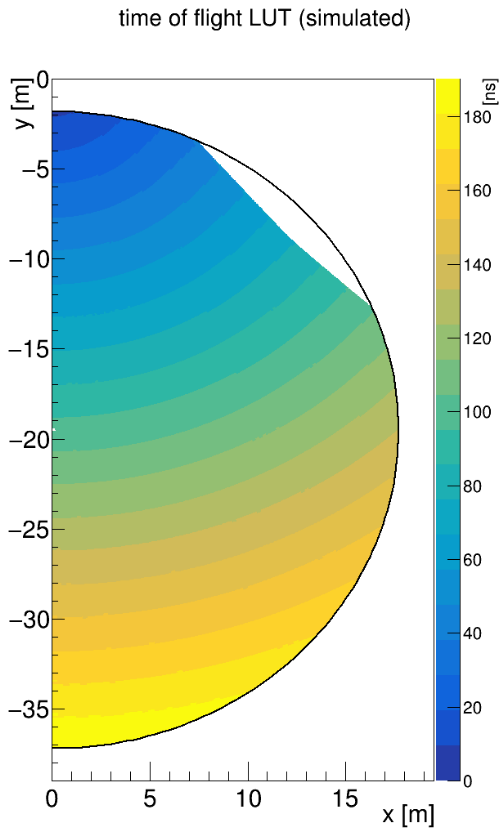

(b)

Figure 5.8: LUTs containing the time of flight for photons to hit a 20" PMT placed at (x,y)=(0,0), obtained from both calculation (a) and simulation (b).

Single Scattering

The statistical treatment of scattered photons within the algorithm described in [120] demands for a LUT containing the spectrum of arrival times from scattered photons originating from a point $\vec{x}$ relative to the PMT position $\vec{p}$.

The task can be addressed by considering at first only single-scattered photons. When the scatter point $\vec{s}$ is confined to the LSc volume, the photon will propagate from $\vec{x}$ to $\vec{s}$, from there to the cross point $\vec{c}$ on the boundary between acrylic and water – again, the optical boundary between LSc and acrylic is being neglected – and finally to the ith sample point $\vec{p}_i$ on the PMT, travelling on straight lines with distances $d_{\overline{xs}}$, $d_{\overline{sc}}$, and $d_{\overline{cp}}$, respectively. The scattering happens immediately and does not introduce a delay, so the time of flight is given by

$$\begin{aligned}\mathrm{tof}_{i,1\mathrm{sc}}(\vec{x},\vec{s})|_{E_l} &= \frac{d_{\overline{xs}}}{v_{g_{\mathrm{LSc}}}(\lambda(E_l))} + \frac{d_{\overline{sc}}}{v_{g_{\mathrm{LSc}}}(\lambda(E_l))} + \frac{d_{\overline{cp}}}{v_{g_{\mathrm{H2O}}}(\lambda(E_l))} \\ &\approx \frac{d_{\overline{xs}}}{v_{g_{\mathrm{LSc}}}(\lambda(E_l))} + \overline{\mathrm{tof}_{\mathrm{unsc}}(\vec{x})}.\end{aligned} \tag{5.14}$$

Adding the first term to the tof obtained from the LUT for direct light yields an approximated tof for the trajectory.

A spherical grid, centred around $\vec{x}$ with equidistant radii, is established for the calculation process. The grid points are one by one considered as potential scatter points $\vec{s}_j$. In order to determine the relative contribution of a constellation $(\vec{x},\vec{s}_j)$ to the time spectrum, $\mathrm{tof}_{i,\mathrm{sc}}$ needs to be weighted by the probability $p_{i,1\mathrm{sc}}(\vec{x},\vec{s}_j)$ of a photon to follow this exact trajectory. The factors that need to be considered here are the probability p_{vis_j} of the photon to be emitted in the direction of $\vec{s}$, the probability p_{surv_j} to reach $\vec{s}_j$ unattenuated, the probability p_{sc} to be scattered when reaching $\vec{s}_j$, the probability p_{vis_i} to be scattered into the direction of $\vec{p}_i$, and the survival probability p_{surv_i} from $\vec{s}_j$ to $\vec{p}_i$.

Assuming isotropic light emission, p_{vis_j} can be replaced by the solid angle that a grid cell covers, which is the inverse number of grid points N_r at the grid radius r of the respective cell. p_{surv_j} is given by Equation (2.3). p_{sc} can be approximated by assuming a scattering between the current and the next inner grid point at radius $r - \Delta r$.

Rayleigh scattering, the dominant scattering process, is not isotropic. The intensity rather shows a $1+\cos^2\theta$ dependency of the scattering angle θ. p_{vis_i} can thus be considered as the solid angle that the sample area effectively covers, weighted by this factor and normalised by its 4π integral. Since solid angle and p_{surv_i} were already calculated in the unscattered case, it is fair to take the value from the corresponding LUT.

The final probability reads

$$\begin{aligned} p_{i,1\mathrm{sc}}(\vec{x},\vec{s}_j) &= p_{\mathrm{vis}_j} \cdot p_{\mathrm{surv}_j} \cdot p_{\mathrm{sc}} \cdot p_{\mathrm{vis}_i} \cdot p_{\mathrm{surv}_i} \\ &\approx N_r^{-1} \cdot e^{-\frac{d_{\overline{xs}}-\Delta r}{l_{\mathrm{att}}}} \cdot \left(1 - e^{-\frac{\Delta r}{l_{\mathrm{Ray}}}}\right) \\ &\quad \cdot \frac{1+\cos^2\theta}{\int_0^{2\pi}\int_0^{\pi}(1+\cos^2\theta)\sin\theta \mathrm{d}\theta \mathrm{d}\phi} \cdot \overline{P_{\mathrm{unsc}}(\vec{s}_j)}, \end{aligned} \tag{5.15}$$

where l_{Ray} and l_{att} are the Rayleigh scattering and attenuation lengths in LSc, respectively. To get a smooth spectrum, Δr should be chosen small and N_r high. Furthermore, E_l can be varied.

It makes sense to include also absorbed and re-emitted photons to the tof spectrum. This can be included in Equation (5.15) by replacing p_{sc} with $(p_{abs} \cdot p_{re})$. The probability $p_{abs} = (1 - e^{-\frac{\Delta r}{l_{\mathrm{abs}}}})$ for absorption within Δr follows analogously to p_{sc} with the absorption length l_{abs}. The energy dependent re-emission probability p_{re} was taken from the JUNO `offline` optical parameters.

Due to the delayed re-emission, the shape of the time spectrum is stretched to higher times. A second entry was added to the spectrum with a constant delay of 1.5 ns according to the expectation value used in the `offline` simulation. The entry was weighted by the respective probability. The resulting spectrum is added as a third dimension to the established LUT format. The spectrum at 800 cm distance and 17° angle is depicted in Figure 5.9 as an example. The tail of the distribution is much longer than in the scintillation function.

Theoretically, an extension to multiple scattering is possible by iterating the process and simply replacing the corresponding LUT term with its predecessor, i.e.

$$\mathrm{tof}_{i,(n+1)\mathrm{sc}}(\vec{x},\vec{s})|_{E_l} \approx \frac{d_{\overline{xs}}}{v_{g_{\mathrm{LSc}}}(\lambda(E_l))} + \overline{\mathrm{tof}_{n\mathrm{sc}}(\vec{x})} \qquad \text{and} \tag{5.16}$$

$$\begin{aligned} p_{i,(n+1)\mathrm{sc}}(\vec{x},\vec{s}_j) &\approx N_r^{-1} \cdot e^{-\frac{d_{\overline{xs}}-\Delta r}{l_{\mathrm{att}}}} \cdot \left(1 - e^{-\frac{\Delta r}{l_{\mathrm{Ray}}}}\right) \\ &\quad \cdot \frac{1+\cos^2\theta}{\int_0^{2\pi}\int_0^{\pi}(1+\cos^2\theta)\sin\theta \mathrm{d}\theta \mathrm{d}\phi} \cdot \overline{P_{n\mathrm{sc}}(\vec{s}_j)}. \end{aligned} \tag{5.17}$$

However, the observations in MC studies show that multiple scattering is a rare process and the spectrum from single scattering was considered sufficient for the purpose of identifying scattered photons. Figure 5.11 (a) shows the TR of a 3 MeV electron event under the use of the scattered-light algorithm in JUNO. The contrast is strongly enhanced when compared to the regular reconstruction of the same event depicted in Figure 6.3

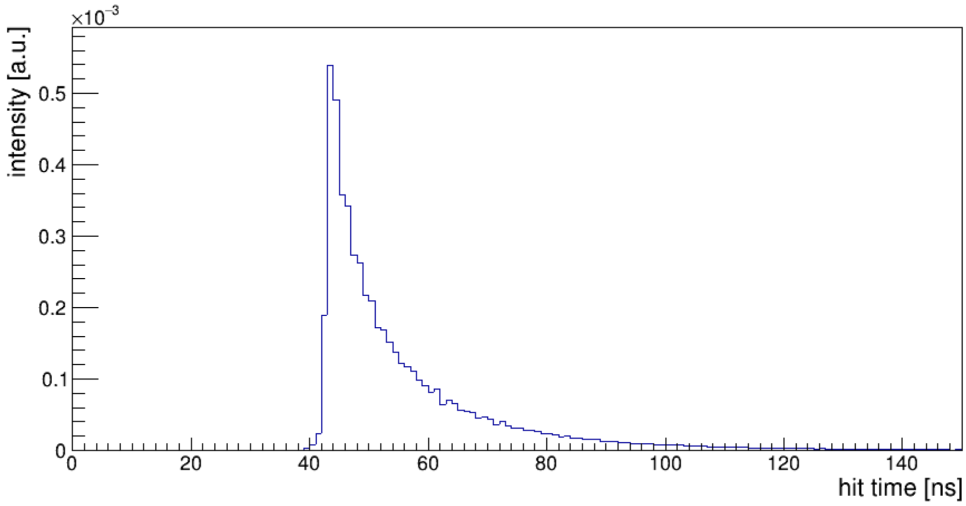

Figure 5.9: Example of a tof spectrum for scattered and re-emitted light. The origin of the original photon was assumed to be in 800 cm distance and an angle of 17° to the PMT.

(a).

The top plot in Figure 5.10 shows the number of detected photons in the detector as obtained from the `offline` simulation as a function of detector radius r. The solid red line represents the total photon number, whereas the solid blue line takes into account only unattenuated photons. These make out around one third of the detected light. The exact fraction is depicted as a function of detector radius in the bottom plot. The amount of visible light rises towards the outer detector regions. A peak is visible around $r = 16\,\mathrm{m}$. Very close to the edge, the light yield drops again due to the occurrence of total reflection. This behaviour can be reproduced with the probability LUTs when calculating the local detection efficiency like it was done for Equation (5.6) for positions along r. The corresponding curves are depicted by dashed lines. A comparison shows that the peak positions coincide. The LUT slope in the unattenuated case is slightly too weak, hinting on an underestimation of the attenuation length. The attenuated curves are very similar to each other except for the falling part near the edge. A reason might be reflection and multiple scattering, none of which was taken into account for the LUTs.

5.2.5 Crystallisation

At energies of only a few MeV, the reconstruction result is barely more than a diffuse cloud around the vertex. Nevertheless, the cloud structure can carry topological information. As an attempt to tease out certain tendencies, a process called crystallisation was implemented. It intervenes in the very last iteration. As usual, a probability density

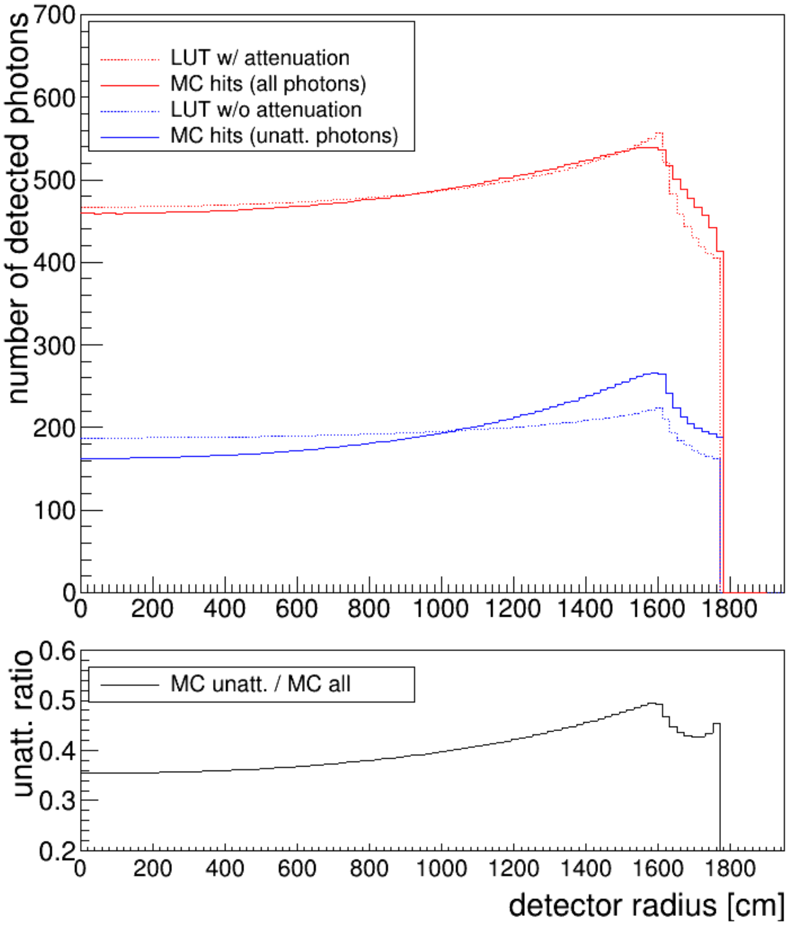

Figure 5.10: Top: Simulated number of detected photons as a function of detector radius in JUNO compared to the local detection efficiency obtained from LUTs. Bottom: Ratio between unattenuated and total light yield as a function of detector radius.

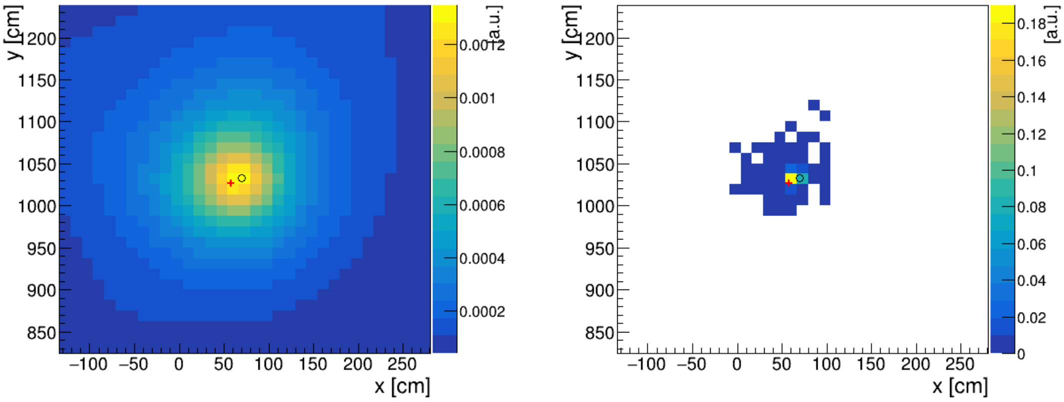

(a) TR using the scattered-light algorithm. The contrast is highly increased in comparison to a regular TR of the same event, depicted in Figure 6.3 (a).

(b) TR using the crystallisation algorithm was used in the last iteration. The scattered-light algorithm was not used here.

Figure 5.11: Depiction of two different reconstruction strategies used on the same 3 MeV electron event in JUNO. A red plus marks the true event position. A fine circle marks the reconstructed vertex which was used as reference point.

distribution is calculated for each hit on the basis of the previous result, but instead of adding up the whole distribution to the final mesh, only in the cell where the distribution has its maximum its value is incremented by 1.

The result is a very granular picture as can be seen in Figure 5.11 (b). The TR of a 3 MeV event was, after going through nine regular iterations with the result depicted in Figure 6.3 (a), finalised with a tenth iteration in which the crystallisation algorithm was applied. Although the scattered-light algorithm was not used, the effect of scattered light is being very much reduced.

Crystallisation can be activated in the configuration files.

5.2.6 Spherical Region of Interest

In its basic configuration, the TR is able to reconstruct an event topology in the detector without making any assumptions on the type of event. Nevertheless, it can sometimes be reasonable to limit the generality on the basis of external information. From the perspective of reconstruction speed it is highly desirable to reduce the mesh volume to a spatial region of interest. In case of high energy muons, where external triggers and fast algorithms can reveal a lot about the approximate track, a cylindrical volume measuring a few metres in radius around the assumed track can be selected as spatial region of interest [120]. A similar solution was implemented for low energy events, where a spherical region of a few metres in radius around the reconstructed vertex is sufficient to enclose the complete region of energy deposition.

Technically, this can be realised by changing the initial probability mask. This mask is binary and usually contains zero entries everywhere except for the active detector volume. The zone with non-zero entries can be confined to any desired sub-volume. This treatment would be sufficient in an ideal medium where no light attenuation takes place. As soon as attenuation effects delay a ratio of photons, it happens that their treatment as direct light suggest an origin beyond the confined region. However, the normalisation requires the photon to come from inside the volume and thus forces the corresponding hit to contribute fully to the probability density – which is typically reflected in the edge region. In that way, the totality of scattered and re-emitted photons lead to artefacts on the edge of the confined volume. Although these spots can easily be identified by means of their location they can strongly distort the reconstruction result in the course of further iterations.

Another change in the initial probability mask remedies the problem: By creating a transition zone in the outermost region of the confined volume, where the bin content is shaped like a fast decrease in the outward direction instead of a prompt cut-off, the impact of the allocated photons is defused. Again due to normalisation, their contribution is not suppressed totally, but rather spread over a wider range and thus less intrusive.

The spherical binary mask can be selected and scaled via the configuration files.

Chapter 6

Event Discrimination

Many sorts of events in a LSc detector trigger signals, much of which are unwanted. While some background can be avoided quite simple by applying fiducial volume cuts, spatial vetoes, or coincidence criteria, the correct identification of the remaining signals demands for more complex methods.

Pulse shape discrimination (PSD) is a generic term which subsumes a variety of approaches to classify events on the basis of hit patterns in a detector. Different signatures can arise e.g. from the particular ratios of the fast and slow scintillation components that appear for different particle types, or from differences in the event topology. Common methods include a tail-to-total evaluation where the tail integral of the pulse is compared to its total integral, or a Gatti analysis [123], where the pulse is compared binwise to averaged sample pulses for two different particle hypotheses. However, both methods are ineffective when the pulse shapes are not distinct enough, as it is the case for electrons, positrons, and gammas. Borexino was able to statistically identify at least a fraction of the positron events by making use of ortho-positronium formation [124, 20, 125]: This bound state with an electron is build for about 50 % of all positrons and leads to a delay of the subsequent annihilation according to its lifetime in LSc of $\sim 3\,\mathrm{ns}$. Also for JUNO this option has been studied [126].

JUNO will have an exceptionally high photoelectron yield which opens the possibility to make use of a small scale difference in topology. An MeV electron deposits energy in the detector mainly by ionisation within a couple of cm, whereas a positron additionally annihilates with an electron, producing two 511 keV gammas. The gammas undergo several processes of Compton scattering, leading to an energy deposition tens of cm away from the positron vertex (see Section 2.1). Although the effect on the pulse shape is hardly noticeable, an advanced analysis after reconstructing the events with the TR method can actually reveal distinct features, as will be demonstrated here.

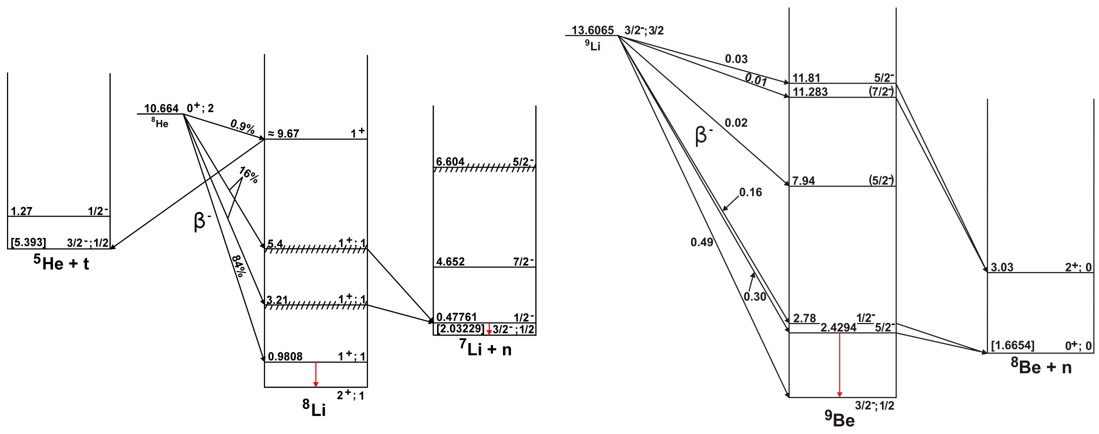

(a) (b)

Figure 6.1: Decay schemes for ^{8}He (a) and ^{9}Li (b). Energy levels are given relative to the ground state of $_{8}$Li and $_{9}$Be, respectively. Taken from [127].

In this chapter, the potential for a discrimination of both electron from positron and electron from gamma events is analysed for a JUNO-type detector. Section 6.1 points out the scientific potential that lies in the event discrimination. Section 6.2 explains the methods which were developed in the course of this work and used on the data samples described in Section 6.3. The results are presented and discussed in Sections 6.4 and 6.5.

6.1 Motivation

6.1.1 ^{8}He and ^{9}Li

Cosmic muons that interact with the ^{12}C contained in the target molecules of the LSc produce a whole bunch of different spallation isotopes, some of which have serious consequences on neutrino measurements. Particular significance attaches to ^{8}He and ^{9}Li. Their decay schemes are depicted in Figure 6.1. Both isotopes feature, apart from the pure β^- decay, a decay channel in which the β^- emission goes along with the release of a neutron. The overall ratios of these (β, n) channels are 16 % and 50.8 %, respectively [97]. Without the possibility to tell e^+ from e^- events, the signature is undistinguishable from that of inverse beta decay $\bar{\nu}_e + p \rightarrow e^+ + n$ and would thus affect the measurement of the mass ordering (see Section 3.2.1).

The current strategy foresees a temporal muon veto. Due to long half-lives of 119 ms and 178 ms, respectively [97], the veto has to be kept upright for more than a second, thus losing a considerably high amount of exposure.

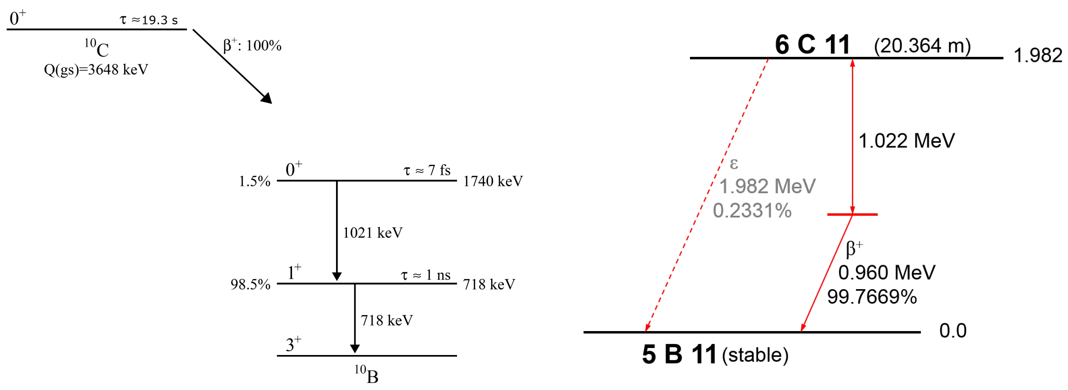

(a) Adapted from [130].

(b) Taken from [131].

Figure 6.2: Decay schemes for ^{10}C (a) and ^{11}C (b). Energy levels are given relative to the ground state of ^{10}B and ^{11}B, respectively.

An e^+/e^- discrimination would ideally render the veto unnecessary, provided that the cut is very clean. But even a softer discrimination would help a great deal in measuring the production rates of both ^{8}He and ^{9}Li. The combination of measurements in KamLAND, Borexino, Daya Bay and Double Chooz predicts a ^{9}Li yield of $(19.96 \pm 1.21) \times 10^{-8} \mu^{-1}\mathrm{g}^{-1}\mathrm{cm}^2$ for an estimated mean muon energy of 215 GeV in JUNO [128]. For ^{8}He the data suggests a yield of roughly a factor 2 less.

6.1.2 ^{10}C and ^{11}C

The β^+ emitters ^{10}C and ^{11}C are also products of cosmic muon spallation. The decay schemes are depicted in Figure 6.2. Both isotopes are serious background sources for solar neutrino signals. JUNO's measurement of ^{8}B neutrinos in the MSW transition region around 3 MeV depends highly on the reduction of ^{10}C background, as can be concluded from Figure 3.6 (see Section 3.2.3). In Borexino, residual ^{11}C is the main background for the direct measurement of CNO and pep neutrinos at energies above 1 MeV [129]. But also the $0\nu\beta\beta$ experiment KamLAND-Zen has to deal with cosmogenics, since in particular residual ^{10}C is dominating the region of interest around the expected $0\nu\beta^-\beta^-$ peak of ^{136}Xe even after applying all cuts [130, 65]. A reduction of ^{10}C would also have an appreciable effect for the detection of ^{8}B neutrinos, whose energy spectrum in JUNO is superimposed with the β^- spectrum from ^{210}Bi. Its rate and spectral shape must therefore be known very precisely. However, the ^{210}Bi spectrum overlaps with the ^{10}C spectrum as can be seen in Figure 3.5.

However, the long lifetimes of 19.3 s and 20.4 min, respectively [97], make an according muon veto rather pointless. Instead, Borexino and KamLAND-Zen so far rely on temporal and spatial correlations based on μ-n-e^+ threefold coincidences when, as in over 90 % of all cases, the spallation process is accompanied by a single neutron [65].

An efficient discrimination between cosmogenic β^+ events and e^- signal events – the latter including the neutral current e^- interactions from solar neutrinos – would mean a significant step forward in the searches mentioned here. Furthermore, the identification of ^{10}C and ^{11}C, even on a statistical basis, would help to further shape current models of spallation processes due to cosmic muons.

6.1.3 Natural Radioactivity

Gammas from natural radioactivity are usually not considered to be dangerous background in JUNO. For IBD signals, they can very effectively be removed by coincidence criteria (see Table 3.3). The solar studies build on the facts that the requirement for intrinsic LSc contamination on the one hand is low enough and the external background due to material surrounding the LSc target on the other hand can be avoided by applying a fiducial volume (FV) cut. Therefore, the backgrounds depicted in Figure 3.5 neglect external gammas. Most often these come from ^{208}Tl (2.6 MeV), and at lower rates also ^{40}K (1.5 MeV) and ^{214}Bi (0.6 MeV, 1.1 MeV, and 1.8 MeV) [132]. Further gammas with energies of 6 MeV and 8 MeV are expected from (n, γ) reactions, e.g. n-captures in the stainless steel frame [1].

However, the depth of the FV cut has to be as high as 5 m in order to become clean enough. A reliable e^-/γ discrimination could thus more than double the JUNO FV for solar neutrino analyses. Furthermore, the discrimination could be used for measuring the modelled external gamma background und would be a valuable tool for cross-checks.

6.2 Methods

When the TR is used on an MeV event, the resulting probability density distribution typically resembles a diffuse cloud around the reference point. An example is shown in Figure 6.3 (a). Here, a 3 MeV electron was reconstructed with 9 iterations and a final binning of 12.5 cm. The true event vertex is marked with a red plus. The small circle indicates the position of the reconstructed vertex which was used as reference point. The amount of unscattered PMT hits and the uncertainty of the hit times is simply not sufficient to resolve single tracks of the involved particles.

But still the cloud shows sensitivity on the actual event topology. While the hit times of unscattered scintillation photons from an electron event fit well to emission points very close to the reference point, the emissions caused by gammas in a positron or

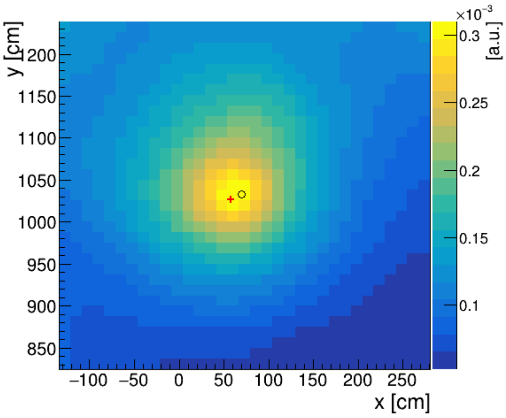

(a) Two-dimensional projection of the result in the XY-plane.

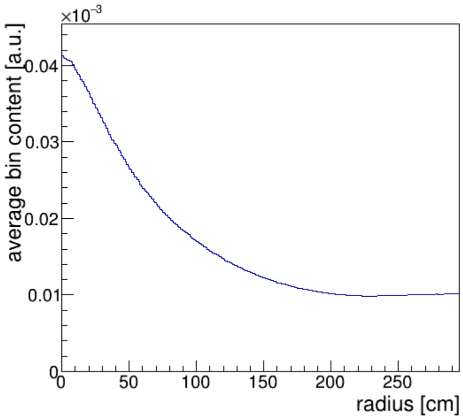

(b) Radial event profile averaged over all directions. The maximum voxel was chosen as the centre.

Figure 6.3: Example for an MeV event in the TR. The displayed event is a 3 MeV electron.

pure gamma event do not correlate that well with the energy deposition at the reference point, so that the probability distribution becomes more diffuse. In very opportune cases the reconstruction result should even show asymmetric features when gammas are involved.

These features are not easy to spot. Two strategies for discrimination will be presented in this section. The first one is a classic approach: Here, it is necessary to develop applicable parameters and criteria for a discrimination. Afterwards, a machine learning approach will be described since, as a typical classification task, the event discrimination can also be performed by a neural network.

6.2.1 Single Parameter Cut

In the following a series of parameters will be introduced by the help of which more point-like events can be discriminated from those featuring a less compact energy deposition.

Spread The reconstruction result of a LE event is expected to exhibit a dense central region around the reference point, outward from which the probability density gradually decreases. This can be observed in Figure 6.3 (b), which represents the radial event profile. Coming from the voxel with the maximum content, the average content from a number of voxels in random directions is build for radii r around the maximum voxel. The spread can be measured by determining the radius R_t at which the profile has fallen below a predefined threshold $t \in [0,1]$ relative to the maximum at $r = 0$. $R_t = 0.5$ was used in the later analyses as a result of empirical testing.

Profile Gradient Assuming the average event profile $P(r)$ to follow a smooth curve, its decrease is likely to feature steeper regions for more point-like events. Therefore, the derivative of the profile is built. In order to be stable against small fluctuations, it is useful to build a moving average over a certain distance. For the evaluation on a binned structure this means that the derivative P'_j at bin j is defined as

$$P'_j = \frac{P_{j+d} - P_j}{d+1}, \tag{6.1}$$

where the integer d sets the number of bins in the window over which is averaged. If not stated otherwise, bins of 1 ns in size will be used and d is set to 25.

Contrast The contrast of the reconstruction result is another handle for discrimination. Here, contrast C is defined as the sum of the n highest bin contents over the integral over all remaining bins. It is usually reasonable to choose $n > 1$ since the cell size of the reconstruction grid is not necessarily small against the dimensions of the probability cloud, and thus the exact position of the grid can affect the content of the maximum voxel. If not stated otherwise, $n = 8$ was used later on.

6.2.2 Machine Learning

Machine learning (ML) is a subdomain of artificial intelligence that receives increasing attention in all fields of data analysis, not least in particle physics. The idea is to feed data samples to an algorithm which thereby develops a predictive model. Hence, the algorithm learns to evaluate unknown data. Useful applications include classification and regression tasks. The procedure in these cases would be supervised learning, i.e. the algorithm is presented with labelled datasets. The learning itself is an iterative process which continuously optimises itself through variations within a set of floating parameters. Throughout the epochs of the iterative process the quality of the parameter configuration is measured with the help of a so-called loss function which basically sums up all differences between predictions and true characteristics. A minimised loss function is intended by applying e.g. the gradient descent method which means to individually tune the parameters in the direction of reduced loss for a defined data sample (training). In order to get an independent measure of the predictive power, the loss function is likewise calculated for a separate data sample (testing).

A wide range of literature on ML and neural networks (NN) is available. A general introduction to the subject can be found e.g. in [133]. For a more physics related consolidation see [134].

The JUNO collaboration is currently exploring the potential of ML techniques towards the reconstruction of vertex and energy and also event classification. In this work, a convolutional neural network (CNN) was established in order to classify events by means of their topological reconstruction. Before the network architecture is explained below, a general introduction to CNNs is given alongside with a selection of related basic terms.

Convolutional Neural Networks

NNs are a linkage of a large number of functional basic units, in analogy to the human brain called neurons. These nodes are hierarchically arranged in layers, as schematically demonstrated in Figure 6.4 (a). The input data is translated into numbers, each of which is passed to a neuron in the input layer. What follows is an arbitrary number of hidden layers, whose neurons are always fed with the output of neurons from the previous layer. The neurons themselves carry out two operations, as being illustrated by Figure 6.4 (b). The first one is a linear combination of the n input numbers x_1 to x_n, induced by weights w_1 to w_n and biases b_1 to b_n. These weights and biases are what the NN optimises throughout the training phase. In the second step, called activation, a non-linear function is applied, e.g. the rectified linear unit (ReLU) function defined as the maximum of 0 and its argument. Introducing non-linearity constitutes a key operation, since it prevents redundancies in a multi-layer architecture. An output layer stands at the end of a NN. In the case of a classification task, the output layer would typically have as many nodes as there were classes defined, and each would contain a number that can be interpreted as a probability for the input data to belong to that class.

In a convolutional neural network (CNN), schematically illustrated by Figure 6.5, the NN concept is extended by the application of convolutional filters. The input data can be considered as a pixelated image, whose pixel intensities were translated into numbers. Filters are matrices much smaller in size than the image itself. After being randomly initialised, the network optimises the matrix entries during training. By shoving the filter over the image, a convolution is carried out, the result of which is represented by a new map of numbers which subsequently undergo activation. The procedure can be repeated with the resulting map and a new set of filters, thus connecting potentially detected features. As an option, the layer size can be reduced between two convolutional layers. Several adjacent pixels are being condensed to one following a predefined rule.

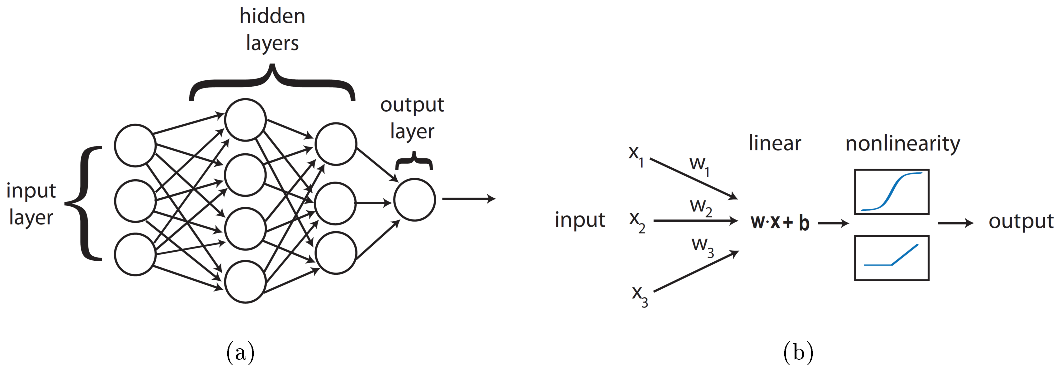

Figure 6.4: Schematic demonstration of a neural network. (a) shows the arrangement of neurons in different layers while (b) illustrates the functionality of a single neuron. Taken from [134].

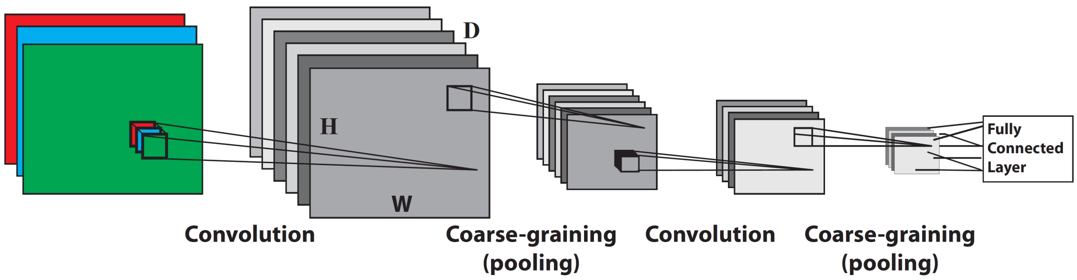

Figure 6.5: Schematic representation of a convolutional neural network. Taken from [134].

This process, visualised in Figure 6.5, is called pooling. In that way, further off spots in the image can be related later on. While the filtering in the top layers can still be understood as the search for visible image features, the filter representations become more abstract in deeper layers. Fully connected (also: dense) layers complete the CNN.

Quality Estimators

Good measures need to be found in order to evaluate the performance of a NN with regard to event discrimination. Here it helps to introduce the expressions *true positive* (TP) and *true negative* (TN), which represent the numbers of correctly predicted signal and background events, respectively. Accordingly, the terms *false negative* (FN) and *false positive* (FP) denote the numbers of incorrect predictions for signal and background, respectively.

A very general but vivid quality estimator is the accuracy α, being defined as the number of true predictions divided by the total number of predictions:

$$\alpha = \frac{\mathrm{TP} + \mathrm{TN}}{\mathrm{TP} + \mathrm{TN} + \mathrm{FP} + \mathrm{FN}}. \tag{6.2}$$

However, the accuracy depends on the ratio of signal to background samples. Since the training sets do not necessarily have to be equally large, the parameter needs to be handled with care. In this work, the training sets were balanced, so that 50 % accuracy can be interpreted as a completely non-predictive network, while a perfect discrimination would be reflected by a score of 100 %.

It has to be noted that the acceptance value for a signal event also influences the accuracy parameter. In case of a binary classification (signal or background), it seems rather intuitive to declare events that were assigned with a signal probability higher than 50 % as such. However it might occasionally be reasonable to raise the acceptance value in favour of cleaner signal samples. In order to provide a more sophisticated look on the NN performance, the receiver operating characteristic (ROC) can be used. The ROC is a graph plotting the signal efficiency, i.e. the true positive rate

$$\mathrm{TPR} = \frac{\mathrm{TP}}{\mathrm{TP} + \mathrm{FN}} \tag{6.3}$$

over the impurity of the selected signal sample, i.e. the false positive rate

$$\mathrm{FPR} = \frac{\mathrm{FP}}{\mathrm{FP} + \mathrm{TN}}. \tag{6.4}$$

A common parameter for the comparison of different ROC curves is their integral, the area under curve (AUC). In the case of a completely non-predictive NNs, TPR and FPR would be equal no matter what acceptance was chosen, so that the ROC curve would resemble a straight line from the origin with slope 1 and AUC = 0.5. A highly predictive NN on the other hand would lead to a fast rise of the curve and an accordingly higher AUC, with AUC = 1.0 at most. Examples for ROC curves are shown in Figure 6.17.

Network Architecture

Image classification is a typical CNN application. Architecture and especially the choice of hyperparameters are decisive factors for the success of a network and need to be adapted to the problem it is supposed to solve. Hyperparameters of a CNN include the number and size of, hidden layers, filters, and also pooling regions. Although guidelines exist for designing CNNs – e.g. filters should have a reasonable size in order to cover and identify certain image features – finding the optimal network to a problem eventually includes heuristic work.

Three strategies were developed and will be described in the following. The CNN implementation was based on TensorFlow libraries [135] utilising the Keras interface [136].

1D-CNN The first approach uses a one-dimensional CNN with the standard structure of several convolutional and pooling layers followed by two dense layers. The exact layering is visualised in Figure 6.6 (a). The input data is the profile of the TR result of an event, described in Section 6.2.1, spread over 300 bins. The convolutional part of the network involves three convolutional and two pooling layers. The transition to the fully connected part requires flattening, meaning that the node matrix is rearranged to become a one-dimensional vector of neurons – a description being actually more illustrative at more dimensions. Batch normalisation is an operation which shifts and scales the output values of the previous layer in order for the input values of the following layer to be centred around 0 with a fixed variance. This stabilises the activation process and prevents that the layer parameters have to be relearned if the previous output changes. The final dense layer reduces the output size to two neurons according to the binary classification task, representing the affiliation to each of the classes. All convolutional and dense layers are activated by means of the ReLU function except for the final dense layer. Here, the Softmax function is applied which makes sure that the outputs add up to 1.

3D-CNN The second approach foregoes preprocessing the TR result and directly feeds the content of the resulting 3D histogram to a CNN, which hence needs to be three-dimensional. Its structure is shown in Figure 6.5 (b). Due to the higher dimensionality, the number of nodes strongly expands by the cost of memory and runtime. Therefore, the input data was reduced to 17 bins in x, y, and z direction, at 12.5 cm binning covering a detector volume of roughly $8\,\mathrm{m}^3$ around the event vertex. Furthermore, the number of convolutional layers was reduced to two and no pooling layer was included. The fully connected part on the other hand was completely retained from the 1D-CNN.

3 channel 3D-CNN The third approach is structurally very similar to the second one. But while then the input data was the raw and unbiased output from the TR, the idea is here to include the physically motivated expectation and feed the gradient field of the TR result to the network. Since the TR result can be differentiated with respect to three room directions, the outcome comprises three 3D matrices rather than one. Technically, CNNs provide the opportunity to process data with more than one channel. In this way a colour image can be broken down into its red, green, and blue component before being fed to a CNN. The network then convolves the three channels separately, bringing together

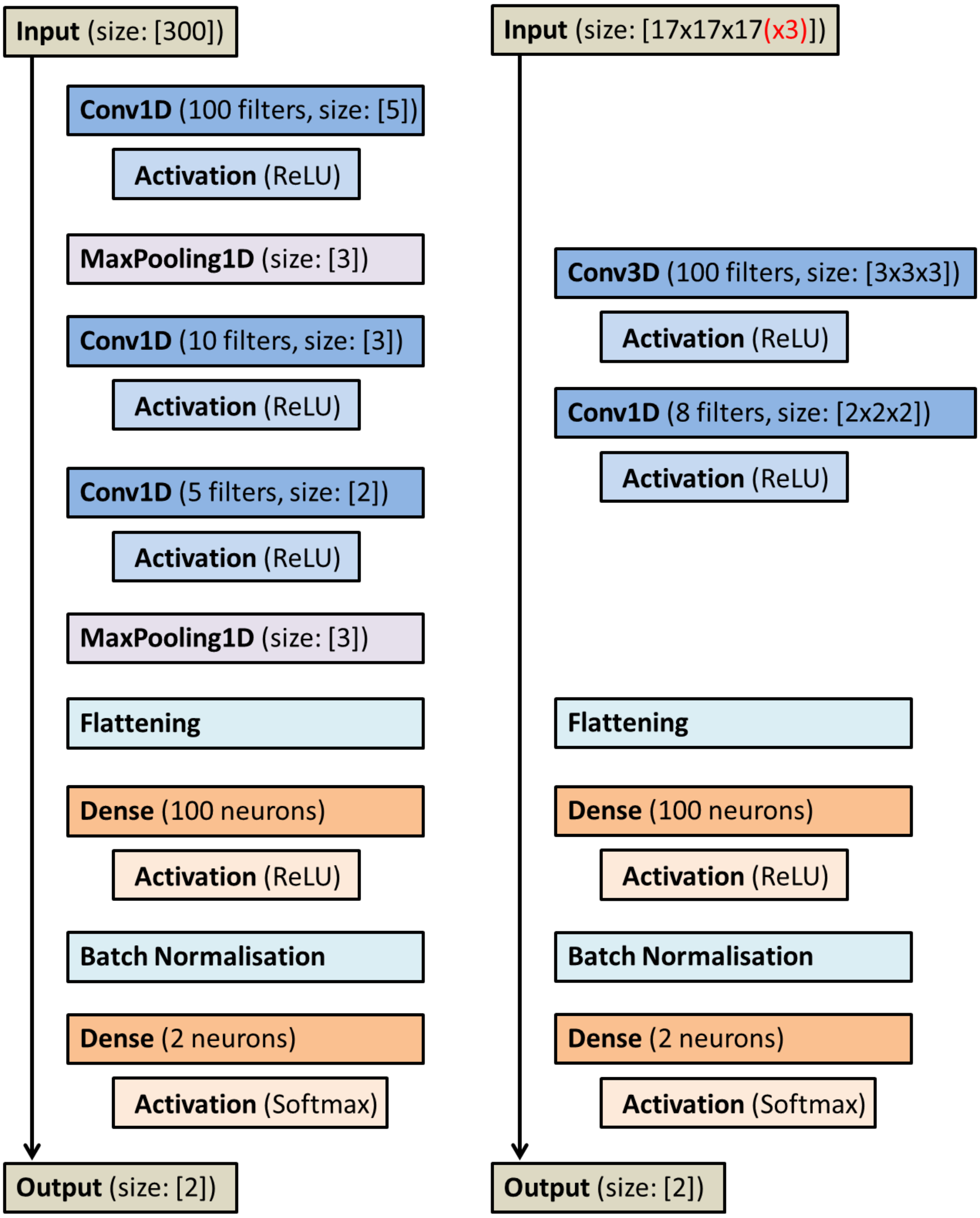

(a) 1D CNN (b) 3D CNN

Figure 6.6: Schematic representation of the CNN architecture used for event discrimination.

the information in the dense layers. Analogously, the already established 3D-CNN could be presented with the three differentiated maps.

6.3 Datasets

The datasets used in the Sections 6.4.1 and 6.4.2 were provided by Y. Xu [137]. They were created with the JUNO `offline` software described in Chapter 4.

120, 000 events were simulated each for electrons and positrons in order to test the e^+/e^- discrimination. The start positions were distributed uniformly over the detector volume. The minimum visible energy for an e^+ event is 1 MeV due to the annihilation energy. The visible energies of the simulated events are uniformly distributed between 1 MeV to 10 MeV and thus cover the range of the e^+ spectrum expected from the reactor $\bar{\nu}_e$. Positronium formation [3] was considered for 54.5 % of the e^+ events with an effective decay time $\tau = 3.08$ ns.

120, 000 events were also simulated each for electrons and gammas in order to test the e^-/γ discrimination. The visible energies are uniformly distributed between 0 MeV and 3 MeV in order to cover the gamma spectrum from natural radioactivity.

Larger samples were needed for the ML analysis in Section 6.5. Therefore, additional simulations were run with software and configurations identical to the simulations previously mentioned. This includes also the data used for ^{10}C analysis in Section 6.4.3. 10^4 events were simulated each for the categories electron, positron, gamma, and ^{10}C, where the delayed gamma emission was considered in the latter case. For the sake of comparability all events were limited to a detector region with radii $9.5\,\mathrm{m} < r < 10.5\,\mathrm{m}$. Kinetic energies were limited to (2.75 ± 0.25) MeV for electrons and gammas and (1.75 ± 0.25) MeV for positrons. The positrons in the ^{10}C events were given uniformly distributed kinetic energies up to the endpoint of the β decay spectrum at 1.9 MeV (see Figure 6.2 (a)). From all four categories only those events were selected which featured hit counts between 3200 and 3800. This left 8045 electron, 7950 positron, 6703 gamma, and 4869 ^{10}C events. Their distribution within the energy interval is uniform.

The data was analysed in three stages:

- Directly after the pure detector simulation stage. The exact PMT hit times are used for reconstruction. These datasets are thought to study the performance of the discrimination methods under ideal conditions in order to estimate its limitation. They will be referred to as **detsim**.

- After smearing the hit times of the *detsim* data according to the TTS values used in the electronics simulation. Offsets on the hit times considering cables and readout electronics are not added. Although these offsets enter the electronics simulation in the official `offline` package, it was decided to not use them here since it is expected that their contribution can be subtracted with calibration to below 1 ns. The datasets will be called **elec w/o noise** later on.

- After adding dark noise to each channel. This is done by the help of the electronics simulation. The datasets will be labelled **elec w/ noise**.

A reference point in space and time has to be found in order to apply the TR on an event. In case of the idealised *detsim* data it would not be justified to use the true start point of the particle since it does not exactly correspond to the actual energy deposition for gamma events. Therefore, the centre of energy deposition was extracted from the Monte Carlo truth and used in combination with the true start time. For the *elec w/o noise* and *elec w/ noise* data the vertex reconstruction implemented inherently in the TR (see Section 5.2.2) was used. Only the Hamamatsu PMTs were used for vertex reconstruction as it was found that the bad time resolution of NNVT PMTs obstructs the fit.

The TR itself was, if not stated otherwise, applied with the following configuration: 10 iterations I_0 - I_9 were carried out. I_0 and I_1 featured a very coarse binning of 2 m and 1 m, respectively, in order to confine the region of interest very fast. I_2 - I_9 were computed on a grid with the final 12.5 cm binning. The detector mesh was reduced from the beginning to a spherical region of interest around the reconstructed vertex with a radius of 3.5 m. The probability mask was reset to values of 0 and 1 after every mesh refinement. The TR made use of all large PMTs. The small PMTs were excluded from reconstruction since their relatively small contribution to the number of hits comes with a high cost in computation time. In order to speed up the reconstruction it was carried out in the *detected light* rather than the *emitted light* mode. The difference was explained in Section 5.1.1. The effect of local variation in photoelectron yield was found to be small within the investigated topologies.

6.4 Results from Classic Methods

The reconstructed events have been used as a basis for event discrimination. This section presents the results under use of single parameter cuts.

Each reconstructed event was processed and assigned with the set of parameters described earlier. The parameters were analysed in turn. A signal efficiency ε was set to a fixed value. Depending on the presumption whether signal or background should tend to populate the parameter axis at higher values, the cut value was defined at the axis

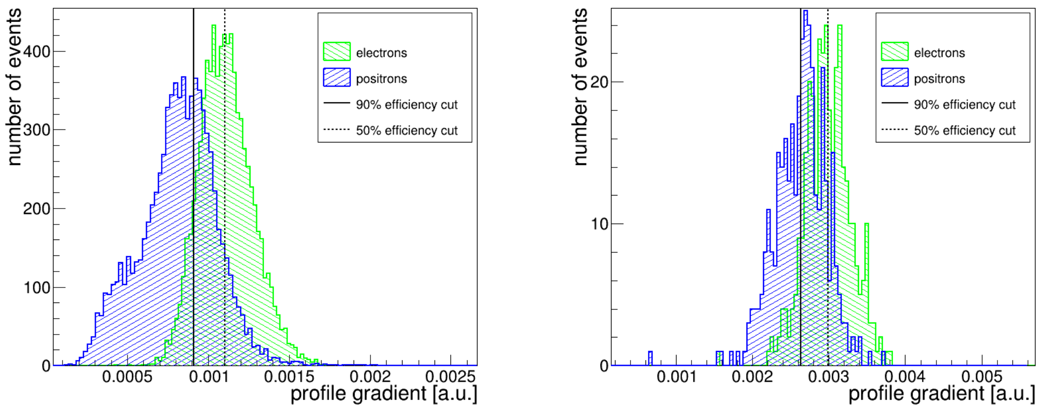

(a) $2.5\,\mathrm{MeV} < E_{\mathrm{vis}} < 3.0\,\mathrm{MeV}$

(b) $8.5\,\mathrm{MeV} < E_{\mathrm{vis}} < 9.0\,\mathrm{MeV}$

Figure 6.7: Distribution of the *profile gradient* parameter in the e^-/e^+ discrimination at the *elec w/ noise* stage. The detector radius was constrained to $9.5\,\mathrm{m} < r < 10.5\,\mathrm{m}$.

position where the integrated signal distribution normalised by its full integral reached ε or $(1-\varepsilon)$, respectively. The remaining background contamination is quantified with the cut impurity κ, defined as the relative amount of background events in the signal region. Efficiency and impurity are analogous to the concepts of true and false positive rate introduced by Equations (6.3) and (6.4).

The uncertainties on κ were calculated via

$$\sigma_\kappa = \frac{\sqrt{\mathrm{FP}}}{\mathrm{FP}+\mathrm{TN}}, \tag{6.5}$$

where FP and TN denote the numbers of wrongly and correctly assigned background signals, respectively.

6.4.1 Electron/Positron

Exemplary distributions of the signal and background parameter are depicted in Figure 6.7 (a). The *profile gradient* parameter is plotted for visible energies $2.5\,\mathrm{MeV} < E_{\mathrm{vis}} < 3.0\,\mathrm{MeV}$, considering only events with detector radius $9.5\,\mathrm{m} < r < 10.5\,\mathrm{m}$. A green and a blue population represent electrons and positrons, respectively. It can clearly be seen how the distributions peak at distinct positions, although they show an overlap. The tendency of the formation ordering matches the hypothesis of electron reconstructions leading to sharper images. A solid (dashed) black line marks the cut value which would result from a required electron efficiency of 90 % (50 %).

It is further expected that the discrimination potential wears out towards higher energies. This can be observed in Figure 6.7 (b), showing the same plot for $8.5\,\mathrm{MeV} < E_{\mathrm{vis}} < 9.0\,\mathrm{MeV}$. Here, the overlap is significantly larger. The relative amount of scintillation photons due to the two 511 keV gammas becomes smaller at higher total energies. Their contribution to the TR result is outshone by the central energy deposition from ionisation. Furthermore, bremsstrahlung gammas occur more often. These would spoil the distinguishing feature of positron events.

The distributions for positrons are broader than for electrons due to the formation of positronium. The delayed annihilation in the event fraction building ortho-positronium causes an additional blurring effect in the TR. This is visible especially at the left-hand tail of the positron distribution in Figure 6.7 (a).

Impact of the Data Quality The top plots in Figure 6.8 show the achieved impurity results at the data stages *detsim* (black), *elec w/o noise* (red), and *elec w/ noise* (green) plotted over visible energy for the parameters *spread* (a), *profile gradient* (b), and *contrast* (c). Only events at a detector radius $9.5\,\mathrm{m} < r < 10.5\,\mathrm{m}$ were considered. Again, solid (dashed) lines mark $\varepsilon = 90\,\%$ ($\varepsilon = 50\,\%$). The results from the idealised *detsim* data behave similarly in all three methods. The minimum values are below 10 % and all lie below 4 MeV. From here, the impurity almost constantly rises towards 10 MeV, scoring impurities between 30 % and 40 % (around 10 %). The general decline to higher energies in the ability to discriminate can be explained with the fading relative contribution of the annihilation gammas to the total amount of emitted light. In the case of the *spread* and *contrast* parameter the impurities indicate a slight increase from the minimum around 3 MeV also towards lower energies. The more realistic datasets *elec w/o noise* and *elec w/ noise* replicate the trend of impurity increase towards high energies, whereas a minimum is hard to make out. One can at the utmost speak of a flattening below 4 MeV in the case of the *profile gradient* and *contrast* parameter. However, the impurities suffer a strong upwards shift by 20 % to 40 % (10 % to 20 %) compared to *detsim* data. Relative to each other, *elec w/o noise* and *elec w/ noise* do not vary strongly, though. The reasons for that will be studied further below.

The cut values for the discrimination are displayed in the bottom plots of Figure 6.8 with equal colour representation. Concerning the *spread* parameter it is interesting to see how the *detsim* values are hardly affected by the energy whilst *elec w/o noise* and *elec w/ noise* show a clear energy dependence. This indicates a relation to the resolution of vertex and time reconstruction, which entered the TR in those two cases and, as can be seen in Figure 5.4, worsens with increasing energy. Notably, cut values for *spread* and *contrast* in the *detsim* data rise and fall, respectively, from 3 MeV to 0 MeV. Both

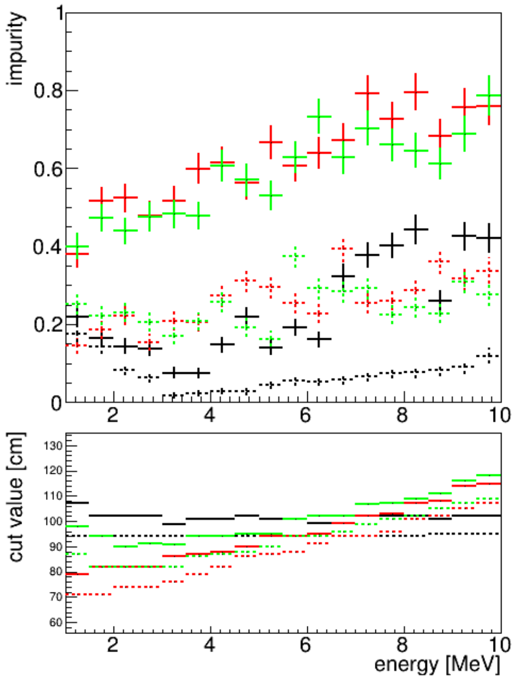

(a) *spread* parameter.

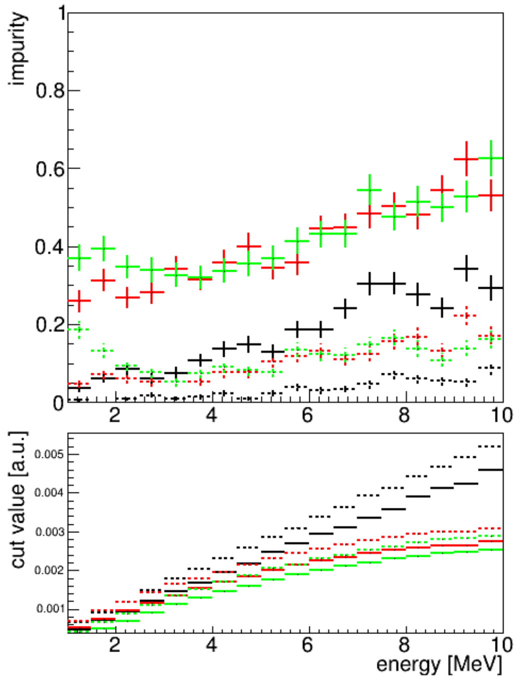

(b) *profile gradient* parameter.

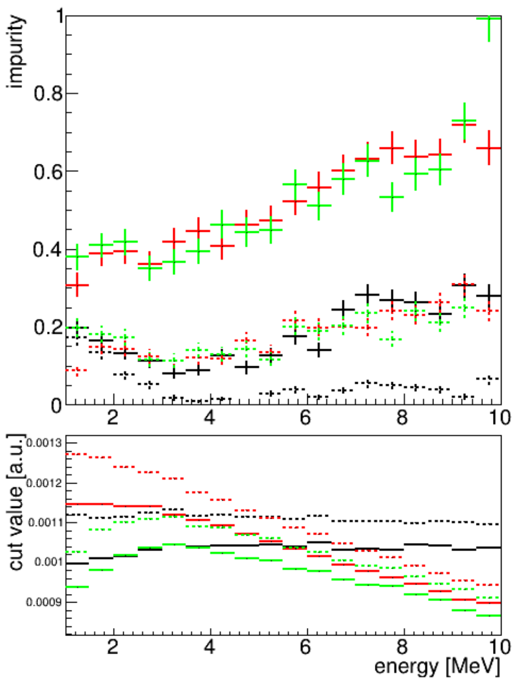

(c) *contrast* parameter.

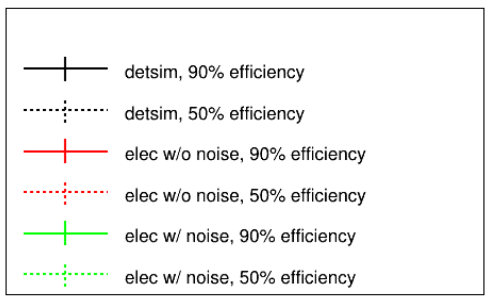

Figure 6.8: e^-/e^+ discrimination at different reconstruction stages for all three discrimination parameters. The impurity is given as a function of energy. Solid and dashed lines represent the results for efficiencies fixed to 0.9 and 0.5, respectively. Only events within a detector radius $9.5\,\mathrm{m} < r < 10.5\,\mathrm{m}$ were considered.

is symptomatic of less sharp TR images due to the statistical lack of information. The addition of noise amplifies this effect, as can be observed for the *elec w/ noise* data, as, similar to scattered photons, the uncorrelated hit times add a blur to the TR. An effect of this becomes visible in the *profile gradient* method, in which the only region where the impurity results for *elec w/o noise* significantly depart from *elec w/ noise* data is below 3 MeV. The dark noise rate of 20 kHz per channel adds up to an expected value of less than one dark hit per nanosecond in the whole central detector. In order to interfere with the reconstructed region of interest, the hit time would have to coincide in accordance with the channel position. The few tens of dark hits meeting this requirement are clearly outnumbered by the high JUNO photoelectron yield of 1,200 PE/MeV. That is why at higher energies the disturbing dark counts can be completely compensated for by higher direct photon statistics.

Impact of the Vertex Resolution It is striking how the *detsim* data in Figure 6.8 yields much lower impurities than realistic datasets. It was studied where this gap comes from. The *elec w/o noise* dataset was reconstructed under various configurations.

- *original vertex and time*: The center of charge deposition was used as reference point and the original start time as reference time.
- *smeared vertex*: A Gaussian smearing with $\sigma = 10$ cm was applied to each vertex coordinate while keeping the reference time untouched.
- *smeared time*: A constant shift of 1.5 ns was added to the original start time to be used as reference time while keeping the vertex unsmeared.

The resulting impurities for the *profile gradient* parameter at 90 % efficiency are, again depending on the energy, displayed in Figure 6.9. The *detsim* (black) and *elec w/o noise* (red) results from Figure 6.8 were also included for comparison. It can be deduced from the results of the *original vertex and time* configuration (magenta) how the pure TTS smearing has a considerable effect mainly at low energies, worsening the impurity with respect to the ideal *detsim* data by absolute 15 % up to 3 MeV. From there on, the difference is narrowed until the higher PE statistics completely compensate for TTS above 6 MeV. Almost no further deterioration is contributed from including the *smeared vertex* (dark blue). In contrast, the *smeared time* (cyan) renders the impurity values to lie about absolute 30 % above the corresponding ideal value and thus ranges, at least below 6 MeV, around the same level as the *elec w/o noise* data. For higher energies the *elec w/o noise* yields a little better results, most probably due to the fact that the offsets

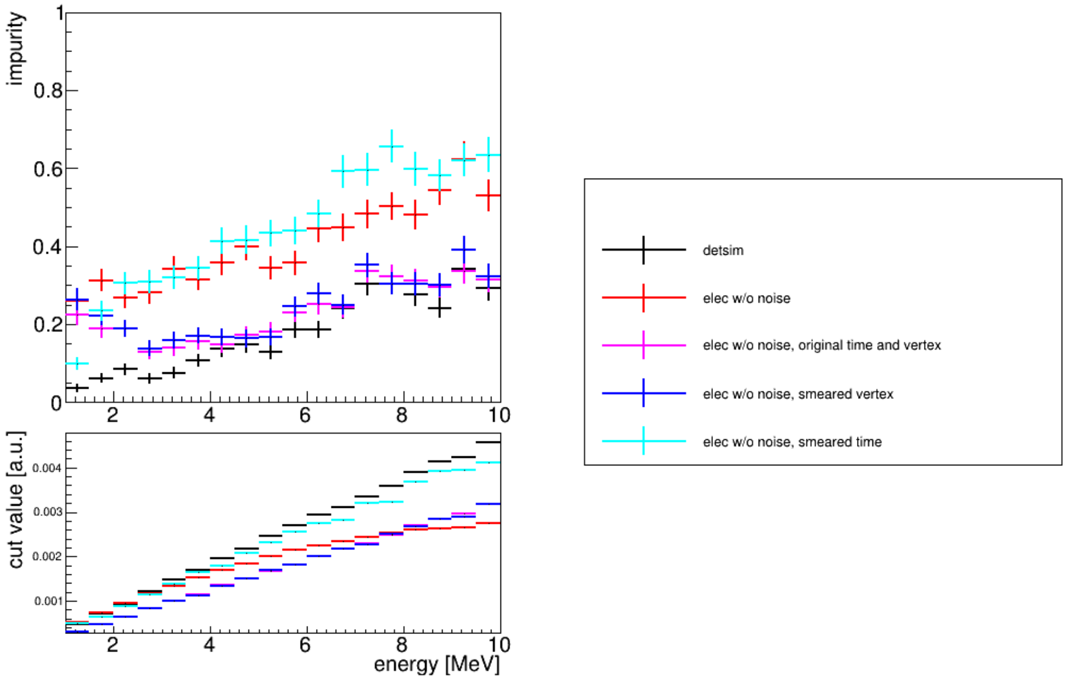

Figure 6.9: e^-/e^+ discrimination for different configurations of reference point and time. The impurity obtained from the *profile gradient* method at 90 % efficiency is given as a function of energy. Only events within a detector radius $9.5\,\mathrm{m} < r < 10.5\,\mathrm{m}$ were considered.

in time reconstruction are quite small here. The conclusion is that apart from TTS at low energies the time reconstruction is the largest issue in the discrimination performance.

The significance of time and vertex reconstruction was closer studied. The *profile gradient* parameter as obtained from the regular reconstruction of the *elec w/o noise* dataset was plotted over the resolution of the reconstructed reference point and time. In the depiction in Figure 6.10 (a) and (b), respectively, the parameters were corrected by their common cut level, drawn as a dashed line. The colours encoding the particle type were kept. While no obvious correlation can be seen between reconstruction quality and parameter value, the events lacking an accuracy in reference time clearly tend to produce parameter values that point to a more diffuse TR image. It can be concluded that the discrimination is not only sensitive to the compactness of energy deposition but also on the reconstructed reference time. The fact that in particular positrons are affected by a bad time reconstruction – the particle specific reconstruction quality is depicted in Figure 5.4 – is assumed to have a welcome effect on event discrimination.

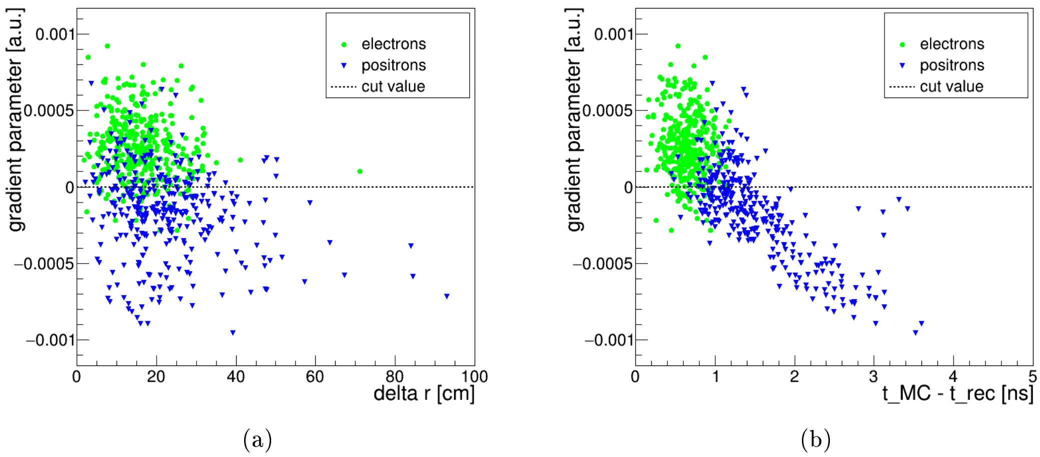

Figure 6.10: Impact of reference point and time on e^-/e^+ discrimination. The *profile gradient* parameter, corrected by the cut value, was plotted over resolution of the reference point (a) and reference time (b). Electron (positron) events are displayed in green (blue).

Impact of the Detector Radius So far the discrimination results were viewed depending on the visible energies while only events from a confined region were considered. Figure 6.11 shows impurities and cut values obtained at different detector radii r with the *elec w/ noise* dataset at 90 % efficiency. Two energy ranges were considered. The light green (dark green) line represents events with visible energies within $3 \pm 0.25\,\mathrm{MeV}$ ($8 \pm 0.25\,\mathrm{MeV}$). The plots for the parameters *spread* (a), *profile gradient* (b), and *contrast* (c) have in common that, regarding the discrimination performance, the detector falls into three regions:

- the central region up to $r \approx 2\,\mathrm{m}$, where all three methods show a very good performance with impurities below 20 % for the low energy samples, while the events with higher energies appear harder to distinguish. However, the divergence is not very significant due to poor statistics. The innermost datapoint should be totally neglected with regard to the small number of available simulated events.

- the bulk region between $r \approx 2\,\mathrm{m}$ and $r \approx 14\,\mathrm{m}$, where the impurities remain on a constant level. The cut values are consistent with the central region, which mildly suggests that the divergence in the central region might in fact be a statistical fluctuation. The rising cut values towards $r \approx 16\,\mathrm{m}$ reflect the likewise rising amount of unscattered photons (see also Figure 5.10).

- the outer region from $r \approx 14\,\mathrm{m}$ to the detector edge, in which the performance drops off promptly, manifesting itself in very high impurities. When having a closer look at selected events it becomes apparent that the probability distributions in the TR results are pulled towards the detector edge in this region as a consequence of the hit normalisation. Furthermore, the edge, beyond which no probability density is allowed in the TR, represents a sharp boundary, resulting in a hard cut-off in the event profile. Some TR results show signs of a malfunctioning mesh refinement, featuring reference points outside the final mesh volume.

Correlation between Parameters The plane formed by two parameters can provide valuable information with regard to a potential combined cut. The scatter plots displayed in Figure 6.12 represent the three pairings which arise from the discussed set of discrimination parameters. They all exhibit the general tendency according to which a value for parameter A which hints on either a signal or background event does so also in case of parameter B. A second observation is that electron points, depicted in green, seem to stick to this principle more strictly than positron points, depicted in blue, which scatter more widely. This leads to the third observation that handfuls of outliers – exclusively positrons – cluster within distinct regions. Some of these clusters can be explained by a failed TR in the sense that the TR result does not, for instance due to a bad reference time, reflect the true topology. This is the case for the positron events scoring extremely small *spread* values (left and right frame). The same events show up when combining *contrast* and *profile gradient* (middle frame) in the form of a loose cluster far off the main island. Most interestingly, the outliers can be identified and dismissed as background with much greater decisiveness as compared to the individual consideration of each parameter. The fact that electron events appear to be very much confined is useful as well.

The circumstances demonstrated here indicate the power that could lie in multivariate analyses. A general correlation was found – which as a matter of fact does not come unexpectedly, since all three parameters build on diffuseness in the TR result and hence on the same characteristic. However, an additional parameter taking into account e.g. the asymmetry in the reconstructed topology or structural features that depart from the picture of only one single bright spot near the reconstructed vertex could dissolve the close correlation and pull the two populations apart. Attempts in these directions have not been successful so far, since the current resolution in topology – limited by the imprecise determination of the reference time – does not reveal any such details. As for the discussed outliers it might be that they will rejoin the main population under an improved time reconstruction.

Incidentally, an external observable like e.g. the fit quality in the determination of

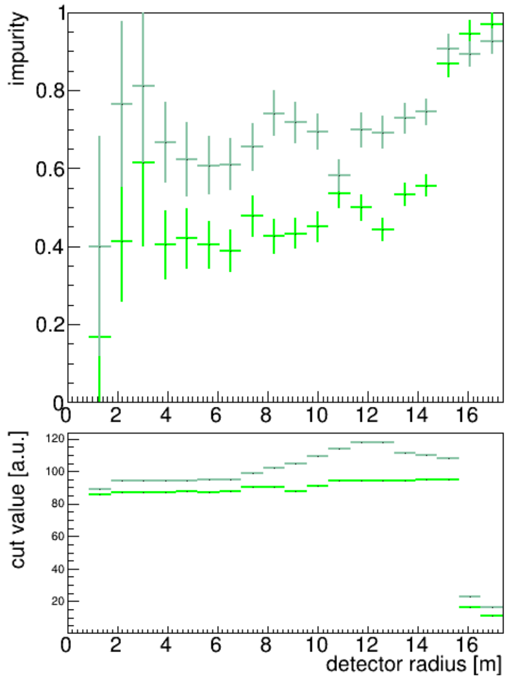

(a) *spread* parameter.

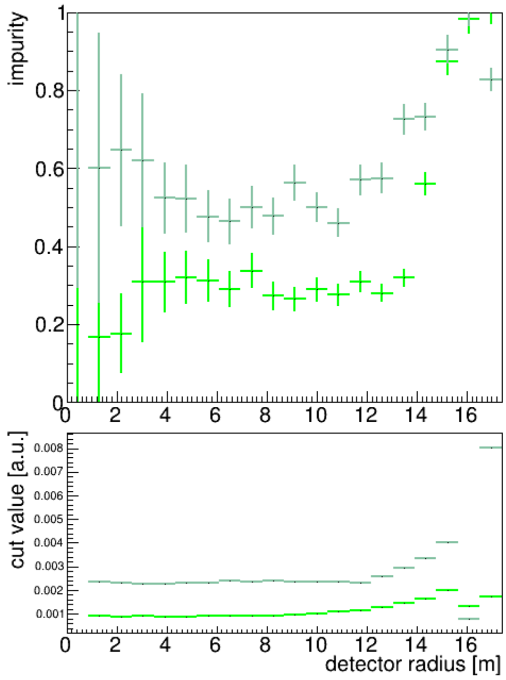

(b) *profile gradient* parameter.

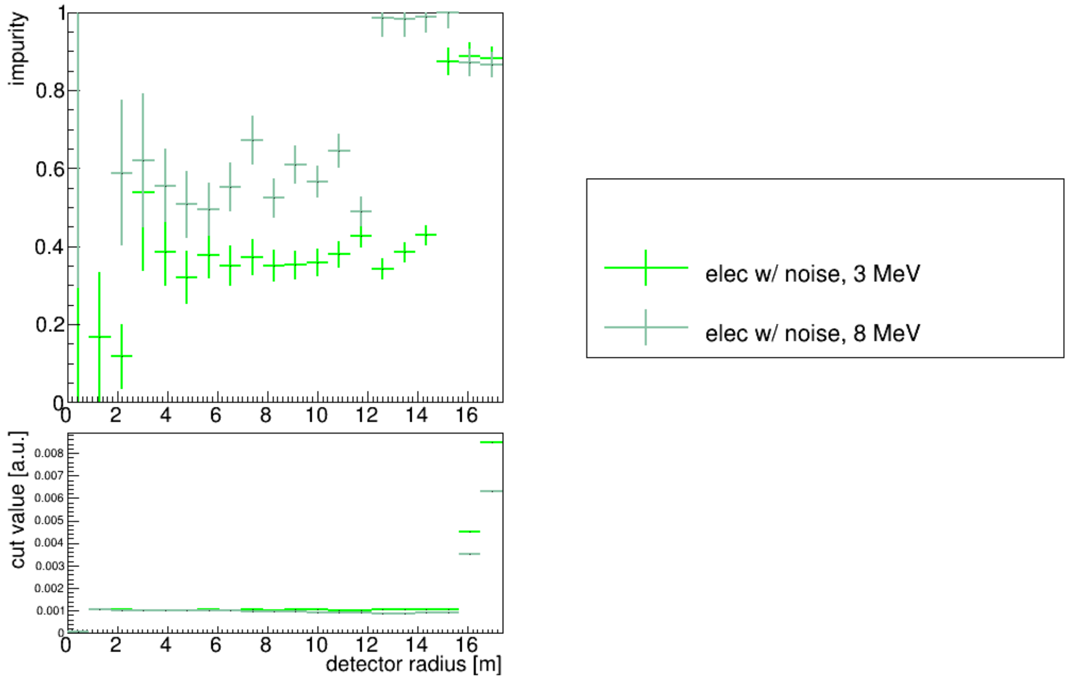

(c) *contrast* parameter.

Figure 6.11: e^-/e^+ discrimination in different energy regions for all three discrimination parameters with the *elec w/ noise* dataset at 90 % efficiency. The impurity is given as a function of detector radius. The energy stated in the legend declares events with visible energies within $[E - 0.25\,\text{MeV}, E + 0.25\,\text{MeV}]$.

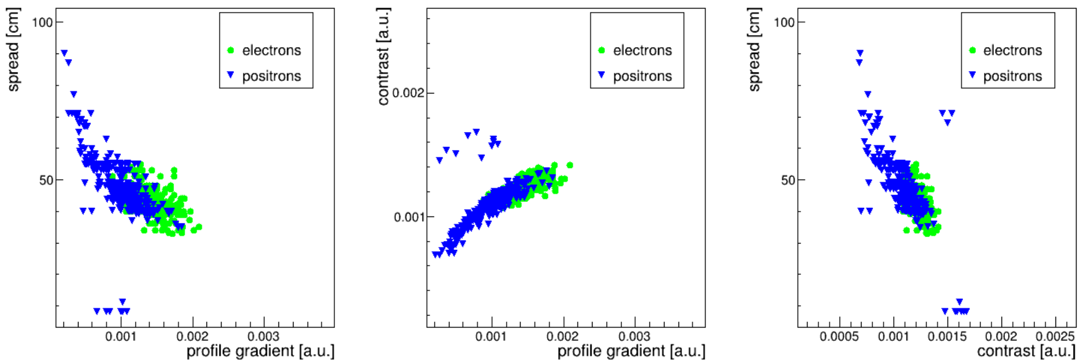

Figure 6.12: Scatter plots demonstrating the correlation between the chosen discrimination parameters. Electrons (positrons) are depicted in green (blue).

the reference time could function as a complementary dimension in the parameter space. An idea of this can be gained from Figure 6.10 (b).

6.4.2 Electron/Gamma

The analysis for electron/gamma discrimination will be presented in this section. It will be demonstrated by means of the *profile gradient* method which provided the best results in the electron/positron analysis. The following sections will likewise refer only to the *profile gradient*.

The parameter distribution for visible energies $2.5\,\text{MeV} < E_{\text{vis}} < 3.0\,\text{MeV}$ and detector radii $9.5\,\text{m} < r < 10.5\,\text{m}$ is exemplarily shown in Figure 6.13 (a). Electron and gamma events are represented by a green and a red distribution, respectively. The tendency of more blurred TR results can be confirmed also for gammas, although, compared to the counterpart from the electron/positron analysis displayed in Figure 6.7 (a), the electron and gamma distributions overlap stronger. Apparently, the blurring effect introduced by a single gamma is not appropriate to the situation with positron ionisation in the centre and two gammas flying apart from that, although with lower energies.

An overview on impurities in the same detector region within the full energy range of natural radioactivity, i.e. up to 3 MeV, is given in Figure 6.14. Again, the data stages *detsim* (black), *elec w/o noise* (red), and *elec w/ noise* (green) are depicted for 90 % (50 %) efficiency as a solid (dashed) line. The *detsim* results at 90 % efficiency decrease almost continuously between 0 and 1.8 MeV with values between 15 % and 5 %, except for energies below 0.5 MeV, where the impurity rises very sharply towards 65 %. The data points for *elec w/o noise* and *elec w/ noise* clearly follow that behaviour, which was also observed for the *spread* and *contrast* parameter in the electron/positron discrimination.

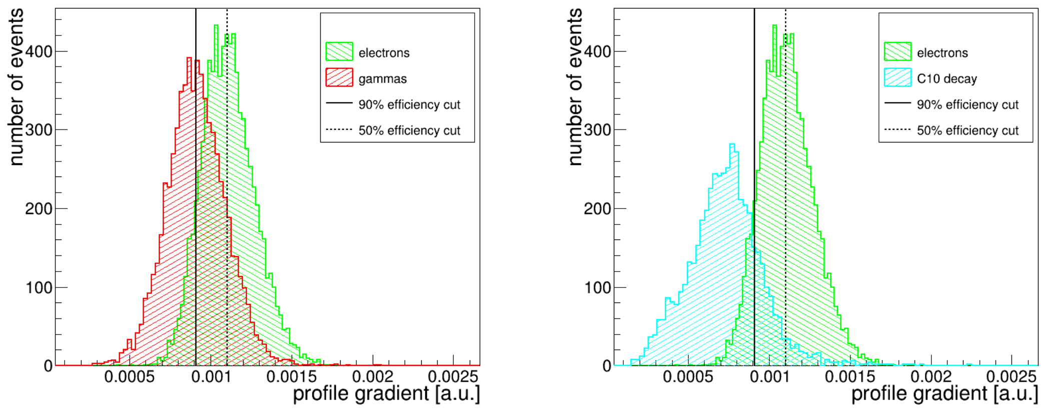

(a) e^-/γ discrimination.

(b) $e^-/^{10}$C discrimination.

Figure 6.13: Distribution of the *profile gradient* parameter at the *elec w/ noise* stage for events with visible energies 2.5 MeV $< E_{\text{vis}} <$ 3.0 MeV. The detector radius was constrained to 9.5 m $< r <$ 10.5 m.

For electron/gamma discrimination however the absolute values for the realistic datasets are worse: an impurity decrease from 90 % (50 %) around 0.5 MeV down to 55 % (20 %) at 1.8 MeV is observed, further remaining on a constant level. Like before, the impurities for *elec w/o noise* decrease earlier than for *elec w/ noise*. A subsequent rise is not to be expected since no point-like energy deposition impends to outshine the gamma depositions. If anything, the TR results at energies beyond the studied scope would be even more blurred due to incremented Compton scatterings.

The dependence of the cut performance on the detector region is shown in Figure 6.15. Events from the two energy regions 0.60 ± 0.13 MeV (light green) and 2.00 ± 0.13 MeV (dark green) were evaluated at 90 % efficiency. It was expectable from the energy dependent analysis that the low energy samples are indistinguishable also in the remaining detector regions. The higher energy samples on the other hand show a falling tendency from total indistinguishability near the detector centre to about $\approx 50\,\%$ impurity towards a 14 m radius. The cut value, which is known to rise with energy – or, to put it more accurately, with the number of unattenuated photons – experiences a continuous rise at the same time. This supports the previously phrased assumption that light yield is of great importance in the discussed energy regime below 3 MeV.

The outermost region is, like for the electron/positron discrimination, completely spoiled by effects of the detector edges on the TR.

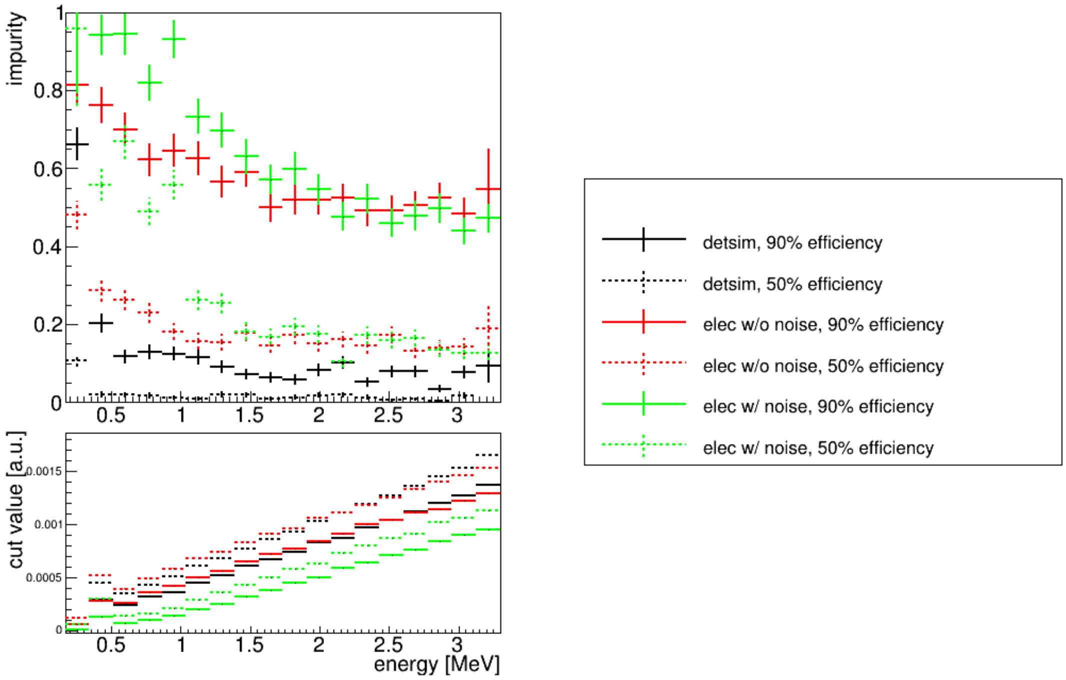

Figure 6.14: e^-/γ discrimination at different reconstruction stages for the *profile gradient* parameter. The impurity is given as a function of energy. Solid and dashed lines represent the results for efficiencies fixed to 0.9 and 0.5, respectively. Only events within a detector radius $9.5\,\mathrm{m} < r < 10.5\,\mathrm{m}$ were considered.

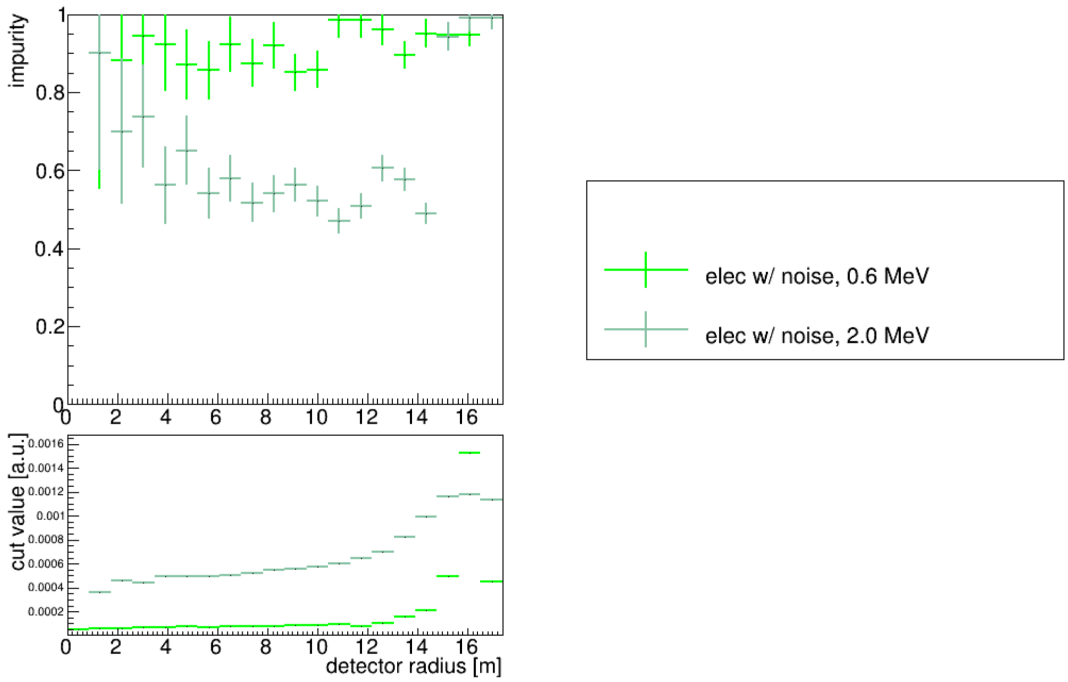

Figure 6.15: e^-/γ discrimination in different energy regions for all three discrimination parameters with the *elec w/ noise* dataset at 90 % efficiency. The impurity is given as a function of detector radius. The energy stated in the legend declares events with visible energies within $[E - 0.25\,\mathrm{MeV}, E + 0.25\,\mathrm{MeV}]$.

6.4.3 Electron/^{10}C

This section deals with the specific discrimination between electron and ^{10}C events. Not only is the β^+ decay of ^{10}C accompanied by an additional 718 keV gamma, but this gamma also comes delayed according to a lifetime of 1 ns. As a result, the parameter distributions turn out to be even more distinct, as can be seen in Figure 6.13 (b), which again considers *elec w/ noise* events with energies between 2.5 MeV and 3 MeV as well as radii between 9.5 m and 10.5 m. The ^{10}C events are, with respect to the positron events in Figure 6.7 shifted a little towards lower parameter values.

The discrimination performance in terms of accuracy will be discussed in combination with Figure 6.17 (d) and Table 6.1 throughout the analysis of the ML results in the following section.

6.5 Results from Machine Learning

TR results from data in the *elec w/ noise* stage was prepared for feeding it to the three different networks *1D-CNN*, *3D-CNN*, and *3 channel 3D-CNN* introduced in Section 6.2.2. e^-/e^+, e^-/γ, and $e^-/^{10}$C discrimination was tested in turn. The data was randomly split into a training and a validation set with the ratio 7:3. Training was stopped after 60 epochs.

The development of loss and accuracy over the epochs can be observed in Figure 6.16 (a) and (b), respectively. Loss, a summed measurement of the difference between each pair of predicted probability and actual identity of all samples, is minimised for the training data by the NN. As long as the loss decreases also for the set of validation samples, the NN is learning successfully. As soon as the validation curve turns into a rise, overfitting occurs, i.e. the network starts memorising noise features in the training samples rather than learning underlying relations.

In Figure 6.16 black lines denote the *1D-CNN*, red lines the *3D-CNN*, and green lines the *3 channel 3D-CNN* approach. Solid lines stand for the parameter as observed during training while dashed lines represent validation data. From left to right, the panels correspond to the e^-/e^+, e^-/γ, and $e^-/^{10}$C discrimination. The NNs show a general accordance between training and validation loss. Small offsets are due to statistical differences between the compositions of training and validation set. The validation loss runs into a constant level but does not rise again, i.e. overfitting is avoided. From the longer phase of strong decrease in the case of $e^-/^{10}$C discrimination in all NNs it can be deduced that the learning process works very efficiently here. The validation losses of the *3D-CNN* develops a very unsteady behaviour. The reason can be related to statistical issues, in particular can the training or validation samples be too small, or the space of hyper-parameters can be too high-dimensioned. An excessive number of hyper-parameters is unlikely, though, since the network is shallow and the filters were chosen small. The instability can possibly be fixed by reducing the learning rate, which is a hyper-parameter regulating the level of parameter adjustment within one epoch.

Both curve shapes and loss levels are closely related to the accuracy, measuring the ratio of true classifications. Table 6.1 lists accuracy values for all NNs and discrimination categories. The stated numbers are mean values of the three highest values in the curves. The table is complemented by the accuracy score from the *profile gradient* parameter cut from the previous section, evaluated at the 90 % efficiency level. For all categories a much lower performance is achieved with the *1D-CNN* than with the three-dimensional approaches, whose accuracies are very close together. This gap measures about 6, 12, and even 15 percentage points for e^-/γ, e^-/e^+, and $e^-/^{10}$C discrimination. The *3D-CNN* yields the highest accuracies: 73.6 % for e^-/γ, 80.8 % for e^-/e^+, and almost 90 % for $e^-/^{10}$C discrimination. Although the *3D-CNN* curve for validation accuracy shows a high number of occasional drops, it generally follows the corresponding training curve. The fact that the validation curve for the *3 channel 3D-CNN* behaves much more steady proofs that it is possible to find a suitable NN configuration which is capable of reaching this level of accuracy. The results from the classic approach are 3 % to 4% below those from the three-dimensional NNs. So in terms of accuracy the classic approach can almost compete with the three-dimensional CNNs.

Figure 6.17 shows the ROC curves for all CNNs ((a) - (c)), complemented by the analogue plot of efficiency over impurity from the *profile gradient* method (d) evaluated with the same datasets. The curves clearly demonstrate the rise in discrimination power going from e^-/γ (red) over e^-/e^+ (dark blue) to $e^-/^{10}$C (cyan). The according potential is also reflected by the AUC values listed in Table 6.2 for all four methods. The curves also show very impressively how the ^{10}C background can be reduced by about 80 % by the cost of only 5 % electron signal (*3D-CNN* and *3 channel 3D-CNN*). On this efficiency level positrons could still be reduced by about 50 %. JUNO's high exposure allows it to consider also lower efficiencies and still keep acceptable signal rates. The ROC curves show that the current performance is not far from the point where pure signal samples can be provided. Pure background samples are already achievable (see also the parameter distributions in Figure 6.13 (b)).

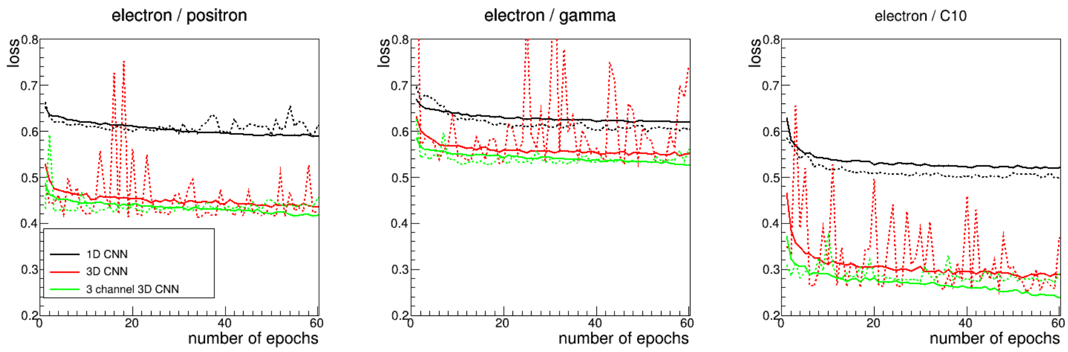

(a) Loss over number of epochs.

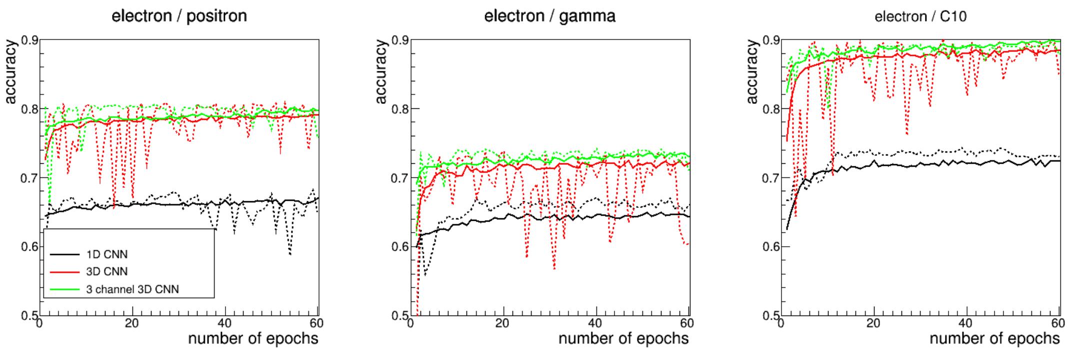

(b) Accuracy over number of epochs.

Figure 6.16: Loss and accuracy as a function of the number of epochs. The plot is shown for the different networks *1D-CNN* (black), *3D-CNN* (red) and *3 channel 3D-CNN* (green). Training and validation loss are depicted as solid and dashed lines, respectively.

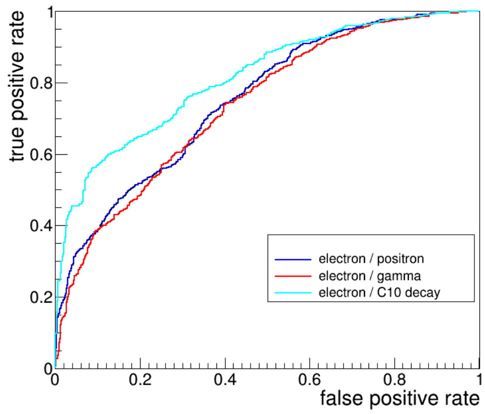

(a) 1D-CNN.

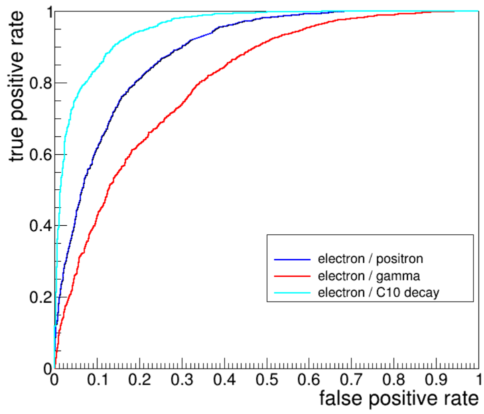

(b) 3D-CNN.

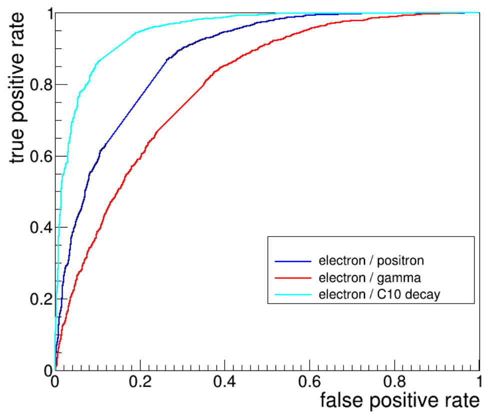

(c) 3 channel 3D-CNN.

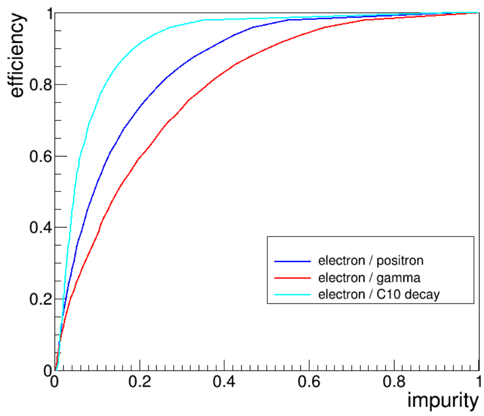

(d) *profile gradient* parameter.

Figure 6.17: ROC curves for all neural networks and one classic approach using the *profile gradient* parameter. Dark blue, red, and cyan lines represent the e^- / e^+, e^- / γ, and e^- / ^{10}C discrimination, respectively.

Table 6.1: Comparison of accuracies between the different neural networks and one classic approach using the *profile gradient* parameter. The statistical $1\,\sigma$ uncertainty for the classic approach is given in parentheses.

category	accuracy [%]			
	1D-CNN	3D-CNN	3ch 3D-CNN	classic
e^- / e^+	67.9	80.8	80.5	76.9 (3)
e^- / γ	67.0	73.6	74.1	69.9 (4)
e^- / ^{10}C	74.2	89.8	89.4	85.8 (3)

Table 6.2: Comparison of ROC AUC scores between the different neural networks and one classic approach using the *profile gradient* parameter.

category	ROC AUC [%]			
	1D-CNN	3D-CNN	3ch 3D-CNN	classic
e^- / e^+	75.1	88.7	87.6	85.4
e^- / γ	73.7	80.3	79.6	79.0
e^- / ^{10}C	81.2	95.3	95.0	91.8

6.6 Discussion

The presented event discrimination can be viewed as an entanglement of mainly three constituent parts: the reconstruction of vertex and time, the TR, and the analysis method.

It has been demonstrated how especially the reconstruction of the reference time has a high impact on the discrimination results. The current reference time was found to have an offset which develops linearly with energy for electron events. It should be easy to introduce an energy dependent correction after investigating also the dependence on detector radius.

For the TR part, several configurations and variants were tested in the course of this study, not all of which have been presented. It shall be mentioned that the use of *crystallisation*, described in Section 5.2.5, did not improve the discrimination power, although the results from the chosen standard procedure could be approached. Also the algorithm for the removal of scattered light, mentioned in Section 5.2.4 and described in [120], did not mean an improvement – on the contrary, the discrimination became completely ineffective. This contradicts the expectations which build on the assumption that a higher amount of direct photons leads to sharper TR results. The latter hypothesis was supported by the presented analysis results. A closer inspection of the scatter algorithm is needed in order to be able to exploit its full potential.

An important issue for the TR is the reduction of edge effects. The distortions which currently occur at large detector radii negatively affect the discrimination. Maybe an improved time reconstruction already brings an improvement.

The bad results at large radii must also be addressed from the analysis side. A reasonable approach would be to build the event profile only based on voxels on the side facing the detector centre when seen from the reference point as soon as the reduced probability mask interferes with the detector edge. Another strategy would be to reduce the size of the spherical region of interest (see Section 5.2.6) when approaching the detector edge.

In case that the improved time reconstruction leads to TR results which reveal more features in the topological structure, it can be worthwhile to add more discrimination parameters to the study, e.g. measures for asymmetry and cluster formation. These would provide complementary information and are thus promising parameters for multivariate analyses.

Such topological details can also improve the ML approach. It might be necessary to further develop the network architectures. More complex and deeper models can help to take up a maximum of the accessible information. An common approach is the addition of further data on a deeper NN layer. This data could e.g. be the fit quality in the time reconstruction or the tof-corrected spectrum of hit times.

Conclusion and Outlook

Large unsegmented liquid scintillator detectors are a state-of-the-art technology for the detection of neutrinos and antineutrinos. The JUNO experiment has the potential to give answers to several open issues in neutrino and astroparticle physics, most notably by determining the mass ordering (MO), a precise measurement of the solar oscillation parameters, and studying the fluxes of solar ^{7}Be and ^{8}B neutrinos.

In this thesis it was successfully demonstrated that thanks to the high photoelectron yield it is possible to separate electron and positron events on a statistical basis in JUNO, which is a novelty in the field. Furthermore, the developed methods proved to be sensible even to electron/gamma discrimination, although to a smaller extend. Topological Reconstruction (TR) was used as a tool to visualise differences in the energy deposition. It turned out that electron events result in sharper images than gamma and especially positron events, which produce two annihilation gammas.

The TR software framework was adapted in order to handle JUNO data. This included an in-depth study of JUNO's optical model in order to calculate look-up tables. These were found to be in very good agreement with simulation results. The implementation will further serve as a basis not only for follow-up low energy studies but also for track reconstruction for GeV particles, e.g. muons.

The analysis itself was split into a classic approach using single parameter cuts on the one hand and the application of machine learning techniques on the other. The classic method achieved a rate of correctly classified events, referred to as accuracy, of 76.9 (3) % for electron/positron and 69.9 (4) % for electron/gamma discrimination for events within (2.75 ± 0.25) MeV. In the special case of the gamma-accompanied β^{+}-decay of ^{10}C, which is major background for the measurement of ^{8}B neutrinos, the accuracy could be enhanced to 85.8 (3) %. A shallow three-dimensional convolutional neural network (CNN) was able to exceed these values, reaching accuracies of 80.8 % for electron/positron, 73.6 % for electron/gamma, and 89.8 % for electron/^{10}C discrimination.

The single parameter approach proves to be almost competitive with the CNN and, moreover, reveals how topology features in low energy events actually affect the TR.

The analysis greatly helps to shape and push forward the understanding of the TR method. Furthermore, in showing a general consistency the two approaches strengthen and support each other.

The energy dependence of the cut was studied with the classic approach. The background contamination increases with energy. This is in accordance with the expectation because the central energy deposition brightens with energy and at some point outshines the adjacent gamma depositions. The rise in impurity for electron/positron discrimination was observed to be 30 percentage points between 1 MeV and 10 MeV. Electron/gamma separation was investigated up to 3 MeV and showed a continuous weakening for low energies below 1.5 MeV. The reason is most probably the decreasing number of photoelectrons which mean a lack of statistical information.

For JUNO the electron/positron discrimination is of great importance as it opens up a new way of background suppression. Solar neutrino measurements can profit enormously from the reduction of cosmogenic ^{11}C and, very importantly, ^{10}C events. The method can remove 80 % ^{10}C events with 95 % signal efficiency in the current configuration and thus compensate partly for JUNO's comparatively moderate overburden. The discrimination method in the current configuration has the potential to provide highly pure background samples of β^+ emitters. As it could be shown that the background contamination is highly sensitive on the resolution of time reconstruction prior to TR, a considerably better result can be expected as soon as an improved time reconstruction enters the TR. A simple time offset can lead to an enhancement already. This could enable the method to provide also signal samples of high purity.

Even though – with currently more than one order of magnitude remaining in between – it remains to be seen if the discrimination power will reach a level which would suffice in itself to make the signal of ^{8}B neutrinos visible against ^{10}C background, a combination with future methods for directionality reconstruction based on Cherenkov light could lead to a breakthrough.

As for the determination of MO, the discrimination cannot replace the spatial muon vetoes given its current accuracy. Rate measurements of ^{8}He and ^{9}Li will nevertheless profit strongly from the availability of enriched electron samples.

The local cut performance was investigated again with the classic approach. Although being stable throughout the largest part of the detector, the classification suffered from a breakdown of discrimination power towards the detector edge. Events within the outermost 3 metres of detector radius were found to be indistinguishable. This drawback is serious especially with regard to the reduction of external gammas. The sources of error were identified and are, firstly, an abrupt boundary effect at the detector edge which can presumably be handled by means of an adaption in the determination of discrimination parameters. Secondly, the TR often failed to reconstruct events at large radii. It needs to be investigated how the reconstruction of low energy events can be ensured in this detector region.

A future refinement of the TR, e.g. by improving the time reconstruction or the algorithm for scattered light removal, can mean that further topological features will be revealed in the TR results. This would offer new possibilities with regard to both the classic and the machine learning approach. The current set of discrimination parameters, which are all based on diffuseness in the TR result, can be complemented by parameters considering e.g. asymmetries or cluster formation in the TR result. A multivariate analysis is then reasonable. Machine learning, currently realised with CNNs that have a rather simple architecture, will be able to develop its full potential when manifold topology features occur. It will be appropriate for the networks to increase in complexity in order to cope with their task. This can mean to add more layers or also to include more event data on a deeper level.

As soon as JUNO is running it will be necessary to calibrate the discrimination methods with real data. The preferable way involves the use of highly pure electron and positron samples. Since β emitters hardly penetrate a surrounding vessel, external sources cannot be used. Instead, one could work with enriched samples. Positron events can easily be selected from the delayed IBD coincidence. Electron events can be chosen from the mainly β^- dominated single site spectrum and interpolated within the β^+ dominated regions.

An idea for electron/positron discrimination which was not pursued in this thesis but is considered worth investigating is to exclude those photons from the TR process whose time-of-flight-corrected hit times match very good with the probable vertex, and thus mask out the central energy deposition from the positron or electron ionisation. Potentially, the gamma contributions in positron events come more into focus by doing so and maybe the increase of impurity at higher energies can be weakened.

From the physics point of view an efficient discrimination at higher energies is highly desirable for it will allow a charge reconstruction of muons which decay at the end of their track. This so-called Michel decay produces electrons and positrons with a few tens of MeV. With an additional separation between electron-like and muon-like events all requirements for an MO measurement are at hand – even though limited by statistics. Nonetheless, a detector being sensitive to MO via two complementary methods would be of unique significance.

List of Figures

List of Tables

Bibliography

[1] F. An et al. Neutrino Physics with JUNO. *J. Phys. G*, 43, 2016. doi:10.1088/0954-3899/43/3/030401.

[2] O. Smirnov et al. Solar neutrino with Borexino: Results and perspectives. *Phys. Part. Nuclei*, 46(166), 2015. doi:10.1134/S1063779615020185.

[3] D. Franco et al. Positronium signature in organic liquid scintillators for neutrino experiments. *Phys. Rev. C*, 83(015504), 2011. doi:10.1103/PhysRevC.83.015504.

[4] B. S. Wonsak et al. Topological track reconstruction in unsegmented, large-volume liquid scintillator detectors. *J. Instrum.*, 13(07):P07005–P07005, jul 2018. doi:10.1088/1748-0221/13/07/p07005.

[5] M. Tanabashi et al. *Phys. Rev. D*, 98(030001), 2018. URL `http://pdg.lbl.gov/`. (Particle Data Group).

[6] S. Bilenky. *Introduction to the Physics of Massive and Mixed Neutrinos*. Springer International Publishing, 2 edition, 2018. doi:10.1007/978-3-319-74802-3.

[7] Kai Zuber. *Neutrino Physics*. CRC Press, 2 edition, 2012. doi:10.1201/b11065.

[8] L. Wolfenstein. Neutrino oscillations in matter. *Phys. Rev. D*, 17(9):2369, 1978. doi:10.1103/PhysRevD.17.2369.

[9] S. P. Mikheev and A. Y. Smirnov. Resonance enhancement of oscillations in matter and solar neutrino spectroscopy. *Sov. J. Nucl. Phys.*, 42(6), 1985. URL `https://www.osti.gov/biblio/5714592`.

[10] B. Pontecorvo. Inverse beta processes and nonconservation of lepton charge. *Sov. Phys. JETP*, 7:172–173, 1957. URL `http://inspirehep.net/record/42736?ln=de`.

[11] Z. Maki, M. Nakagawa, and S. Sakata. Remarks on the unified model of elementary particles. *Prog. Theor. Phys.*, 28(5):870–880, 1962. doi:10.1143/PTP.28.870.

[12] I. Esteban et al. Global analysis of three-flavour neutrino iscillations: synergies and tensions in the determination of θ_{23}, δ_{CP}, and the mass ordering. *J. High Energ. Phys.*, 106, 2019. doi:10.1007/JHEP01(2019)106.

[13] J. N. Bahcall. *Neutrino Astrophysics.* Cambridge University Press, 1989.

[14] N. Vinyoles et al. A New Generation of Standard Solar Models. *Astrophys. J.*, 835 (2), 2017. doi:10.3847/1538-4357/835/2/202.

[15] A. Gallo Rosso et al. Introduction to neutrino astronomy. *Eur. Phys. J. Plus*, 133 (7):267, Jul 2018. ISSN 2190-5444. doi:10.1140/epjp/i2018-12143-6.

[16] K. S. Hirata et al. Observation of 8B solar neutrinos in the Kamiokande-II detector. *Phys. Rev. Lett.*, 63(16), 1989. doi:10.1103/PhysRevLett.63.16.

[17] K. Abe et al. Solar neutrino measurements in Super-Kamiokande-IV. *Phys. Rev. D*, 94(5), 2016. doi:10.1103/PhysRevD.94.052010.

[18] A. Bellerive et al. The Sudbury Neutrino Observatory. *J. Nucl. Phys. B*, 908: 30–51, 2016. doi:10.1016/j.nuclphysb.2016.04.035.

[19] B. Aharmim et al. Electron energy spectra, fluxes, and day-night asymmetries of ^{8}B solar neutrinos from measurements with NaCl dissolved in the heavy-water detector at the Sudbury Neutrino Observatory. *Phys. Rev. C*, 72:055502, Nov 2005. doi:10.1103/PhysRevC.72.055502.

[20] G. Bellini et al. Final results of Borexino Phase-I on low-energy solar neutrino spectroscopy. *Phys. Rev. D*, 89(11), 2014. doi:10.1103/PhysRevD.89.112007.

[21] G. Bellini et al. Neutrinos from the primary proton–proton fusion process in the Sun. *Nature*, 512:383–386, 2014. doi:10.1038/nature13702. Borexino Collaboration.

[22] J. F. Beacom et al. Physics prospects of the Jinping neutrino experiment. *Chin. Phys. C*, 41(2), 2017. doi:10.1088/1674-1137/41/2/023002.

[23] A. Serenelli. New Solar Composition: The Problem With Solar Models Revisited. *Astrophys. J.*, 705, 2009. doi:10.1088/0004-637X/705/2/L123.

[24] S. Andringa et al. Current Status and Future Prospects of the SNO+ Experiment. *Adv. High Energy Phys.*, (6194250), 2016. doi:10.1155/2016/6194250.

[25] A. Gando et al. Constraints on θ_{13} from A Three-Flavor Oscillation Analysis of Reactor Antineutrinos at KamLAND. *Phys. Rev. D*, 83(052002), 2011. doi:10.1103/PhysRevD.83.052002.

[26] M. Maltoni and A. Y. Smirnov. Solar neutrinos and neutrino physics. *Eur. Phys. J. A*, 52(87), 2016. doi:10.1140/epja/i2016-16087-0.

[27] T. Kajita. Neutrino Oscillation Studies with Atmospheric Neutrinos. In *Neutrinos in particle physics, astrophysics and cosmology*, Scottish Graduate Series, pages 217–237. CRC Press, 2009.

[28] K. S. Hirata et al. Observation of a small atmospheric ν_μ/ν_e ratio in Kamiokande. *Phys. Lett. B*, 280(1-2):146–152, 1992. doi:10.1016/0370-2693(92)90788-6.

[29] K. Abe et al. Atmospheric neutrino oscillation analysis with external constraints in Super-Kamiokande I-IV. *Phys. Rev. D*, 97, 2018. doi:10.1103/PhysRevD.97.072001.

[30] A. Timmons. The Results of MINOS and the Future with MINOS+. *Adv. High Energy Phys.*, 2016(7064960), 2016. doi:10.1155/2016/7064960.

[31] K. Abe et al. Combined Analysis of Neutrino and Antineutrino Oscillations at T2K. *Phys. Rev. Lett.*, 118(151801), 2017. doi:10.1103/PhysRevLett.118.151801.

[32] P Adamson et al. Measurement of the Neutrino Mixing Angle Theta 23 in NOvA. *Phys. Rev. Lett.*, 118, 04 2017. doi:10.1103/PhysRevLett.118.151802.

[33] V. Vorobel. Recent Results from Daya Bay. *Phys. Part. Nuclei*, 49(713), 2018. doi:10.1134/S1063779618040585.

[34] G. Bak et al. Measurement of Reactor Antineutrino Oscillation Amplitude and Frequency at RENO. *Phys. Rev. Lett.*, 121(201801), 2018. doi:10.1103/PhysRevLett.121.201801.

[35] M. Kaneda et al. Recent Results from Double Chooz. *Phys. Part. Nuclei*, 49(709), 2018. doi:10.1134/S1063779618040317.

[36] P. F. de Salas et al. Neutrino Mass Ordering from Oscillations and Beyond: 2018 Status and Future Prospects. *Front. Astron. Space Sci.*, 2018. doi:10.3389/fspas.2018.00036.

[37] G. G. Raffelt and A.Y. Smirnov. Self-induced spectral splits in supernova neutrino fluxes. *Phys. Rev. D*, 76(8), 2007. doi:10.1103/PhysRevD.76.081301.

[38] T. Kajino et al. Neutrinos in core-collapse supernovae and nucleosynthesis. *J. Phys. G*, 41(4), 2014. doi:10.1088/0954-3899/41/4/044007.

[39] C.S. Lim and T. Inami. Lepton Flavor Nonconservation and the Mass Generation Mechanism for Neutrinos. *Prog. Theor. Phys.*, 67(1569), 1982. doi:10.1143/PTP.67.1569.

[40] R. B. Patterson. Prospects for Measurement of the Neutrino Mass Hierarchy. *Annu. Rev. Nucl. Part. Sci.*, 65:177–192, 2015. doi:10.1146/annurev-nucl-102014-021916.

[41] K. Abe et al. Hyper-Kamiokande Design Report. 2018. URL `https://arxiv.org/abs/1805.04163`.

[42] J. Brunner. Measurement of Neutrino Oscillations with Neutrino Telescope. *Adv. High Energy Phys.*, 2013. doi:10.1155/2013/782538.

[43] The IceCube-Gen2 Collaboration. PINGU: A Vision for Neutrino and Particle Physics at the South Pole. *J. Phys. G*, 44(5), 2017. doi:10.1088/1361-6471/44/5/054006.

[44] M. G. Aartsen et al. Probing the Neutrino Mass Ordering with Atmospheric Neutrinos from Three Years of IceCube DeepCore Data. *Eur. Phys. J. C*, 2019. URL `https://arxiv.org/abs/1902.07771v1`.

[45] T. Chiarusi. Neutrino astronomy and oscillation research in the Mediterranean: ANTARES and KM3NeT. *Nucl. Instrum. Methods Phys. Res., Sect. A*, 2018. doi:10.1016/j.nima.2018.11.112.

[46] K. Chakraborty et al. Spotlighting the sensitivities of Hyper-Kamiokande, DUNE and ESSvSB. *Nucl. Phys. B*, 937:303–332, 2018. doi:10.1016/j.nuclphysb.2018.10013.

[47] R. Acciarri. Long-Baseline Neutrino Facility (LBNF) and Deep Underground Neutrino Experiment (DUNE) Conceptual Design Report Volume 2: The Physics Program for DUNE at LBNF. 2016. URL `https://arxiv.org/abs/1512.06148v2`.

[48] M. A. Acero et al. New constraints on oscillation parameters from ν_e appearance and ν_μ disappearance in the NOνA experiment. *Phys. Rev. D*, 98(032012), 2018. doi:10.1103/PhysRevD.98.032012.

[49] N. Aghanim et al. Planck 2018 results. VI. Cosmological parameters. 2018. URL `https://arxiv.org/abs/1807.06209`.

[50] R. A. C. Croft et al. Intensity mapping with SDSS/BOSS Lyman-α emission, quasars, and their Lyman-α forest. *Mon. Not. R. Astron. Soc.*, 481(1), 2018. doi:10.1093/mnras/sty2302.

[51] T. M. C. Abbott et al. Dark Energy Survey year 1 results: Cosmological constraints from galaxy clustering and weak lensing. *Phys. Rev. D*, 98(4), 2018. doi:10.1103/PhysRevD.98.043526.

[52] F. N. D. Kurie et al. The Radiations Emitted from Artificially Produced Radioactive Substances. I. The Upper Limits and Shapes of the β-Ray Spectra from Several Elements. *Phys. Rev.*, 49(368), 1936. doi:10.1103/PhysRev.49.368.

[53] P. F. de Salas et al. Status of neutrino oscillations 2018: $3sigma$ hint for mass ordering and improved CP sensitivity. *Phys. Lett. B*, 782:663–640, 2018. doi:10.1016/j.physletb.2018.06.019.

[54] B. A. Robson. *Cosmology, Gravitational Waves and Particles*, chapter "The Matter-antimatter Asymmetry Problem", pages 154–162. World Scientific, 2018. doi:10.1142/9789813231801_0014.

[55] Z. Bai et al. Standard Model Prediction for Direct CP Violation in $K \to \pi\pi$ Decay. *Phys. Rev. Lett.*, 115(212001), 2015. doi:10.1103/PhysRevLett.115.212001.

[56] M. Artuso et al. CP violation in the B_s^0 system. *Rev. Mod. Phys.*, 44(045002), 2016. doi:10.1103/RevModPhys.88.045002.

[57] V. N. Aseev et al. Upper limit on the electron antineutrino mass from the Troitsk experiment. *Phys. Rev. D*, 84(112003), 2011. doi:10.1103/PhysRevD.84.112003.

[58] Ch. Kraus et al. Final Results from phase II of the Mainz Neutrino Mass Search in Tritium β Decay. *Eur. Phys. J. C*, 40:447–468, 2005. doi:10.1140/epjc/s2005-02139-7.

[59] J. Wolf et al. The KATRIN neutrino mass experiment. *Nucl. Instrum. Methods Phys. Res., Sect. A*, 623(1):442–444, 2010. doi:10.1016/j.nima.2010.03.030.

[60] A. A. Esfashani. Determining the neutrino mass with cyclotron radiation emission spectroscopy–Project 8. *J. Phys. G*, 44(5), 2017. doi:10.1088/1361-6471/aa5b4f.

[61] E. Majorana. Teoria simmetrica dell'elettrone e del positrone. *Nuovo Cim.*, 14 (171), 1937. doi:10.1007/BF02961314.

[62] J. Schechter and J. W. F. Valle. Neutrinoless double-β decay in SU(2)$\times$U(1) theories. *Phys. Rev. D*, 25(2951), 1982. doi:10.1103/PhysRevD.25.2951.

[63] M. Agostini et al. Improved Limit on Neutrinoless Double-β Decay of 76Ge from GERDA Phase II. *Phys. Rev. Lett.*, 120(132503), 2018. doi:10.1103/PhysRevLett.120.132503.

[64] C. Alduino et al. First Results from CUORE: A Search for Lepton Number Violation via $0\nu\beta\beta$ Decay of 130Te. *Phys. Rev. Lett.*, 120(132501), 2018. doi:10.1103/PhysRevLett.120.132501.

[65] A. Gando et al. Search for Majorana Neutrinos Near the Inverted Mass Hierarchy Region with KamLAND-Zen. *Phys. Rev. Lett.*, 117(082503), 2016. doi:10.1103/PhysRevLett.117.082503.

[66] N. Abgrall et al. The large enriched germanium experiment for neutrinoless double beta decay (LEGEND). *AIP Conf. Proc.*, 1894(020027), 2017. doi:10.1063/1.5007652.

[67] J. B. Albert et al. Sensitivity and discovery potential of the proposed nEXO experiment to neutrinoless double-β decay. *Phys. Rev. C*, 97(065503), 2018. doi:10.1103/PhysRevC.97.065503.

[68] C. Giunti et al. Update of short-baseline electron neutrino and antineutrino disappearance. *Phys. Rev. D*, 86(113014), 2012. doi:10.1103/PhysRevD.86.113014.

[69] G. Mention et al. Reactor antineutrino anomaly. *Phys. Rev. D*, 83(073006), 2011. doi:10.1103/PhysRevD.83.073006.

[70] A. Aguilar-Arevalo et al. Evidence for neutrino oscillations from the observation of anti-neutrino(electron) appearance in a anti-neutrino(muon) beam. *Phys. Rev. D*, 64(112007), 2001. doi:10.1103/PhysRevD.64.112007.

[71] A. Aguilar-Arevalo et al. Improved Search for $\bar{\nu}_\mu \rightarrow \bar{\nu}_e$ Oscillations in the MiniBooNE Experiment. *Phys. Rev. Lett.*, 110(161801), 2013. doi:10.1103/PhysRevLett.110.161801.

[72] M. Dentler et al. Updated global analysis of neutrino oscillations in the presence of eV-scale sterile neutrinos. *J. High Energ. Phys.*, 2018. doi:10.1007/JHEP08(2018)010.

[73] C. Grupen. *Teilchendetektoren.* BI-Wiss.-Verl., 1993.

[74] 2019. URL `https://www.nist.gov/pml/stopping-power-range-tables-electrons-protons-and-hel` NIST.

[75] 2019. URL `http://physics.nist.gov/PhysRefData`. NIST.

[76] M. Yeh et al. Gadolinium-loaded liquid scintillator for high-precision measurements of antineutrino oscillations and the mixing angle, θ_{13}. *Nucl. Instrum. Methods Phys. Res., Sect. A*, 578:329–339, 2007. doi:10.1016/j.nima.2007.03.029.

[77] J. A. B. Gibson and A. E. Lally. Liquid scintillation counting as an analytical tool. A review. *Analyst*, 96(1147), 1971. doi:10.1039/AN9719600681.

[78] J. B. Birks. Scintillations from Organic Crystals: Specific Fluorescence and Relative Response to Different Radiations. *Proc. Phys. Soc. A*, 64(10):874–877, 1951. doi:10.1088/0370-1298/64/10/303.

[79] T. Kaptanoglu et al. Cherenkov and scintillation light separation using wavelength in LAB based liquid scintillator. *J. Instrum.*, 14(05), 2019. doi:10.1088/1748-0221/14/05/T05001.

[80] Provided by the JUNO Collaboration.

[81] G. Alimonti. Light propagation in a large volume liquid scintillator. *Nucl. Instrum. Methods Phys. Res., Sect. A*, 440(2):360–371, 2000. doi:10.1016/S0168-9002(99)00961-4.

[82] M. Wurm et al. Optical scattering lengths in large liquid-scintillator neutrino detectors. *Rev. Sci. Instrum.*, 81(053301), 2010. doi:10.1063/1.3397322.

[83] *Photomultiplyer Tubes – Basics and Applications.* HAMAMATSU, 3a edition, 2007. URL `https://www.hamamatsu.com/resources/pdf/etd/PMT_handbook_v3aE.pdf`.

[84] P. Eckert et al. Characterisation studies of silicon photomultipliers. *Nucl. Instrum. Methods Phys. Res., Sect. A*, 620:217–226, 2010. doi:10.1016/j.nima.2010.03.169.

[85] *An Introduction to the Silicon Photomultiplier.* sensL, 2011. URL `https://www.sensl.com/downloads/ds/TN%20-%20Intro%20to%20SPM%20Tech.pdf`.

[86] M. J. Minot et al. Large Area Picosecond Photodetector (LAPPD) - Pilot production and development status. *Nucl. Instrum. Methods Phys. Res., Sect. A*, 2018. doi:10.1016/j.nima.2018.11.137.

[87] A. R. Back. Accelerator Neutrino Neutron Interaction Experiment (ANNIE): Preliminary Results and Physics Phase Proposal. 2017. URL `https://arxiv.org/abs/1707.08222v2`.

[88] J. R. Alonso et al. Advanced Scintillator Detector Concept (ASDC): A Concept Paper on the Physics Potential of Water-Based Liquid Scintillator. 2014. URL `https://arxiv.org/abs/1409.5864v3`.

[89] D. V. Forero. The benefits of a near detector for JUNO. 2017. URL `https://arxiv.org/abs/1710.07378v1`.

[90] M. Li et al. Separation of Scintillation and Cherenkov Lights in Linear Alkyl Benzene. *Nucl. Instrum. Methods Phys. Res., Sect. A*, 830:303–308, 2016. doi:10.1016/j.nima.2016.05.132.

[91] J. Caravaca et al. Cherenkov and scintillation light separation in organic liquid scintillators. *Eur. Phys. J. C*, 77(811), 2017. doi:10.1140/epjc/s10052-017-5380-x.

[92] M. Askins et al. The Physics and Nuclear Nonproliferation Goals of WATCHMAN: A WAter CHerenkov Monitor for ANtineutrinos. 2015. URL `https://arxiv.org/abs/1502.01132v1`.

[93] T. Adam et al. The OPERA experiment Target Tracker. *Nucl. Instrum. Methods Phys. Res., Sect. A*, 577(3), 2007. doi:10.1016/j.nima.2007.04.147.

[94] M. He et al. Double calorimetry system in JUNO. *Radiat. Detect. Technol. Methods*, 1(21), 2017. doi:10.1007/s41605-017-0022-2.

[95] D. A. Dwyer and T. J. Langford. Spectral Structure of Electron Antineutrinos from Nuclear Reactors. *Phys. Rev. Lett.*, 114(012502), 2015. doi:10.1103/PhysRevLett.114.012502.

[96] M. Blennow et al. Quantifying the sensitivity of oscillation experiments to the neutrino mass ordering. *J. High Energ. Phys.*, 28, 2014. doi:10.1007/JHEP03(2014)028.

[97] G. Audi et al. The NUBASE2016 evaluation of nuclear properties. *Chin. Phys. C*, 41(3), 2017. doi:10.1088/1674-1137/41/3/030001.

[98] M. Blennow and T. Schwetz. Determination of the neutrino mass ordering by combining PINGU and Daya Bay II. *J. High Energ. Phys.*, 89, 2013. doi:10.1007/JHEP09(2013)089.

[99] M. G. Aartsen et al. Combined sensitivity to the neutrino mass ordering with JUNO and PINGU/IceCube Upgrade. in preparation.

[100] M. Asplund et al. The Chemical Composition of the Sun. *Annu. Rev. Astron. Astrophys.*, 47:481–522, 2009. doi:10.1146/annurev.astro.46.060407.145222.

[101] S. Vagnozzi. New Solar Metallicity Measurements. *Atoms*, 7(2), 2019. doi:10.3390/atoms7020041.

[102] S. Basu and H. M. Antia. Helioseismology and Solar Abundances. *Phys. Rep.*, 457 (5-6), 2008. doi:10.1016/j.physrep.2007.12.002.

[103] A. Mirizzi et al. Supernova neutrinos: Production, oscillations and detection. *Riv. del Nuovo Cim.*, 39(1-2), 2016. doi:10.1393/ncr/i2016-10120-8.

[104] K. Hirata et al. Observation of a neutrino burst from the supernova SN1987A. *Phys. Rev. Lett.*, 58(1490), 1987. doi:10.1103/PhysRevLett.58.1490.

[105] M. Apollonio et al. Determination of neutrino incoming direction in the CHOOZ experiment and its application to supernova explosion location by scintillator detectors. *Phys. Rev. D*, 61(012001), 1999. doi:10.1103/PhysRevD.61.012001.

[106] J. F. Beacom. The Diffuse Supernova Neutrino Background. *Annu. Rev. Nucl. Part. Sci.*, 60, 2010. doi:10.1146/annurev.nucl.010909.083331.

[107] M. Wurm et al. The next-generation liquid-scintillator neutrino observatory LENA. *Astropart. Phys.*, 35(11), 2012. doi:10.1016/j.astropartphys.2012.02.011.

[108] G. Bellini et al. Observation of geo-neutrinos. *Phys. Lett. B*, 687(4-5), 2010. doi:10.1016/j.physletb.2010.03.051.

[109] I. Shimizu et al. Partial radiogenic heat model for Earth revealed by geoneutrino measurements. *Nat. Geosci.*, 4, 2011. doi:10.1038/ngeo1205.

[110] R. Han et al. Potential of geo-neutrino measurements at JUNO. *Chin. Phys. C*, 40(3), 2016. doi:10.1088/1674-1137/40/3/033003.

[111] T. Li et al. Design and development of JUNO event data model. *Chin. Phys. C*, 41(6), 2017. doi:10.1088/1674-1137/41/6/066201.

[112] J. H. Zou et al. SNiPER: an offline software framework for non-collider physics experiments. *J. Phys. Conf. Series*, 47(46), 2015. doi:10.1088/1742-6596/664/7/072053.

[113] R. Brun and F. Rademakers. ROOT — An object oriented data analysis framework. *Nucl. Instrum. Methods Phys. Res., Sect. A*, 389(1-2), 1997. doi:10.1016/S0168-9002(97)00048-X.

[114] S. Agostinelli et al. Geant4—a simulation toolkit. *Nucl. Instrum. Methods Phys. Res., Sect. A*, 506(3), 2003. doi:10.1016/S0168-9002(03)01368-8.

[115] M. Grassi et al. Charge reconstruction in large-area photomultipliers Charge reconstruction in large-area photomultipliers. *J. Instrum.*, 13, 2018. doi:10.1088/1748-0221/13/02/P02008.

[116] C. Genster et al. Muon reconstruction with a geometrical model in JUNO. *J. Instrum.*, 13, 2018. doi:10.1088/1748-0221/13/03/T03003.

[117] Q. Liu et al. A vertex reconstruction algorithm in the central detector of JUNO. *J. Instrum.*, 13, 2018. doi:10.1088/1748-0221/13/09/T09005.

[118] W. Wu et al. A new method of energy reconstruction for large spherical liquid scintillator detectors. *J. Instrum.*, 14, 2019. doi:10.1088/1748-0221/14/03/P03009.

[119] Sebastian Lorenz. *Topological Track Reconstruction in Liquid Scintillator and LENA as a Far-Detector in an LBNO Experiment.* PhD thesis, Universität Hamburg, 2016. URL `http://www.neutrino.uni-hamburg.de/sites/site_neutrino/content/e60876/e60879/e279717/infoboxContent279721/Dissertation_SLorenz.pdf`.

[120] F. Benckwitz. Applications of topological reconstruction to reduce the muon induced background in large volume liquid scintillator detectors. Master's thesis, University of Hamburg, 2017. URL `http://www.neutrino.uni-hamburg.de/sites/site_neutrino/content/e60876/e101065/e267767/infoboxContent288365/ba_felix_final.pdf`.

[121] D. Meyhöfer. Vertex reconstruction in large liquid scintillator detectors. Master's thesis, University of Hamburg, 2016. URL `http://www.neutrino.uni-hamburg.de/sites/site_neutrino/content/e60876/e208869/e279634/infoboxContent298515/masterarbeit.pdf`.

[122] J. Dittmer. Solar neutrino studies, background evaluation for the $0\nu\beta\beta$ search and topological track reconstruction with the SNO+ experiment. Master's thesis, Technische Universität Dresden, 2019.

[123] E. Gatti and F. De Martini. A new linear method of discrimination between elementary particles in scintillation counters. In IAEA, editor, *Proceedings of the Conference on Nuclear Electronics. V. II*, pages 265–276, 1962. URL `https://inis.iaea.org/search/search.aspx?orig_q=RN:43116654`.

[124] G. Bellini et al. First Evidence of pep Solar Neutrinos by Direct Detection in Borexino. *Phys. Rev. Lett.*, 108(051302), 2012. doi:10.1103/PhysRevLett.108.051302.

[125] M. Agostini et al. Simultaneous precision spectroscopy of pp, 7Be, and pep solar neutrinos with Borexino Phase-II. *Phys. Rev. D*, 100(082004), 2019. doi:10.1103/PhysRevD.100.082004.

[126] Y. Cheng et al. e+/e- discrimination in liquid scintillator and its usage to suppress 8He/9Li backgrounds. *Chin. Phys. C*, 41(1), 2017. doi:10.1088/1674-1137/41/1/016101.

[127] 2019. URL `http://www.tunl.duke.edu/nucldata`. TUNL Nuclear Data Evaluation Project.

[128] H. de Kerret et al. Yields and production rates of cosmogenic 9Li and 8He measured with the Double Chooz near and far detectors. *J. High Energ. Phys.*, 2018. doi:10.1007/JHEP11(2018)053.

[129] C. Galbiati et al. Cosmogenic 11C production and sensitivity of organic scintillator detectors to pep and CNO neutrinos. *Phys. Rev. C*, 71(055805), 2005. doi:10.1103/PhysRevC.71.055805.

[130] A. Li et al. Suppression of cosmic muon spallation backgrounds in liquid scintillator detectors using convolutional neural networks. *Nucl. Instrum. Methods Phys. Res., Sect. A*, 947(162604), 2019. doi:10.1016/j.nima.2019.162604.

[131] 2019. URL `www.nucleonica.com/Application/ReducedDecaySchemes/C11_TXT.htm`. Nucleonica.

[132] R. Möllenberg. *Monte Carlo Study of Solar 8B Neutrinos and the Diffuse Supernova Neutrino Background in LENA*. PhD thesis, Technische Universität München, 2013. URL `http://nbn-resolving.de/urn/resolver.pl?urn:nbn:de:bvb:91-diss-20131127-1175550-0-8`.

[133] I. Goodfellow et al. *Deep Learning*. MIT Press, 2016. URL `http://www.deeplearningbook.org`.

[134] P. Mehta et al. A high-bias, low-variance introduction to Machine Learning for physicists. *Phys. Rep.*, 810, 2019. doi:10.1016/j.physrep.2019.03.001.

[135] M. Abadi et al. Large-scale machine learning on heterogeneous systems, 2015. URL `https://www.tensorflow.org/`. Software available from tensorflow.org.

[136] F. Chollet et al. Keras, 2015. URL `https://keras.io`.

[137] Provided by Y. Xu, Forschungszentrum Jülich.

Danksagung

Auch wenn unter dem Titel dieser Dissertation mein Name steht, gibt es eine Reihe von Menschen, die das Gelingen des Projektes möglich gemacht haben. Das gilt zunächst für Prof. Dr. Caren Hagner, die meine Begeisterung für Neutrinos geweckt und mir die Möglichkeit gegeben hat, diese Arbeit zu verfassen. Ich möchte mich für das große Vetrauen bedanken, das sie mir dabei geschenkt hat. Dasselbe gilt für Dr. Björn Wonsak, der als sprudelnder Quell an Ideen und Motivation jedereit ein offenes Ohr für mich hatte. Ich hätte mir keinen besseren Betreuer wünschen können.

Aus dem engeren Kollegenkreis danke ich weiterhin Hans-Jürgen "Hajo" Ohmacht (selbstverständlich mit Handschlag) für den allmorgendlichen Gedankenaustausch, Daniel Bick und meinen Mit-Doktoranden David Meyhöfer, Stefan Bieschke und Malte Stender für die Hilfe programmier-, installier- und korrigiertechnischer Art, Sebastian Lorenz für vorbildliche Programmierarbeit und die Starthilfe in Form vieler wertvoller Kommentare sowie Felix Benckwitz für angeregte Gespräche, die ich in guter Erinnerung behalten werde. Bei euch und der gesamten Arbeitsgruppe Neutrinophysik, sowohl der alten als auch der neuen Garde, bedanke ich mich für die fantastische Arbeitsatmosphäre. Nicht zuletzt ihr seid der Grund dafür, dass es jeden Morgen Spaß macht, ins Büro zu kommen.

Es ist mir ein Anliegen auch die deutsche JUNO Forschergruppe hervorzuheben. Bei den zahlreichen Treffen habe ich viele nette Menschen kennenlernen dürfen, was zu der komfortablen Situation geführt hat, für fast jedes Problem geeignete Ansprechpartner zu haben. Gleiches gilt für die JUNO Kollaboration. I would like to thank Yu Xu for the good cooperation in the context of event discrimination and for the preparation of simulation data. I also thank Tao Lin for the great support concerning the simulation framework: he never failed on providing quick and accurate answers to my questions.

Ein großer Dank gilt meiner Familie und meinen Freunden, die mich in meiner Arbeit bestärkt haben auch ohne nachvollziehen zu können, warum die Neutrinomassenordnung geklärt werden muss. Auch die Gelegenheiten, bei denen sie mich vom Schreibtisch ferngehalten haben, waren wichtige Momente ausgleichender Zerstreuung. Besondere Erwähnung verdient Leonie, die mich unterstützt und mir den Rücken freigehalten hat.

Bei dir, Mathilda und Ole bedanke ich mich vor allem, denn ihr sei der Grund, weshalb ich mich jeden Tag freue wenn es Zeit wird, den Bildschirm auszuschalten, den Stift wegzulegen und nach Hause zu kommen.

Eidesstattliche Versicherung / Declaration on oath

Hiermit versichere ich an Eides statt, die vorliegende Dissertationsschrift selbst verfasst und keine anderen als die angegebenen Hilfsmittel und Quellen benutzt zu haben.
Die eingereichte schriftliche Fassung entspricht der auf dem elektronischen Speichermedium.
Die Dissertation wurde in der vorgelegten oder einer ähnlichen Form nicht schon einmal in einem früheren Promotionsverfahren angenommen oder als ungenügend beurteilt.

Hamburg, den 11.11.2019

Henning Rebber